University of Southampton

Faculty Engineering and Physical Science

Zepler Institute for Photonics and Nanoelectronics

Thermally insensitive fibre delay-line interferometer operating at room temperature

DOI [enter DOI]

[Volume X of Y]

by

Bo Shi

ORCID ID [bshi@mail.ustc.edu.cn]

Thesis for the degree of Doctor of Philosophy

May 2024

Abstract

Due to the unique properties of fibre interferometers, such as low cost, easy alignment, and light weight, they have become popular in scientific research. However, optical fibre is susceptible to environmental noise, including pressure perturbations, acoustic vibrations, and temperature variations. In some specialized applications, such as frequency references, optical fibre sensing, and metrology, a stable fibre interferometer is strongly required.

Various methods have been proposed to reduce fibre interferometers' sensitivities, especially the sensitivity to temperature. These methods generally have not achieved zero thermal sensitivity at room temperature and sometimes require cryogenic environment. The motivation behind this project is to build a thermally insensitive fibre interferometer that operates at room temperature without the need for a vacuum environment or an expensive thermal control system.

In this thesis, a compensated delay-line fibre interferometer structure is proposed to achieve zero thermal sensitivity. One arm is constructed with a long length of hollow-core fibre (HCF) with low thermal sensitivity to provide optical delay, while the other arm is made of a short standard single-mode fibre (SSMF) with high thermal sensitivity to compensate for the thermally induced phase accumulation in the HCF arm. Simulation results in COMSOL with different winding patterns show that the thermal stability of this design is 1000 times better than that of SMF-based interferometers.

A prototype of the compensated Mach-Zehnder fibre interferometer is fabricated and characterized. The results demonstrate that the coating of HCF significantly affects the thermal response. By employing thinly-coated HCF and single mode fibre (SMF), the first generation of the thermally insensitive fibre interferometer is fabricated and characterized. It crosses zero sensitivity at 28°C, and the zero-crossing temperature can be tuned by adjusting the length of SMF in the compensation arm. Furthermore, it exhibits 1000 times better thermal stability than SSMF within a ±1°C range. Unfortunately, the thinly-coated HCF was found to suffer from random breaks when coiled over extended period of time.

The second generation of the interferometer benefited from mechanically stable HCF with thicker coating, effect of which was offset by using larger silica glass jacket. The long-term frequency instability ($\Delta f/f$) of this thermally insensitive interferometer reaches 10^{-12} at averaging time of 1000 seconds. Additionally, by reducing the Fresnel reflections at the SSMF-HCF interfaces, the Mach-Zehnder interferometer was upgraded to a Michelson interferometer with Faraday rotator mirrors (FRM), which is polarization insensitive and provide double the delay length. This represented the third compensated interferometer generation.

Lastly, the application of laser stabilization to the thermally insensitive fibre interferometer was demonstrated, showing over an order-of-magnitude improvement in the long-term stability of the laser frequency when compared to a free-running laser. we believe this low-cost and high-performance thermally insensitive fibre interferometer will be of interest in various scientific research applications.

Keywords: Fibre interferometer, hollow core fibre, thermal sensitivity, laser stabilization

Abbreviations

AOM: acousto-optic modulator

AR coating: anti-reflective coating

ARF: antiresonant hollow core fibre

BS: beam splitter

CTE: coefficient of thermal expansion

CTF: conjoined-tube fibre

DFB EDFL: distributed feedback external diode fibre laser

DNANF: double nested antiresonant nodeless hollow core fibre

ECDL: external cavity diode laser

EOM: electro-optic modulator

FDL: fibre delay-line

FP cavity: Fabry-Perot cavity

FPI: Fabry-Perot interferometer

FRM: Faraday rotator mirror

FTIR: Fourier transform infrared spectroscopy

GRIN: gradient refractive index fibre

HCF: hollow core fibre

HOM: high order mode

Iso: optical isolator

LIGO: laser interferometer gravitational-wave observatory

LPF: low pass filter

MA: mode adapter

MFD: mode field diameter

MI: Michelson interferometer

MIOC: multifunctional integrated optical chip

MZI: Mach-Zehnder interferometer

NANF: nested antiresonant nodeless hollow core fibre

OFDR: optical frequency domain reflectometry

ORC: optoelectronic research centre

OTDR: optical time domain reflectometry

PBGF: photonic bandgap hollow core fibre

PBS: polarization beam splitter

PD: photodetector

PDE: partial differential equation

PDH: Pound-Drever-Hall

PER: polarization extinction ratio

PID: proportional-integral-derivative

PM: polarization maintenance

RF: radio frequency

SMF: single mode fibre

SSMF: standard single mode fibre

TEC: thermo-electric cooler

T-HCF: thinly-coated HCF

T-SSMF: thinly-coated standard SMF

ULE: ultra-low expansion

VCO: voltage-controlled oscillator

ϕ-OTDR: phase sensitive optical time domain reflectometry

Table of Contents

List of Accompanying Materials

Research Thesis: Declaration of Authorship

I declare that this thesis and the work presented in it are my own and has been generated by me as the result of my own original research.

I confirm that:

1. This work was done wholly or mainly while in candidature for a research degree at this University;
2. Where any part of this thesis has previously been submitted for a degree or any other qualification at this University or any other institution, this has been clearly stated;
3. Where we have consulted the published work of others, this is always clearly attributed;
4. Where we have quoted from the work of others, the source is always given. With the exception of such quotations, this thesis is entirely my own work;
5. I have acknowledged all main sources of help;
6. Where the thesis is based on work done by myself jointly with others, we have made clear exactly what was done by others and what we have contributed myself;
7. Parts of this work have been published as:

Shi, B., Zhang, C., Fokoua, E. R. N., Poletti, F., Richardson, D. J., & Slavík, R. (2023, May). Towards spliced SMF to hollow core fiber connection with low loss and low back-reflection. In *CLEO: Science and Innovations* (pp. STh1G-3). Optica Publishing Group.

Shi, B., Davidson, I. A., Mahdiraji, G. A., Rzegocki, J., Fokoua, E. R. N., Mousavi, M., ... & Slavík, R. (2023, May). Optimizing hollow core fibers for stable interferometry. In *2023 Joint Conference of the European Frequency and Time Forum and IEEE International Frequency Control Symposium (EFTF/IFCS)* (pp. 1-2). IEEE.

Shi, B., Marra, G., Feng, Z., Sakr, H., Hays, J. R., Fokoua, E. R. N., ... & Slavík, R. (2021, May). Temperature-insensitive delay-line fiber interferometer. In *2021 Conference on Lasers and Electro-Optics (CLEO)* (pp. 1-2). IEEE.

Shi, B., Marra, G., Feng, Z., Sakr, H., Hayes, J. R., Fokoua, E. R. N., ... & Slavík, R. (2022). Temperature insensitive delay-line fiber interferometer operating at room temperature. *Journal of Lightwave Technology*, *40*(16), 5716-5721.

Shi, B., Sakr, H., Hayes, J., Wei, X., Fokoua, E. N., Ding, M., ... & Slavík, R. (2021). Thinly coated hollow core fiber for improved thermal phase-stability performance. *Optics Letters*, *46*(20), 5177-5180.

Signature: ..... Date:.....

Acknowledgements

I would like to express my heartfelt gratitude to my supervisor, professor Radan Slavík, for his unwavering support, guidance, and mentorship throughout the duration of my project. His expertise and encouragement have been instrumental in shaping my research and personal growth. I extend my sincere appreciation to my dedicated team members who have worked tirelessly alongside me, Meng, Xuhao, Cong, Win, Irene, Lauren, Zitong, and so on. Your collaboration, expertise, and commitment have been invaluable, and I am truly grateful for the collective effort that has gone into this endeavour. A special thank you goes out to my friends in the UK for their friendship, encouragement, and the countless moments of respite during this journey, another Meng, Long, Yuanguo and so on. Your support has made this experience richer and more enjoyable. To my family, who has been my constant pillar of strength, I am deeply grateful for your unwavering support, understanding, and love. Your encouragement has been the driving force behind my accomplishments. Last but certainly not least, I want to express my gratitude to my girlfriend for her patience, understanding, and unwavering belief in me. Your support has been my source of inspiration, and I am truly blessed to have you by my side. Thank you, each one of you, for being an integral part of my journey. Your contributions have made a significant impact, and I am truly appreciative.

Chapter 1 Introduction

In this chapter, we briefly introduce the thesis topics following the motivation and description of novelty of my work. Finally, we give the structure of the thesis.

1.1 Fibre Interferometers

1.1.1 Interferometry and interferometers

In 1678, Huygens proposed the wave theory of light against Newton's particle theory of light, and in 1803, Thomas Young described his famous interference experiment known as the double-slit experiment to support this theory [1], as depicted in FIGURE 1.1. In this experiment, coherent light emanating from slit *A* is subsequently split by two slits, *B* and *C*, and the diffracted two beams then overlap and interfere with each other on the screen. The observed result is an alternating pattern of bright and dark fringes, referred to as an interference pattern, which proves that light behaves like a wave as it exhibits interference effects characteristic of wave phenomena. Later, various interferometers are proposed to test the speed of light [2], like the Michelson interferometer (MI) [3], Mach-Zehnder interferometer (MZI) [4], Fizeau-Foucault apparatus [5], the Sagnac interferometer [6], and others, which inspired the development of interferometry. Here we introduce some of them that are relevant to the subsequent content.

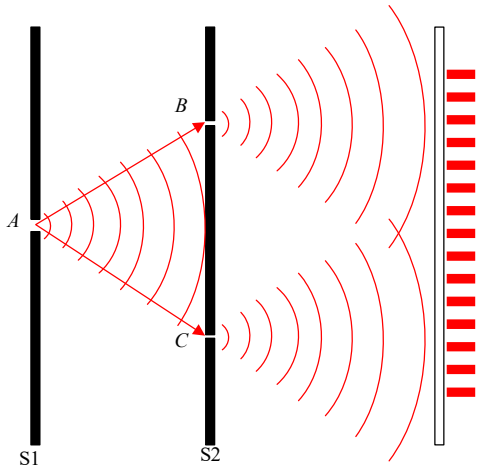

FIGURE 1.1. Schematic of Young's double-slit experiment.

Michelson and Morley proposed the important interferometric configuration, the Michelson interferometer, and conducted experiment to prove against the existence of aether that Einstein's theory of special relativity had discarded. The configuration of Michelson interferometer is shown

in FIGURE 1.2. The incident light beam is split into two paths, and the two beams are then reflected by the mirrors and overlapped together after passing through the beam splitter (BS). The resulting coherent pattern is detected by the photodetector, and any perturbation in arms will cause a change in pattern. Back to Michelson-Morley's experiment, one arm of the interferometer follows the direction of Earth's rotation, and the other one is perpendicular to it. If the aether existed, the dragging effect would cause a speed difference between the two beams and lead to a pattern shift. However, no interference shift was detected, which means there is no observable difference in the speed of light in the perpendicular directions.

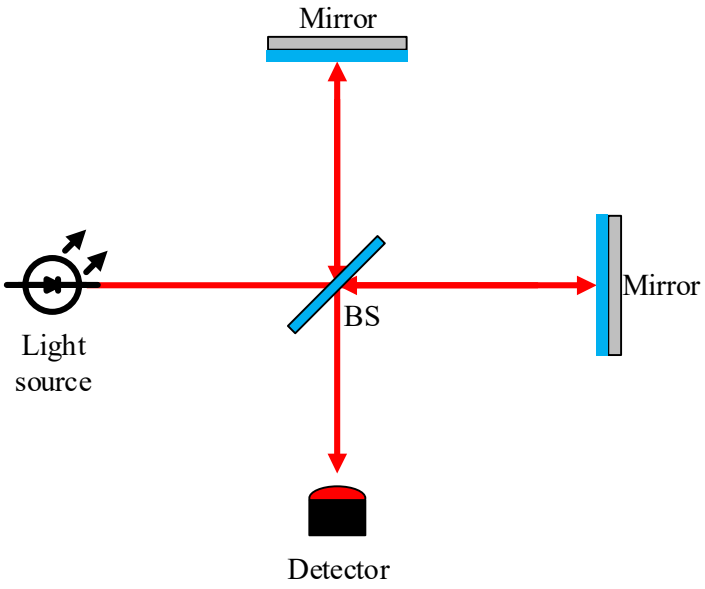

FIGURE 1.2. Configuration of Michelson interferometer

Sagnac interferometer was built by Georges Sagnac who set up the experiment to prove the existence of the aether. The structure is shown in FIGURE 1.3, a beam of light is split into two beams by the BS, and the two beams are made to propagate through the same paths but in opposite directions and out of loop at the enter point, the interference is detected by a photodetector. The relative phase difference is dependent on the angular velocity of the apparatus. If there is no rotation of the frame, no shifting interference patter could be observed.

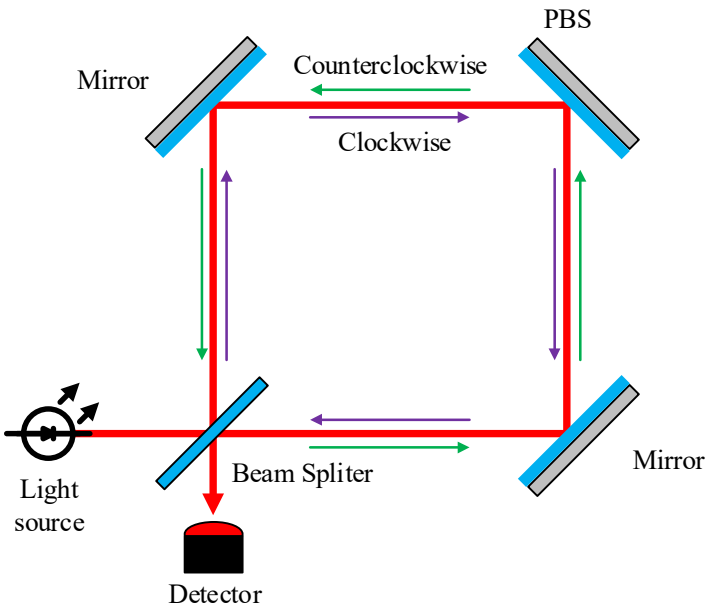

FIGURE 1.3. Configuration of Sagnac interferometer

FIGURE 1.4 shows the configuration of a Mach-Zehnder interferometer. A light beam is split into two beams, which propagate through two different optical paths. Subsequently, they are reflected by the mirrors into BS to overlap with each other; the transmitted interference signal is then detected by the photodetector. When there is a perturbation in either arm, such as air flow, air pressure variation, or length perturbation, et at., the relative phase between the two beams varies. This phase perturbation is then observed in the form of fringes shift or amplitude variations.

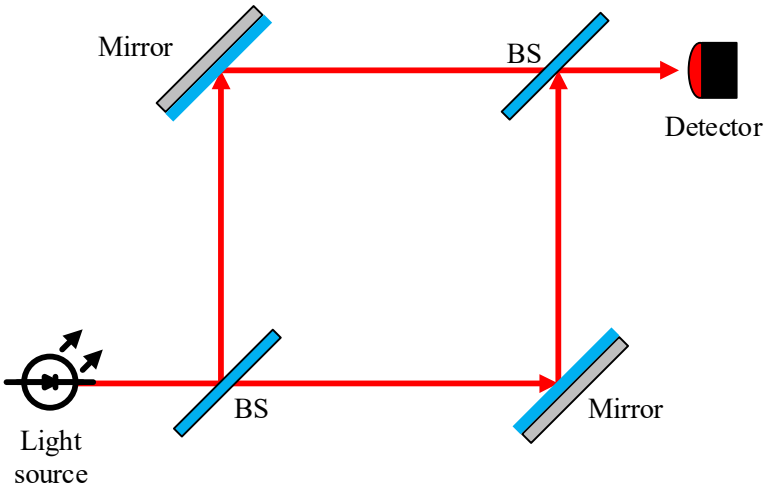

FIGURE 1.4. Configuration of Mach Zehnder interferometer

Fabry-Perot interferometer (FPI), also known as etalon is an optical cavity formed by two parallel reflective surfaces (i.e., mirrors) [7]. Unlike the interferometers introduced above, it detects the interference of multi-waves. As seen from FIGURE 1.5, the light incident into the cavity is reflected many times and passes through the cavity only when the phase difference of the overlapping waves out of the mirror is integer multiple of π (resonance condition), which is determined by the wavelength of incident light, length, and refractive index of cavity. The FPI was developed by Charles Fabry and Alfred Perot and is widely used in wavelength measurement.

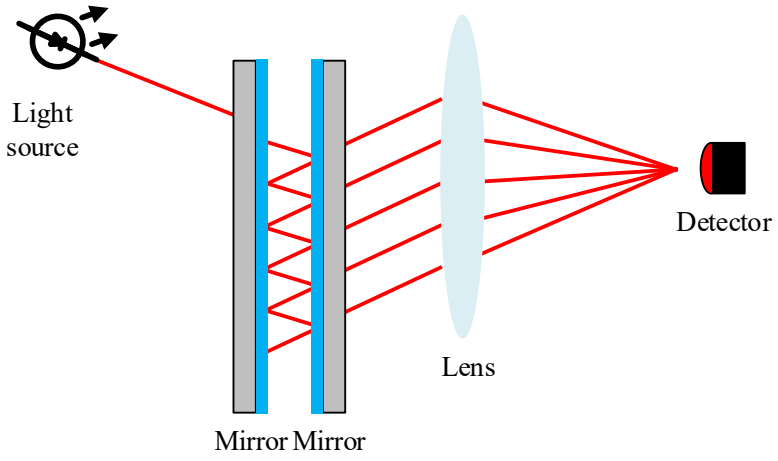

FIGURE 1.5. Configuration of Fabry-Perot interferometer

Interferometers are widely used in scientific research areas, such as metrology [8], sensing [9], optical filtering [10]. One of the most famous applications is laser interferometer gravitational-wave observatory (LIGO) [11], shown in FIGURE 1.6.

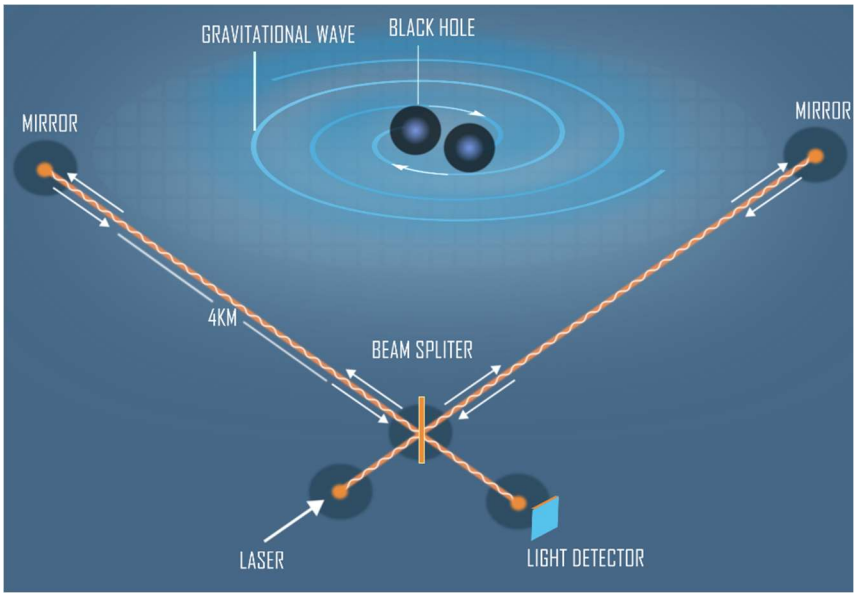

FIGURE 1.6. The schematic of LIGO from [12].

LIGO is a giant Michelson interferometer, of which two arms are 4 km long and perpendicular with each other. The ultra stable laser sends the light into the instrument and the beam is split along two arms. The light is bounced back by the reflection of mirrors. Normally, the light waves from two arms return and cancel each other at the output due to the identical configuration of two arms. When there is a gravitational-wave pass through the two arms, which will affect the length of two arms, and the uncancelled light waves will be received by the detector.

Beside the giant gravitational-wave detector, Michelson interferometer can also be employed in Fourier transform infrared spectroscopy (FTIR) [13]. Here the light source is polychromatic infrared light, by moving one of the mirrors, collecting the interference light after the absorption of material under test, and using the Fourier transform, the spectroscopy is obtained.

Another important application of interferometer is used for laser stabilization. Recently, the frequency instability of highest performance laser is reported to be 10^{-17} in 1 s, which is calculated by counting the beat frequency with another stabilized laser (same configurations). It is achieved by stabilizing a free running laser to an ultra-stable FPI based on Pound-Drever-Hall (PDH) method, shown in FIGURE 1.7 [14]. Here the FP cavity is used as a frequency discriminator, by comparing the frequency perturbation of the laser to the reflection spectrum of FP cavity to generate error signal which is sent to the servo to correct the laser frequency variation (Details will be discussed in later content).

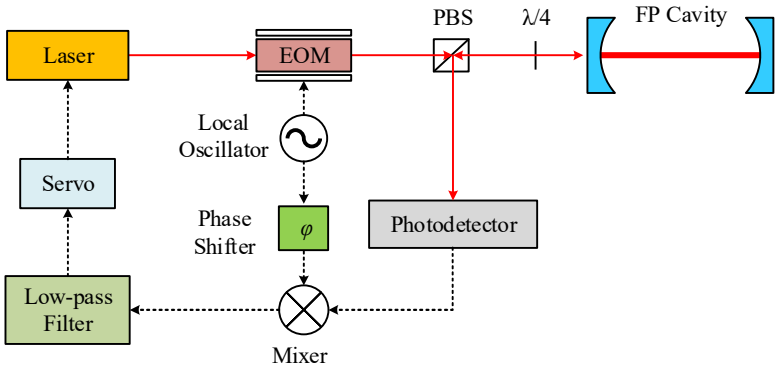

FIGURE 1.7. Schematics of PDH method adapted from [15].

The heavy weight, complex alignment, and difficulty in achieving long delays in a small volume limited the applications of space-aligned interferometers. However, the situation was changed with the appearance of optical fibres.

1.1.2 Fibre-based interferometers

Optical fibre has been developed for years, the structure and guiding principle of optical solid core fibre are shown in FIGURE 1.8. Typical fibre cable contains five parts: an outer jacket, a strength member, a coating, cladding and a core. The first two parts are mainly used for protecting fibre from strain damage, and coating is used to prevent the scratch of glass cladding and reduce the micro bending loss in the fibre. The cladding and core are responsible for propagating the light based on total inner reflection, with most light traveling through the inner core due to its higher refractive index.

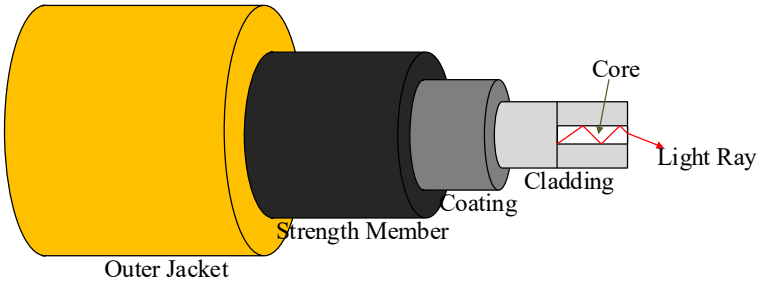

FIGURE 1.8. The structure of a typical fibre cable.

Optical fibre has many unique advantages compared to metal wire in propagation of light, such as: lower loss (0.15 dB/km at 1550 nm); light weight, alignment-free, small volume. With the advantages of optical fibre, fibre-based interferometers are constructed and well developed, here are some examples. For fibre-based MZI (see in FIGURE 1.9), the beam splitters are replaced by the optical couplers, and due to the light guided in the fibre can be bent, mirrors are not needed [16].

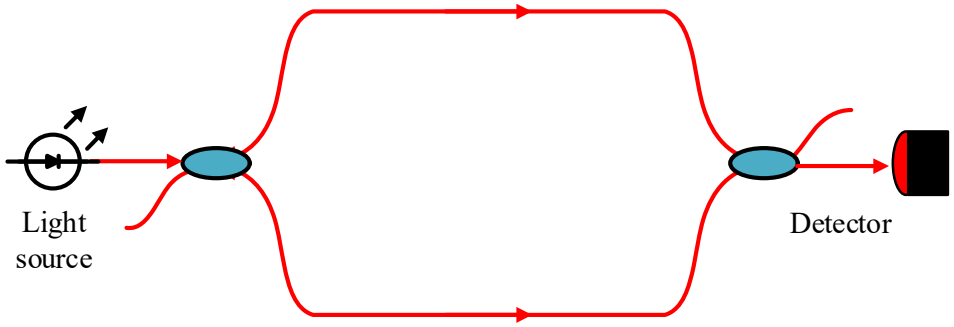

FIGURE 1.9. The configuration of fibre Mach-Zehnder interferometer.

Same as the fibre-based MZI, the beam splitter of MI is replaced by the coupler. As light is propagated in the fibre, which means it can be easily aligned. Moreover, the mirrors can be replaced by micro mirrors with fibre pigtails which can be connected or spliced to the fibre, allowing a robust connection [17]. The structure is shown in FIGURE 1.10.

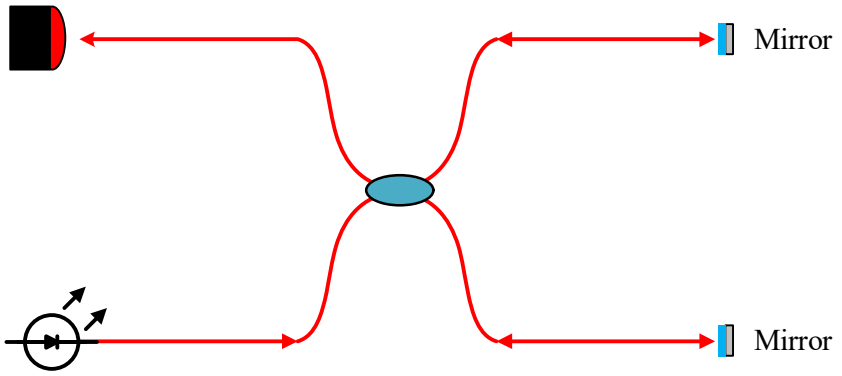

FIGURE 1.10. The configuration of fibre Michelson interferometer.

For fibre FPI (depict in FIGURE 1.11), besides the replacement of splitters by the fibre coupler, the reflected mirrors could be replaced by the fibre Bragg grating (FBG) which can reflect light at certain wavelength [18].

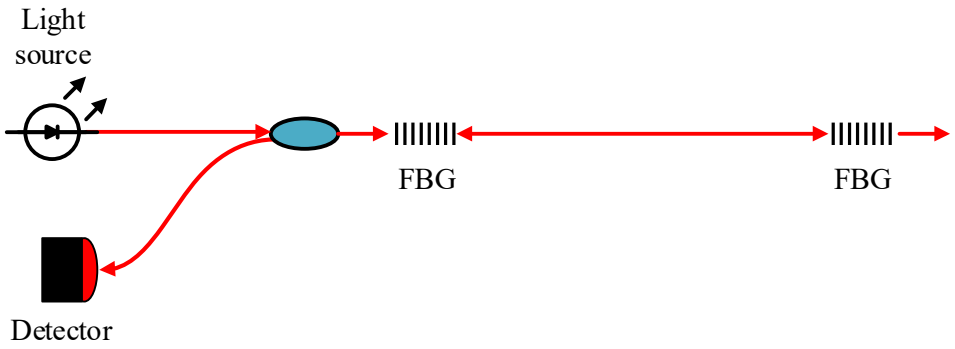

FIGURE 1.11. The configuration of fibre Fabry-Perot interferometer.

The fibre Sagnac interferometer achieves long delay by the fibre spools in a small space without any reflective mirrors, thanks to the bendability of fibre [19]. The configuration is shown in FIGURE 1.12. Light passes through the circulator before the beam is bifurcated by the multifunctional integrated optical chip (MIOC), capable of implementing various functional modulations such as phase modulation. Subsequently, the light travels through the fiber spool in two opposing directions—clockwise and counterclockwise. The resulting beams exit the spool and interfere within the MICO, with the resultant signal propagated to the detector through the circulator.

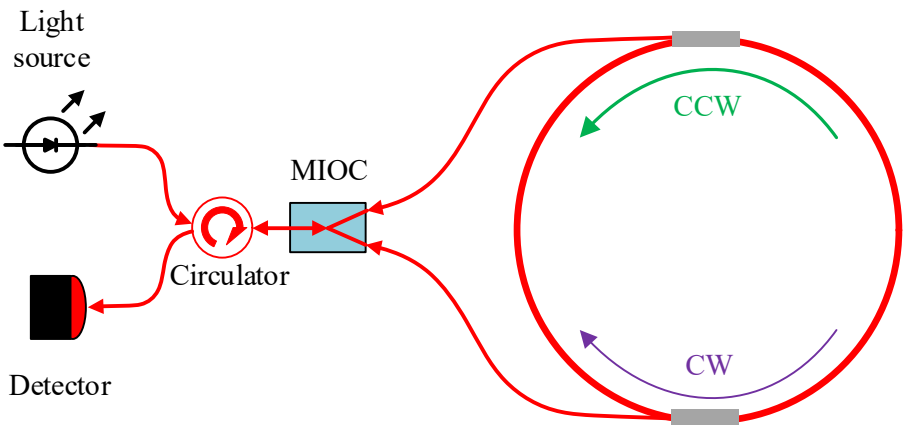

FIGURE 1.12. The configuration of fibre Sagnac interferometer (fibre gyroscope).

Compared to space-aligned interferometers and introduced earlier, fibre-based interferometers can be light weight and compact while providing long delay, thanks to the bendability of fibre. They can be easily connected or spliced together, allowing a robust connection and easy alignment. These additional advantages extend the applications of interferometry. Besides the typical applications of space-aligned interferometer, fibre interferometers can be employed in more complicated scenarios, such as fibre hydrophone [20], or phase sensitive optical time domain reflectometry (ϕ-OTDR) [21], enabling distributed and long-distance sensing. One of the important applications of fibre interferometer is as an alternative to FP cavity as frequency discriminator in ultra-stable laser stabilization[15].

1.1.3 Stable fibre interferometers in laser stabilization

Ultras-table lasers with high frequency stability and phase coherence has been strongly required in many research applications, such as optical atomic clocks [22], gravitational wave detection [23][24], low-noise microwave synthesis [25], and fundamental physics[26] .It is usually achieved by stabilizing the laser to a FP cavity [27], fibre interferometer [28] or some other stable frequency reference [29][30]. Latest reported laser stabilized to an ultra-stable cavity has achieved the frequency stability of 10^{-17} at 10 s [14], which employs a vacuum and cryogenic environment to supress the noise floor of cavity and coatings. For some specific applications, such as space ranging interferometry and coherent optical satellite links [31][32], of which laser system is requiring light weight, robust and easy-align structure, therefore, an optical fibre delay-line interferometer stabilized laser would be one of the best alternative.

Laser stabilization principle is shown in FIGURE 1.13. This scheme is a negative feedback control system. An error signal indicating the laser noise is obtained by comparing the laser signal

with the external reference. Then the loop filter corrects the laser frequency noise with negative feedback. Based on this principle, several methods have been proposed to stabilized laser with different optical frequency reference, e.g., transmission fringe locking which uses an automated feedback system to keep the laser frequency on one side of a resonance of the resonator, correcting the frequency perturbation based on the decrease or increase of the transmitted intensity [33], self-injection locking, enforcing operation of a laser on a certain optical frequency by injecting light with that frequency into the laser resonator [34], and Hänsch–Couillaud stabilization, detecting the frequency-dependent polarization change for error signals without any modulations [35].

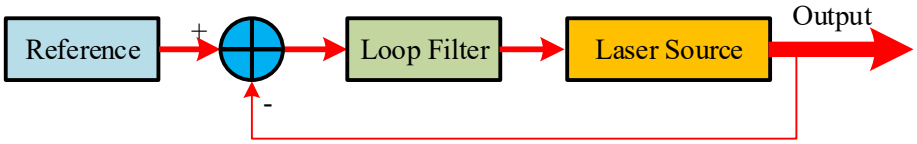

FIGURE 1.13: General scheme of a frequency stabilized laser.

Recently, the best performance ultra-stable laser is achieved based on PDH method, stabilizing the laser to a high finesse and ultra-stable cavity [14] [15]. Frequency stability of these cavity stabilized laser is dependent on the stability of cavity optical length, which is limited by thermal and vibration-induced cavity length fluctuation, and thermal-mechanical noise of the passive cavity components. Low coefficient of thermal expansion (CTE) material is employed to make the spacer and mirror substrate which can minimize the coupling of temperature variations to the optical path and frequency stability. Numata, et al. discussed the mechanical loss of these material and concluded that using fused silica or ultra-low expansion (ULE) for the mirrors and spacers can minimize the thermal noise [36]. Later Stoehr et al. reported an external cavity diode laser (ECDL) stabilized to an ULE cavity with 8 cm diameter and 10 cm length, which was placed in a vacuum chamber operating at 24 ℃ (zero CET at ~11 ℃), achieved 1.5 Hz linewidth at 657 nm and $<2\times10^{-15}$ fractional stability in 1 s [37]. Besides the reduced thermal length perturbation, the cavity was also reported to be vibration-insensitive, which was horizontally mounted and supported by four points, then optimized by the finite-element analysis, showing two orders less sensitivity than usual supported from below [38]. Later a shorter length (7 cm) ULE cavity, which was mounted vertically to exploit the intuitive symmetry in the vertical direction, was employed to stabilize the diode laser, achieving 2 Hz transmission linewidth and 10^{-15} fractional frequency stability at time scale of 0.5 s to 300 s [39]. To stabilize the ULE cavity at zero CTE point, eliminating the thermal expansion, Peltier elements were placed in vacuum allowing operation at an optimal temperature [40]. This vibration and thermally compensated system suppressed the laser linewidth down to subHertz. [36]

reported fused silica could reduce the contribution of thermal noise floor, and cavity with ULE-based spacer and fused silica mirrors was then reported to achieved frequency instability as 5.6×10^{-16} at 1 s [41].

Cavity made of crystalline material, such as silicon [27] or sapphire [42] , have a reduced thermal noise floor at least an order of magnitude than usual glass. Laser stabilized to a silicon cavity operating at 124 K (zero CTE temperature of silicon) showed 1×10^{-16} at short time scale and linewidth <40 mHz at 1.5 μm [27]. The stability was limited by thermal noise of optical coating, reducing the temperature to 4K could further improve the frequency stability [43], and latest reported stability was 6.5×10^{-17} from 0.8 to 80 s.

Besides these high-performance FP cavities stabilized laser which employed giant setups to provide the strictly required cryogenic temperature, micro-FP cavity used for chip-based laser has been fabricated [44]. It stabilized a laser with 1-s linewidth of 1 Hz and fractional frequency instability below 10^{-14} to 1 s. Note here the vacuum is employed to further suppress the thermally-induced drifts.

In addition, the complex alignment of free-space optical components and spatial mode matching, the requirement of vacuum environment, cryogenic temperature or highly stable temperature control system make this cavity stabilized laser expensive, bulky (maybe not for the chip-based FP cavity), and fragile. An alternatively method is stabilizing the laser to a fibre delay-line interferometer, which is supposed to be low-cost, light weight, compact and easy-to-align, besides, this method allows the high linearity frequency sweep, fast and wide range frequency tunning. The first fibre stabilized laser was reported by Chen [45], he used a 25-m single mode fibre (SMF) based MZI to stabilize a He-Ne laser, achieving 5 kHz linewidth and frequency stability less than 10^{-11} with a time of 1 s. Here the fibre spool is enclosed into a vacuum tank to reduce the thermal drift noise and hang to minimize the vibration influence. Later this technique is studied by many groups [46][47][48]. Cranch et. al presented a distributed feedback external diode fibre laser (DFB EDFL) stabilized to a longer delay-length (100 m) MZI using homodyne detection method to reduce the frequency noise as low as 1.5 Hz/√Hz at 1 kHz [46]. Cliche applied the same method to stabilize a diode laser achieves 10 Hz/√Hz at 10 kHz [48]. Crozatier reported a Michelson fibre interferometer extending the control bandwidth, which has a 10 km delay length [49]. Takahashi placed the Michelson interferometer (110 m arm imbalance) in a vacuum environment and stabilized the DFB EDFL to reach 2 Hz/√Hz at 80 Hz [50].

A novel work done by Kéfélian et al. presented a fibre Bragg grating laser stabilized to a fibre Michelson interferometer with 1 km delay [28], shown in FIGURE 1.14. The laser light passed through the acoustic optical modulator (AOM) driven by a voltage-controlled oscillator (VCO),

which applied ~40 MHz modulation frequency for PDH stabilization. Then it was split by the 1/99 coupler, 99% of the power was sent to the output, and 1% was sent into the Michelson interferometer. The interferometer was simply enclosed in a muti-layer thermal isolation box and placed on a passive anti-vibration platform. Ends of the arms are spliced with a Faraday rotator mirror to avoid the polarization degradation, of which the principle will be discuss in later content. In the delay-line arm, there is another AOM driven by a 70 MHz synthesizer for heterodyne detection to reduce the low frequency noise of the system. The detected signal from the interferometer will be mixed with the doubled frequency signal from the synthesizer, by the PI feedback loop, the laser was stabilized to the interferometer, of which the linewidth was reported to achieve 8 Hz in 1 s. Impressively, the frequency noise measured was believed to be at least as low as that stabilized to a ULE-cavity with comparable delay time between 40-40k Hz, and it also indicated that frequency noise below 40 Hz was mainly caused by the thermal noise fibres.

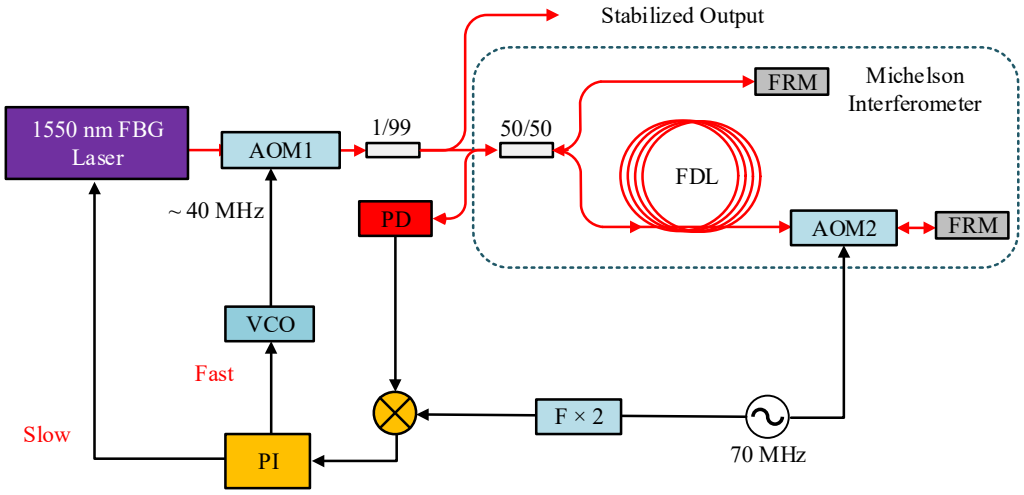

FIGURE 1.14: The principle of laser stabilized to a fibre Michelson interferometer (adapted from [28]). AOM: Acousto-optic modulator; FDL: fibre delay-line; FRM: Faraday rotator mirror; PD: photodetector; VCO: voltage-controlled oscillator.

To solve the excess frequency nose induced by mechanical vibration of fibre stabilized laser, vibration-insensitive fibre spool was studied in [51][52][53]. With a double-winding spool and optimized geometry parameter, the acceleration sensitivity of interferometer was reduced to 8×10^{-11} g^{-1} and $3\times10\text{-}^{11}$ g^{-1} in axial and radial directions. Employing this vibration-insensitive fibre spool design, laser stabilized to a 5-km SMF-based MI was reported to achieve long-term stability as 1.1×10^{-14} at 1000 s [54]. Here the fibre thermal noise was supressed by employing vacuum environment and precise thermal control where the temperature perturbation was under 10^{-8} K. The configuration of the system is shown in FIGURE 1.15 of which the stabilization method is the same as above.

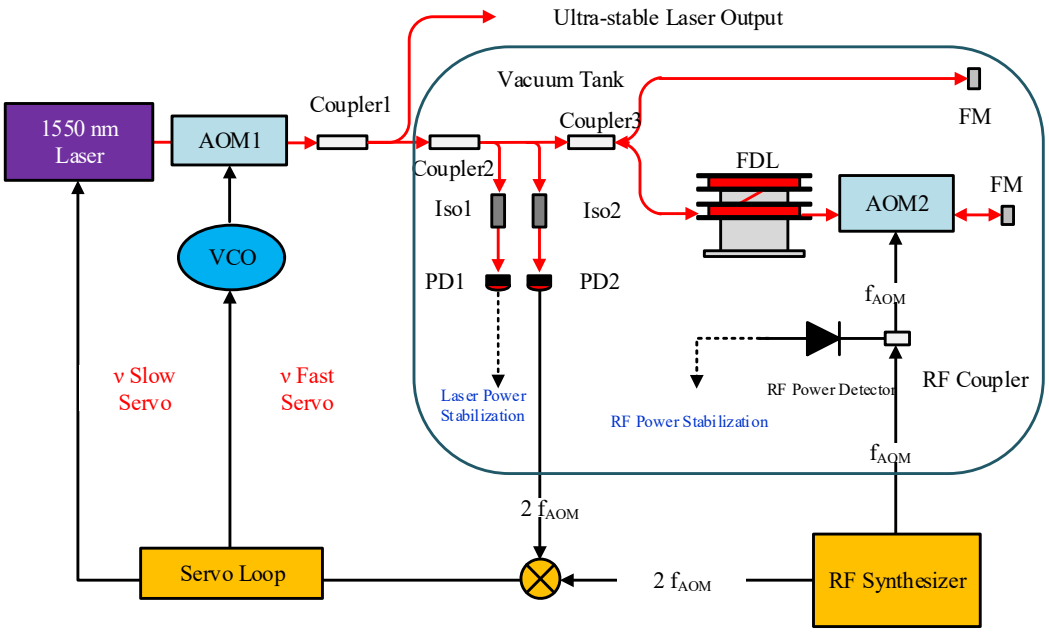

FIGURE 1.15: Schematic of latest fibre stabilized ultra-stable laser adopted from [54]. Iso, optical isolator; RF, radio frequency. Note here the fibre spool is wound in vibration-insensitive spool and housed in a five-layer vacuum tank to achieve the best performance.

A simple method to reduce the thermal influence on the fibre stabilized laser was proposed by Kong [55], utilizing two fibre interferometers within different thermal phase sensitivities, one was employed as frequency reference for laser noise correction, the other was used as thermometer to cancel the temperature variation. This reduced the Allan deviation of fraction frequency noise at 1000 s from 5.6×10^{-8} to 6.9×10^{-10} with a common active thermal control system.

To further improve the frequency of lasers limited by the thermal noise of fibre interferometer, fibre interferometer was cooled in cryogenic temperature, which is shown in FIGURE 1.16, showing first order temperature insensitive point at 3.55 K [56]. There are some differences between the interferometer stabilization method introduce above. The frequency reference here is a fibre ring resonator, and frequency modulation was achieved by the electro-optic modulator (EOM). Results showed the stabilized laser presents the similar low linear drift 5×10^{-11} h^{-1} as that stabilized to the ULE-cavities, furthermore, a 10^{-10} long-term instability of the stabilized laser frequency was achieved.

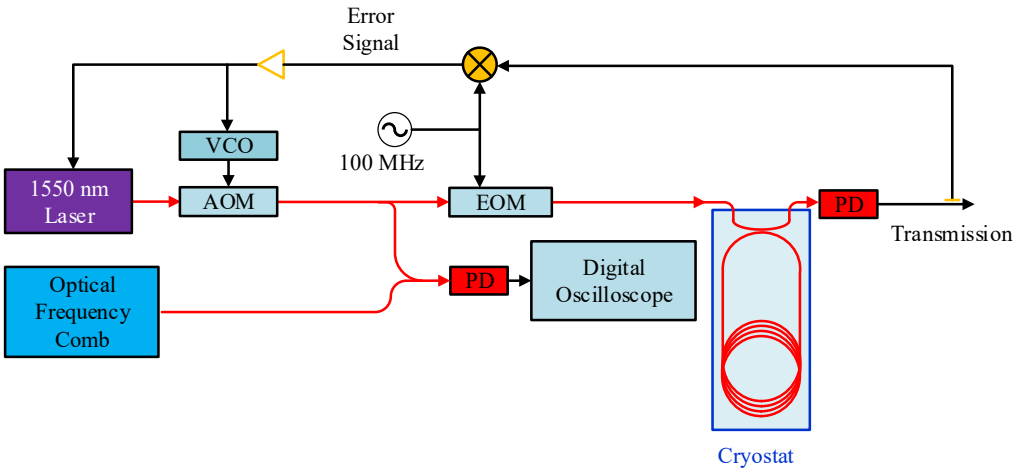

FIGURE 1.16: Experimental setup. A cryogenic fibre ring resonator serves as a frequency reference for stabilizing a laser at 1535 nm adapted from [56].

1.2 State of the art

In this thesis, we am focusing on the reduction of thermal sensitivity of fibre interferometers. The thermal phase noise of fibre is the results of two effects, the thermo-optic effect of the fibre core which changes the refractive index, and the length elongation due to the thermal expansion. There are already some research works on the reduction of thermal sensitivity of optical fibre as well as fibre-based interferometers.

Employing materials with low TEC for the fibre coating could reduce the thermal expansion of fibres [57], Bondza et al. tested single-acrylate and dual-acrylate fibre, copper-coated and aluminium-coated fibre, results show a potential of one order of magnitude improvement of thermal sensitivity with these metal-coated fibre [58]. Dragic showed the P_2O_5 doped fibre core has negative opto-thermal effect to compensate the elongation of fibre [59]. Feng et al. measured the lower thermal sensitivity of P_2O_5 doped fibre. Compared to standard single mode fibre (SMF), it has 27% lower thermal sensitivity, and it is believed to be even lower with higher levels of doping [60]. Zhu et.al proposed a method to reduce the fibre sensitivity by cooling it in cryogenic environment, based on his results, the thermal sensitivity of standard fibre is expected to reach zero near -250 ℃ [56][61].

Hollow core fibre (HCF) which guides the light though its centre air core has lower thermal sensitivity due to the low opto-thermal effect of air which is dominated by the elongation of silica glass and coating, which was firstly studied by Dangui. et al. [62]. They calculated and experimentally proved the thermal sensitivity of photonic bandgap hollow core fibre (PBGF) to be about 3-6 times better than SMF, and by special designing the coatings and jackets, it can be reduced to 11 times lower than SMF. Slavík et al. reported lower thermal sensitivity of PBGF (18 times better thermal stability) which is due to the different coating and jacket parameters [63]. To further reduce

the sensitivity, uncoated HCF (HCF-PBGF) was placed in cryogenic temperature -71 ℃, where the TEC of silica cross zero [64]. Same method applied to thinly-coated nested antiresonant nodeless hollow-core fibre (NANF) was reported to have lower zero-sensitivity temperature (-134℃), this was due to the coating's effect [65].

Some other methods have also been reported to further reduce thermal sensitivity of HCF at room temperature [66][67][68]. For example, HCF with open end was reported to achieved zero thermal phase sensitivity [66], the principle is shown in FIGURE 1.17. When the surrounding temperature increases, besides the thermal expansion induced length elongation, the air pressure inside will increase as well. If the end of HCF is not sealed, the air molecules will come out and decrease the density inside the air core, which reduce the refractive index of the HCF. This reduced refractive index compensates the phase increase due to the length change, achieving lower thermal sensitivity, which was even reported to cross zero at 110 ℃.

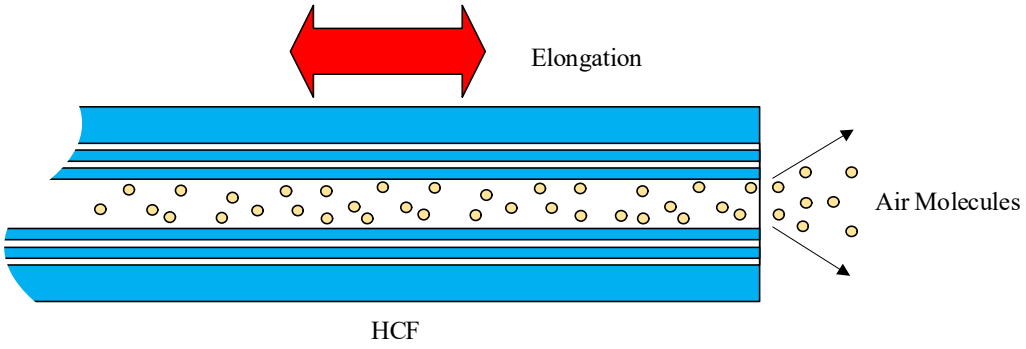

FIGURE 1.17. Schematic of open end HCF achieving low thermal phase sensitivity at room temperature.

Another effective way to reduce the thermal phase sensitivity of HCF is winding the fibre spool on a low TEC supporter reported in [67]. The fibre was spooled on the Zerodur with pre-set tension at low temperature, which means the fibre was stretched, when the temperature increased, the elongation of the fibre was compensated by the tension release, leading to a thermally insensitive elongation fibre spool. This method achieved 3 times lower thermal sensitivity and provided a potential way to achieve zero thermal sensitivity at room temperature.

Wingding HCF spool to achieve zero thermal sensitivity at room temperature without any supporter was also reported [68]. The mechanical parameter difference between silica and coating allowing the winding spool to generate a gradient tension along the fibre turns, and inside turns would be thermally insensitive. Optimizing the parameters of wingding turns and diameters, the spooled HCF achieved ~90 times better thermal stability than the unspooled HCF.

In this thesis, we proposed a method to achieve zero thermal sensitivity of a delay-line fibre interferometer at room temperature and constructing the interferometer with two fibres with different thermal sensitivities and lengths. This method needs no cryogenic temperature and any complex spool windings, which will benefit various applications where thermally stable interferometers are strongly required.

1.3 Aims and novelty

The main goal of the present research is to build a thermally insensitive fibre delay-line interferometer operating at room temperature, without cryogenic and vacuum environment. To achieve this goal, my contributions include:

- Proposed an all-fibre delay-line interferometer design based on the thermal phase compensation between two arms made from two different fibres, SMF and HCF, and simulated the thermal performance under temperature variations as described in Chapter 4
- Fabricated the prototype of thermally insensitive fibre delay-line interferometer, and iterated it through three generations with updated structure and fibres, developed phase extraction method to evaluate the thermal sensitivity of interferometers, as described in Chapter 4, 5, 6.
- Demonstrated the application of laser stabilization of this thermally insensitive fibre delay-line interferometer, described in Chapter 7.

1.4 Structure of the thesis

To clearly separate the work that we did from the state-of-the-art, all the chapters that discuss background and related literatures are at the beginning of the thesis, before presenting my works and results. The background knowledges of laser stabilization and hollow core fibres are presented in Chapter 2 and Chapter 3, respectively. The principle, simulation as well as the prototype of thermally insensitive fibre interferometer are shown in Chapter 4, Chapter 5-6 introduce the iterations of the thermally insensitive compensated fibre delay-line interferometer and the characterization, specifically, Chapter 7 demonstrates the application of laser stabilization.

Chapter 2 Background: Laser stabilization to fibre interferometers Background knowledge about laser stabilization to fibre interferometer is introduced in this chapter. The principle of PDH method stabilizing laser to a FP cavity is introduced first. Laser stabilized to the fibre interferometer is discussed then, including the principle, transfer function, and noise source analysis.

Chapter 3 Background: Antiresonant hollow core fibres A brief introduction of HCF is present in this chapter. The development of HCF and the guidance principle is introduced first. Then connection methods of integrating HCF to SMF system is reviewed. At the end, some important

characters of HCF are discussed, such as backscattering, thermal phase sensitivity and pressure sensitivity.

Chapter 4 Principle and prototype of thermally insensitive fibre delay-line interferometer The principle of thermally insensitive fibre interferometer is introduced in this chapter. The thermal sensitivity of fibre delay-line interferometer is introduced first. Then the compensated method to achieve a thermally insensitive interferometer is proposed. The feasibility of this compensation method is proved by finite element simulation and the prototype of compensated fibre Mach-Zehnder interferometer is fabricated and characterized in this chapter.

Chapter 5 First generation of thermally insensitive fibre delay-line interferometer The fabrication and characterization of the first generation of thermally insensitive fibre delay-line interferometer is fabricated and characterized in this chapter. The phase extraction method based on a 3×3 couple developed and the thermal response between thinly-coated HCF the prototype-used HCF are compared. Then the first generation of thermally insensitive fibre interferometer with the thinly-coated HCF is fabricated and later characterized with the updated measuring setup. Additionally, the improved measuring system with polarization and pressure perturbation reduction is introduced.

Chapter 6 Iteration and characterization of the thermally insensitive fibre delay-line interferometer The second and third generation of thermally insensitive interferometer with new HCF and longer delay-length is introduce in this chapter. The latest designed thinly-coated HCF is characterized first. With this HCF, the second generation thermally insensitive fibre delay-line interferometer is fabricated and its long-term stability is measured. Then the Michelson interferometer is built to reduce the polarization degradation and double the delay length as the third generation.

Chapter 7 Demonstration of laser stabilization to thermally insensitive fibre interferometers Application of **s**tabilization is demonstrated in this chapter. The configuration of the laser stabilization system is introduced first, then the results of long-term stability of laser stabilization to the second and third generation of the thermally insensitive fibre delay-line interferometer are presented.

Chapter 8. Conclusions and future work The conclusions are drawn, and future work is prospected in this chapter.

Chapter 2 Background: Laser stabilization to fibre interferometers

In this chapter, we first introduce the PDH method based on a FP cavity. Subsequently, we focus on the laser stabilization to fibre interferometer, including the principle, transfer function of fibre interferometer, and the noise source analysis.

2.1 Principle of PDH method

The PDH laser frequency stabilization technique relies on optical heterodyne detection, achieved through the generation of optical sidebands by RF phase modulation. This approach allows for the precise frequency stabilization to a fraction of the resonator bandwidth, all while maintaining a considerably wide locking range. Most notably, it offers a robust frequency stabilization. FIGURE 2.1 illustrates the fundamental principle of the PDH method.

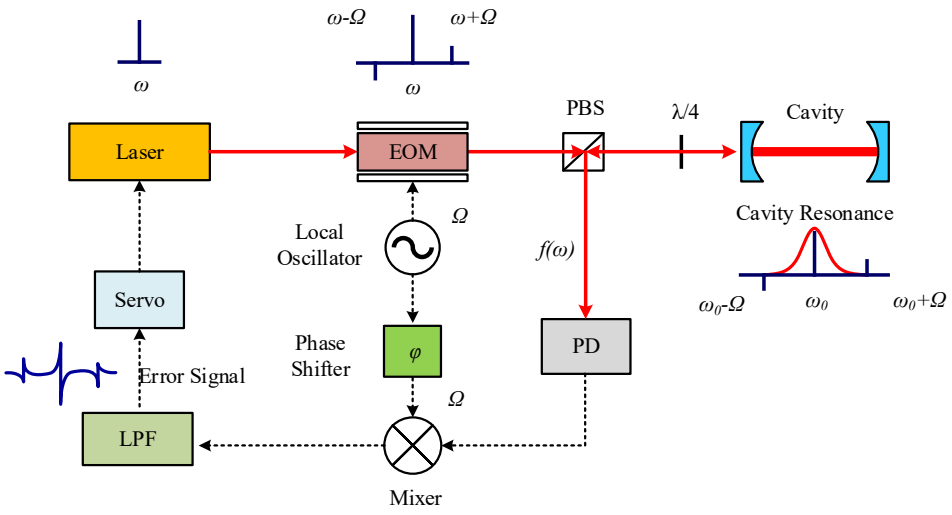

FIGURE 2.1: Working principle of PDH method adapted from [15] .

Light emitted from a laser with frequency of ω is modulated by the electro-optic modulator with two sidebands, ω + Ω and ω - Ω, passed through the polarization beam splitter (PBS) and quarter wave plate, the linear polarization is turned to circle polarization, and the light is sent to the cavity. The reflected light then passes through the quarter wave plate which turns the polarization of the reflected beam perpendicular to the incident, thus reflected by the PBS and detected by the photodetector, of which the electrical signal is then mixed with the modulation signal to generate the error signal. Note here the phase shifter is used to introduce a phase difference to achieve maximum

beat signal, which will be sent to the servo to correct the frequency error of the laser. To better understand this method, mathematic derivation is needed [15].

For a monochromatic laser light, its field can be written as:

$$E = E_0 e^{i\omega t}. \tag{2. 1}$$

Due to the requirement of heterodyne detection, the light is then modulated by an optical modulator:

$$E = E_0 e^{i[\omega t + \beta sin(\Omega t)]}. \tag{2. 2}$$

Here E_0 is the electrical field, ω is the frequency, β and Ω are modulation depth and frequency. When $\beta < 1$, the phase modulated filed can be expressed by Bessel series approximation as:

$$E_i \approx E_0[J_0(\beta)e^{i\omega t} + J_1(\beta)e^{i(\omega t+\Omega t)} - J_1(\beta)e^{i(\omega t-\Omega t)} \tag{2. 3}$$

J_i represents the i_{th} Bessel series. $J_{i>1}$ are relatively small compared to J_1 thus can be neglected.

The reflection of FP cavity can be written as [7]:

$$F(\omega) = \frac{E_r}{E_i} = \frac{r_1 - r_2 e^{i\phi}}{1 - r_1 r_2 e^{i\phi}} \tag{2. 4}$$

Here the E_i is the incident light field to the FP cavity, E_r is the reflected field. r_1 and r_2 are the reflectivity of the mirrors and ϕ is the phase difference acquired in one cavity loop.

Then the field of light reflected from the cavity is:

$$\begin{aligned} E_r = E_0[&F(\omega)J_0(\beta)e^{i\omega t} + F(\omega+\Omega)J_1(\beta)e^{i(\omega t+\Omega t)} \\ &- F(\omega+\Omega)J_1(\beta)e^{i(\omega t-\Omega t)}]. \end{aligned} \tag{2. 5}$$

The power detected by the photodetector is:

$$P_r = E_r E_r^*. \tag{2. 6}$$

$$= P_c|F(\omega)|^2 + P_s|F(\omega+\Omega)|^2 + |F(\omega-\Omega)|^2 \quad (2.\ 7)$$

$$+2\sqrt{P_cP_s}\{Re[F(\omega)F(\omega+\Omega)^* - F(\omega)*F(\omega-\Omega)]cos(\Omega t) + Im[F(\omega)F(\omega+\Omega)^* - F(\omega)*F(\omega-\Omega)]sin(\Omega t)\} \quad (2.\ 8)$$

$$+(2\Omega \text{ terms}). \quad (2.\ 9)$$

Here P_c and P_s are the power of carrier and sidebands. (2. 7) is the current part, (2. 8) is the interference signal between the carrier and sideband, and (2. 9) is the interference between two sidebands. Due to the phase shifter, the local oscillator will be shifted to sinusoidal function wave, thus the mixed signal can be maximized and then filtered by the low pass filter (LPF) to generate the error signal, which is sent to the servo to correct the laser frequency errors.

2.2 Fibre stabilized laser

In this section we will discuss the laser stabilized to fibre interferometer, to be more precisely, the delay-line fibre interferometer, such as fibre MZI and MI.

2.2.1 Principle

A fibre interferometer can be regarded as a frequency-to-phase converter when employed for laser stabilization, the principle is shown in FIGURE 2.2.

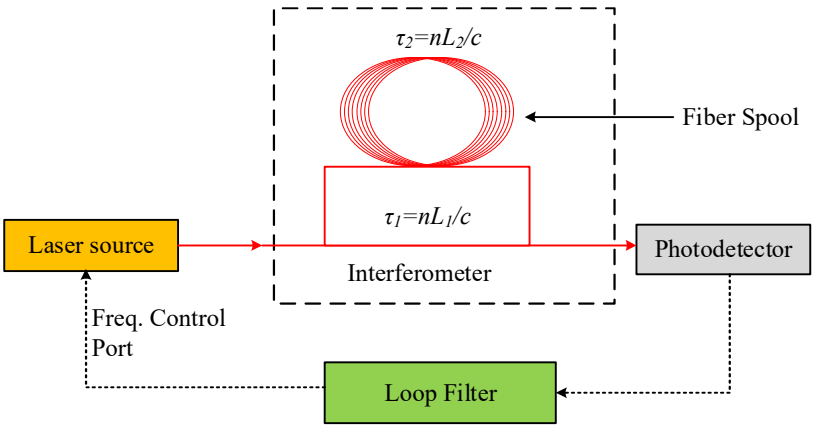

FIGURE 2.2: Principle of laser stabilization with a fibre-interferometer from [75] .

As shown in FIGURE 2.2, the laser signal is fed into the interferometer which has two arms of different length (L_1, L_2). The electric fields in the arms of the fibre interferometer are:

$$E_1 = E_0 sin[\omega t + \Gamma sin(\Omega t)], \tag{2. 10}$$

$$E_2 = E_0 \sin[(\omega'(t+\tau)], \tag{2. 11}$$

where ω and ω' denote the angular frequency of the beam in each arm of the interferometer and Γ and Ω denote the modulations on amplitude and frequency from an EOM driven by a synthesizer, here the delay time is:

$$\tau = n(L_1 - L_2)/c, \tag{2. 12}$$

n is the refractive index of fibre and $c$is the speed of light in vacuum. Provided the polarization of two arms are kept the same, using Bessel series approximation, the interferometric signal can be written as follows [45]:

$$\begin{aligned} I^2 = |E|^2 = {E_0}^2\{2 + \Gamma/2 - \Gamma/2\cos(2\Omega t) + 2\cos[(\omega-\omega')t - \omega'\tau] \\ + \Gamma cos[(\omega-\omega')t + \Omega t - \omega'\tau] - \Gamma cos[(\omega-\omega')t - \Omega t \\ - \omega'\tau]\} \end{aligned} \tag{2. 13}$$

The last two terms of Eq. (2. 13) times can be yield as:

$${E_0}^2 \Gamma\{cos[(\omega-\omega')t - \omega'\tau] sin(\Omega t)\}, \tag{2. 14}$$

The signal will be demodulated in the lock-in amplifier with reference signal as $sin(\Omega t)$ [69], here we just show the last two terms:

$$\begin{aligned} &{E_0}^2 \Gamma\{cos[(\omega-\omega')t - \omega'\tau] \times sin(\Omega t)\} \times sin(\Omega t) \\ &= {E_0}^2 \Gamma\{cos[(\omega-\omega')t - \omega'\tau]\} + \Gamma sin(2\Omega t) \end{aligned} \tag{2. 15}$$

After filtering the current and high frequency components $(\omega, \omega' \; and \; 2\Omega \; terms)$, the output becomes:

$$P = -{E_0}^2 \Gamma \sin[(\omega-\omega')t - 2\pi n \tfrac{L_1 - L_2}{\lambda'}], \tag{2. 16}$$

λ' is the optical wavelength at the end of delay arm (longer one).

When the phase is locked,

$$\sin[(\omega-\omega')t-2\pi n\frac{L_1-L_2}{\lambda'}]=0. \quad (2.17)$$

The solution is:

$$(\omega-\omega')t-2\pi n\frac{L_1-L_2}{\lambda'}=n\pi. \quad (2.18)$$

Where n is an integer. If $L_1-L_2$is assumed to be constant, while *t* is variable, Eq. (2. 18) can be further separated by:

$$\omega-\omega'=0; \quad (2.19)$$

$$2\pi n\frac{L_1-L_2}{\lambda'}=m\pi, m=0,1,2\ldots. \quad (2.20)$$

It shows that L_1-L_2 can be used to define λ'. With a negative feedback control, we can suppress the error signal to zero, and thus reduce the laser frequency fluctuation. Besides, it indicates that longer delay length gives a larger error signal as the phase change of the electrical fields is proportional to L_1-L_2.

2.2.2 Transfer function

Delay-line fibre interferometer can be regard as a frequency discriminator which transfer the frequency change to phase perturbation [47], The transfer function is:

$$T(f)=\frac{1-e^{-i2\pi f\tau}}{if}(Hz^{-1}). \quad (2.21)$$

Here f is the Fourier transfer frequency, and τ is the delay time.

At low frequency (f << $1/\tau$), $T(f)\propto\tau$, the phase change is approximately proportional to the delay time, in other word, the delay length of the interferometer. It means longer fibre leads to a higher response sensitivity to the frequency perturbation. However, there is a trade-off between sensitivity and modulation frequency bandwidth at high frequency. we plot the transfer function of two different length of fibres, both magnitude and phase in FIGURE 2.3 and FIGURE 2.4. As both are normalized, longer delay length can have null response at lower frequency.

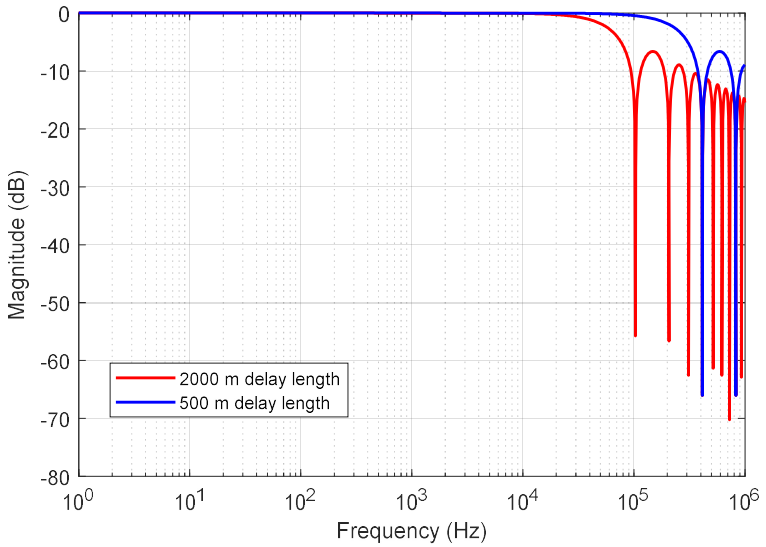

FIGURE 2.3: Interferometer amplitude response to laser frequency noise of delay length as 500 m and 2000 m

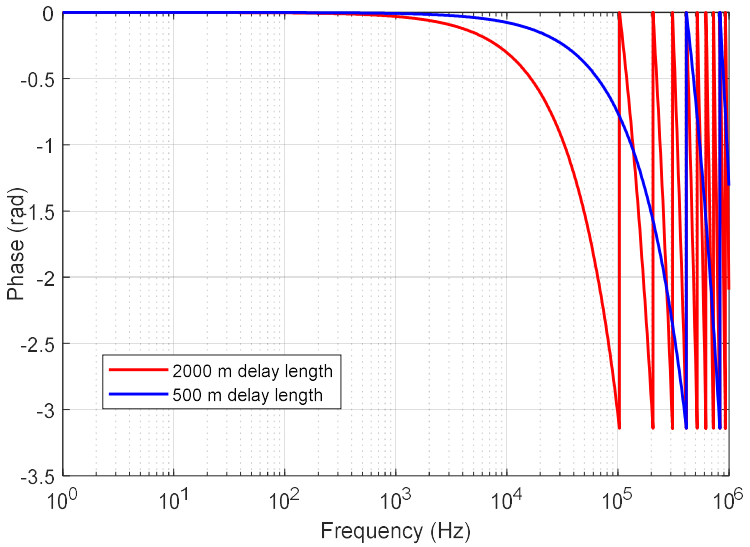

FIGURE 2.4: Interferometer normalized phase response to laser frequency noise of delay length as 500 m and 2000 m

2.2.3 Noise analysis

In practice, the length of fibre cannot be constant which introduces noise. The delay length $L_1 - L_2$ is a function of time:

$$L_1 - L_2 = L_{10} - L_{20} + (L_{10} - L_{20}) \sum B_i sin(m_i t). \quad (2.\ 22)$$

L_{10} and L_{20} are the average lengths of two arms, and B_i is the amplitude of the relative change of length difference. The fractional stability is:

$$\delta f/f = \delta(L_1 - L_2)/(L_1 - L_2) \tag{2. 23}$$

It shows that the frequency stability is proportional to the fluctuation of fibre delay length. To analyse the noise source for the laser stability, thermal induced thermal intrinsic noise, thermal drift noise, pressure induced phase noise and polarization perturbation would be introduced in following part while the vibration noise and acoustic noise which influence the fractional frequency stability at high frequency are not analysed here, as this thesis is focusing on the low frequency noise and long-term stability.

Thermal intrinsic noise

Thermal intrinsic noise is a fundamental noise in fibre interferometer, caused by the temperature fluctuation and dependent on the fibre material and parameters. Experiments show two different noise behaviour at different frequencies. For noise at high frequency (> 1kHz), it is described as thermal dynamic (or thermal conductivity) noise and has been studied based on fluctuation dispassion theorem by [76][77][78]. This theory believes that the noise comes from the spontaneous temperature fluctuation of the fiber refractive index, which is expressed as:

$$S_D(f) = \frac{2\pi k_B T^2 L}{\lambda^2 \kappa}\left(\frac{dn}{dT} + n\alpha_L\right)^2 ln\left(\frac{{k_{max}}^4 + \left(\frac{2\pi f}{D}\right)^2}{{k_{min}}^4 + \left(\frac{2\pi f}{D}\right)^2}\right)^2. \tag{2. 24}$$

The parameters are shown in TABLE 2.1.

For lower frequency noise, it presents as $1/f$ noise, and it is explained by the mechanical dissipation theorem, which show that the noise is from the spontaneous fluctuation of fibre length. Duan [79] used one-dimensional model analyse it and later experimentally proved by [80].

$$S_M(f) = \left(\frac{2\pi}{\lambda} n\right)^2 \frac{2k_B T L \phi_0}{3\pi E_0 A} \frac{1}{f}. \tag{2. 25}$$

Property	Notation	Value
Wavelength	λ	1550 nm
Temperature	T	300 K
Refractive index temperature coefficient	$\frac{dn}{dT}$	$9.2\times10^{-6}K^{-1}$
Effective refractive index	n	1.468
Thermal expansion coefficient	α_L	$5.5\times10^{-7}K$
Thermal conductivity	κ	1.37 W/(mK)
Thermal diffusivity	D	8.2×10^{-7} m^2/s
Boundary condition parameter	k_{max}	3.846×10^{-5} m^{-1}
Boundary condition parameter	k_{min}	3.846×10^{-4} m^{-1}
Bulk modulus of material	E_0	1.9×10^{10} Pa
Cross-sectional area of fibre	A	4.91×10^{-8} m^2
Loss of angle	ϕ_0	0.01

TABLE 2.1 The parameters of fibre noise calculation

Here we plot the calculated results of the thermal dynamic and thermal mechanical curves of a 100 m optical fibre based on above two theories. Results in [80] also indicates that optimizing the coating's parameter can reduce the intrinsic noise of fibres.

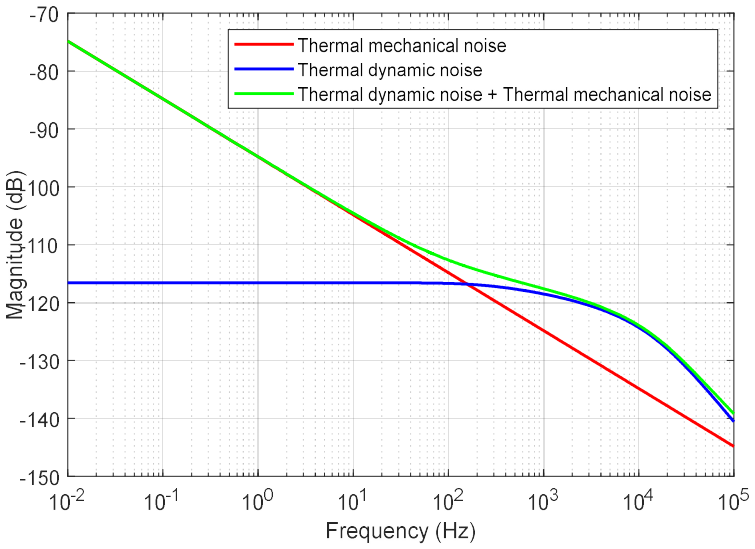

FIGURE 2.5: The intrinsic noise of fibres. Blue line is from Wanser [76] for noise at high frequency, red line is Duan's theory [79] for $1/f$ noise at low frequency. Green line is the sum of these two without offset.

Thermal drift noise

Different from the thermal intrinsic noise, thermal drift noise is the temperature fluctuation induced phase perturbation [81]. For a monochromatic light with wavelength λ, propagating through a piece of fibre with length L, the accumulated phase is:

$$\varphi = \frac{2\pi n_{eff} L}{\lambda} \tag{2. 26}$$

Due to the temperature change ΔT, the n_{eff}, L will be modified, and we obtain:

$$\frac{\Delta\varphi}{\varphi} = \frac{\Delta L}{L} + \frac{\Delta n}{n} = \epsilon_z + (\frac{\partial n}{\partial T})_\rho \Delta T + (\frac{\partial n}{\partial T})_T \tag{2. 27}$$

Here ϵ_z is axis strain in the core due to the length change, and ρ is the core density. The last part is the photoelastic effect which can be expressed by the Pockels coefficients. Then we obtained the thermal sensitivity:

$$\frac{\Delta\varphi}{\varphi\Delta T} = \frac{1}{n}(\frac{\partial n}{\partial T})_\rho + \frac{1}{\Delta T}\{\epsilon_z - \frac{n^2}{2}[(P_{11}+P_{12})\epsilon_r + P_{12}\epsilon_z]\} \tag{2. 28}$$

P_{11} and P_{12} are the Pockels coefficients of the core, and ϵ_r is the radial strain in the core Using the model proposed by N. Lagakos et al. [81], the thermal sensitivity of standard dual-coated fibre (SMF-28) is calculated as: 6.57×10^{-5} K^{-1}. we can also define the thermal sensitivity b normalizing the phase change of the fibre length:

$$S_\varphi = \frac{1}{L}\frac{d\varphi}{dT} = \frac{1}{L}\frac{d(2\pi nL/\lambda)}{dT} = \frac{2\pi}{\lambda}\left(\frac{dn}{dT} + \frac{n}{L}\frac{dL}{dT}\right) \tag{2. 29}$$

Here L is the length of fibre, T is the temperature, $\frac{dn_{eff}}{dT}$ is thermos optic effect of optical fibre, is measured to be 1×10^{-5} K^{-1}, and $\frac{1}{L}\frac{dL}{dT}$ is the thermal induced elongation of fibre along longitude axis. As the thermal expansion coefficient of silica is 0.55×10^{-6} K^{-1} [82], the thermal sensitivity of solid core fibre is about 48 rad/m/K at wavelength of 1550 nm. In later chapters, we will use this definition to describe fibre thermal sensitivity. Based on this definition, the thermal induced phase noise can be express as:

$$\Delta\varphi = \int_0^L \int_{T_1}^{T_2} S_\varphi \, dT dL. \tag{2. 30}$$

The thermal drift noise demonstrates dependency on temperature variation, the length of fibres, and the thermal sensitivity of fibres. As previously mentioned, extending the length amplifies the sensitivity of the frequency discriminator, making shortening the length an impractical solution. More effective approaches would involve minimizing temperature perturbations in the fibre system, such as implementing highly precise thermal control systems, refining the container's wall to diminish thermal reflections [45], winding the fibre spool in specific patterns to ensure uniform thermal distribution [83], or reducing the thermal sensitivity of fibres.

Pressure perturbation noise

When fibre is exposed in atmospheric environment, the pressure perturbation load on the fibre surface will leads to the strain in both radius and axis direction, which causes the length change and refractive index perturbation [86]. Like the thermal induced phase shift, and the pressure sensitivity can be defined as:

$$\frac{\Delta\varphi}{\varphi\Delta P} = \frac{1}{\Delta P}\left\{\epsilon_z - \frac{n^2}{2}[(P_{11}+P_{12})\epsilon_r + P_{12}\epsilon_z]\right\}. \tag{2. 31}$$

N. Lagakos et al. modelled the pressure induced phase change of standard coated optical fibre [86]. With their model, we calculated the pressure sensitivity of SMF 28 as -1.04×10^{-11}/Pa. Similarly, we simplified the definition of pressure sensitivity by normalizing the pressure-induced fibre phase perturbation to its length:

$$S_{\varphi\_P} = \frac{1}{L}\frac{d\varphi}{dP} = \frac{1}{L}\frac{d(2\pi nL/\lambda)}{dP} = \frac{2\pi}{\lambda}\left(\frac{dn}{dP} + \frac{n}{L}\frac{dL}{dP}\right), \tag{2. 32}$$

here $\frac{dL}{LdP}$ is the pressure induced fibre length change.

In some applications, the high-pressure sensitivity is preferred, such as hydrophone [87]. By employing a thick coating, the fibre pressure sensitivity can be improved by 38 times [86]. While used as frequency references, fibre interferometer is supposed to be as little by pressure perturbation as possible. [86] provided an effective way to reduce the pressure sensitivity by coating the fibre with high bulky modulus silica glass substrate or metal coting. For commercial fibre-based interferometer, housing it in a sealed box can minimise the pressure perturbation, further pumping the box to vacuum would provide the theoretically minimum pressure influence [51].

Fibre Rayleigh scattering

Fibre Rayleigh scattering describes the elastic scattering of light by particles due to the density fluctuation of silica glass, which are smaller than the wavelength of light. This effect can be employed in distributed fibre sensing [21]. The measured backscattering coefficient of SMF is −72 dB/m [88]. The Rayleigh scattering not only increases the attenuation of fibres, but also degrades the fibre-based applications, for example, the backscattering will be mixed with mirror-reflected light in a fibre Michelson interferometer sensor or frequency discriminator. Methods have been proposed to solve this problem [75].

Polarization perturbation

Silica fibre is believed to have a symmetric cross-section, standard single-mode silica fibres provide excellent spatial mode purity over long lengths. When unperturbed, they can also maintain the purity of the polarization state extremely well, down to the fundamental limit imposed by anisotropic Rayleigh scattering in the glass, however, when there is a stress applied such as bending, leads to slightly asymmetry of the fibre, the birefringence occurs. Polarization extinction ratio (PER) is defined to describe how much power is coupled from the principle linear polarization to the orthogonal direction:

$$PER = 10log_{10}\frac{P_{principle}}{P_{orthogonal}} \quad (2.\ 33)$$

For a 1 km-length fibre, the theoretical maximum PER is about 45 dB at wavelength of 1550 nm using parameters of a standard SMF [89].

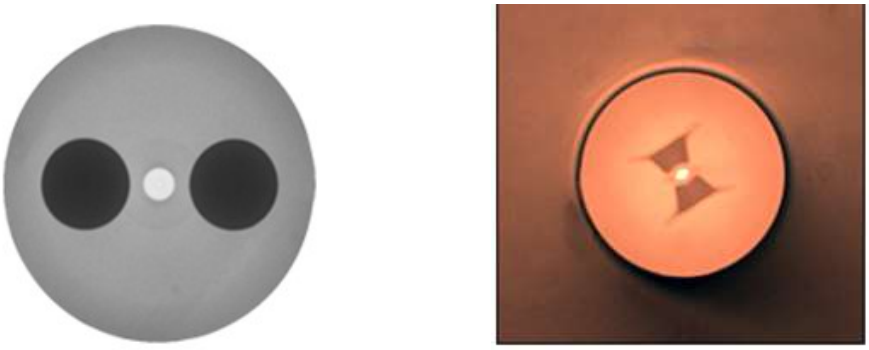

FIGURE 2.6. Cross-section of PM fibres (left: Panda PM; right: bowtie PM). These PM fibres apply stress along radius axis of the cross-section by inserting high TEC material symmetry to the core, leading to a distinct birefringence difference between two axes, maintaining the light linear polarization which is launched along the slow or fast axis.

To avoid this phenomenon, we can employ the polarization-maintaining (PM) fibre to construct the fibre interferometer [50] [90] , which can maintain the linear polarization of propagating light due to the distinct propagation constant between two axis. FIGURE 2.6 shows the cross-section of two typical PM fibres. However, there several problems when employing the PM fibres. For example, they are very sensitive to alignment and require the system be all-PM [91]. Besides, the PM fibres are very expensive due to the complex manufacture.

Alternative polarization control options in this scenario include polarization controllers or Faraday mirrors [69][70]. Polarization controllers utilize fibre birefringence induced through bending or coiling, enabling manipulation of output polarization by adjusting fibre angle and coiling However, this solution necessitates realignment and automated polarization control for extended operation. A more sophisticated approach is the application of a MI with FRMs. The underlying principle of the FRM is illustrated in FIGURE 2.7. Inside the FRM, incident light undergoes a 45° polarization rotation upon passing through the magnetic field, followed by reflection off the mirror. Subsequently, the light passes through the magnetic field again, causing an additional 45° polarization rotation, resulting in a polarization state perpendicular to the incident light. Back to the MI, the two waves at the output ports consistently maintain the same polarization state, yielding a maximal beat-note signal amplitude without reliance on polarization controllers. It's important to note that this approach is exclusive to the MI and has a limited bandwidth determined by the delay length.

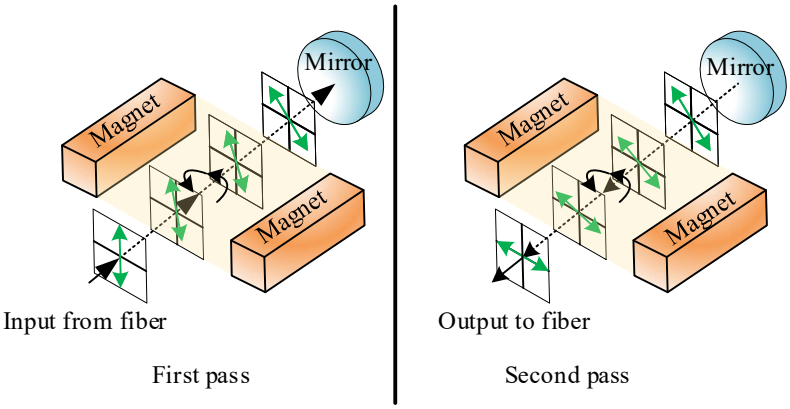

FIGURE 2.7: Principal scheme of the Faraday mirror rotator (45° rotation): light input to the rotator passes the magnetic field, its polarization is rotated 45°, then reflected and pass the magnetic field second time, it is rotated another 45°, which is perpendicular to the input direction.

Chapter 3 Background: Antiresonant hollow core fibres

In this chapter we introduce HCFs, and background knowledges are focusing on the antiresonant hollow core fibre (ARF) used in our interferometry. we firstly review the development of ARF, and introduce the guiding principle of ARF, review the connection methods. In the end we list the characters of HCF compared to solid core fibres.

3.1 Review of antiresonant HCF

Photonic bandgap hollow core fibres (PBGFs) are the early idea to guiding the light through hollow core by the photonic bandgap guidance principle [92], which require periodical air-glass structure, however, the attenuation was found to be limited by the mode-field overlap with glass cladding and the lowest loss of PBGF reported is 1.2 dB/km till now [93], far beyond the solid core single mode fibre which is about 0.15 dB/km. The alternative appeared when the Kagome HCF was invented [94], providing an extremely delicate structure of thin triangular-lattice struts with no cladding nodes, and the inhibited coupling of Kagome HCF leads to a potential of low attenuation.

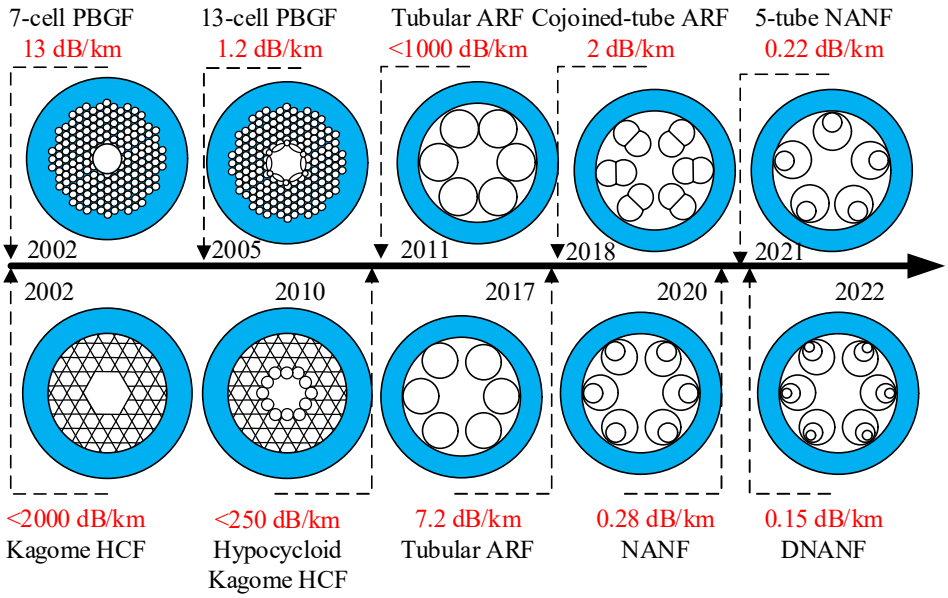

FIGURE 3.1: The development of HCF: from PBGF to ARF.

The first antiresonant guiding occurred in a hypocycloid Kagome HCF due to the negative curvature which represents the shape of the first ring around the core [97], leading to a decreased attenuation down to hundreds of dB/km. Removing the periodical triangle structures but keeping the

centre tubular lattice of hypocycloid Kagome HCF, the first ARF (tubular ARF) was fabricated by Belardi in 2013 [98]. This kind of ARF did not require a periodical lattice and worked just on the principle of antiresonance, of which the attenuation was reduced to 7.2 dB/km by separate the touching rings and optimizing the manufacturing [99]. FIGURE 3.2 shows the cross-section of PBGF and ARF (NANF).

In 2014, Belardi developed the crucial new concept of the nested ring design, which added a second smaller hollow tube inside each tube in the negative-curvature layer, reduced light coupling from the core into the cladding, and thus reduced fibre attenuation [100]. This structure was latter modified by Poletti which was called as NANF [84]. Removing the nodes where tubes touched could give the NANF fibre a low-loss antiresonant band an octave wide and suppress high-order modes well enough to make the fibre effectively single mode. His analysis indicated that the attenuation in NANF fibres due to leakage, surface scattering and bending could be lower than for conventional solid fibres. Due to the negligible optical field overlap with glass leading to low surface scattering loss, the attenuation of this ARF is mainly limited by the confinement loss and envisioned to eventually surpass the attenuation of other HCF and even that of SMF.

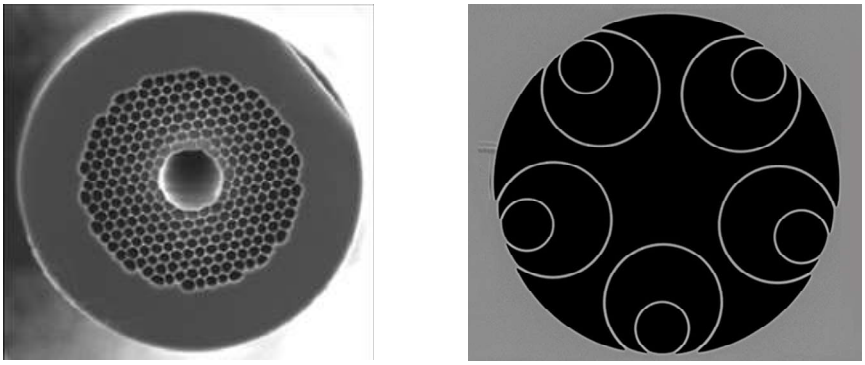

FIGURE 3.2: Scanning electron microscopy (SEM) photos of PBGF and NANF

In 2018, Gao et. al reported her conjoined-tube fibre (CTF) which has a minimum loss of 2 dB/km at 1512 nm [101], and in the same year, Optoelectronic Research Centre (ORC) in the University of Southampton reported minimum loss of only 1.3 dB/km at 1450 nm in the NANF fibre [102]. Attributable to improvements in tube handling, preform fabrication and pressurization, which improved uniformity along the fibre length as well as cross-sectional, ORC reported a loss of 0.28 dB/km between 1510 and 1600 nm, and close to 0.3 dB/km between 1500 and 1640 nm for a 2.8-km fibre in 2020 [103]. In 2021, the record low loss was improved further to 0.22 dB/km from 1625 nm to 1640 nm for a 2.2 km fibre which was achieved by moving from the 6-tube NANF into a 5-tube NANF [104]. Recently, a new record low loss was reported to be 0.174 dB/km at C band with a structure which adds an extra smaller hollow tube inside each second tube in NANF, which is called double nested antiresonant nodeless fibre (DNANF) [105]. Although the attenuation is still higher

than the lowest value of Ge-free SMF, it already surpasses the attenuation of conventional germanium-doped SMF in the O and C bands.

3.2 Antiresonant guiding principle

Structure of ARF has been shown in figure, which consists of inside thin capillaries and thick membrane. Assuming the thin capillaries are of the same thickness d and refractive index n, to understand the guidance mechanism of ARF, we consider a piece of glass sheet part of the inside capillary shown in FIGURE 3.3.

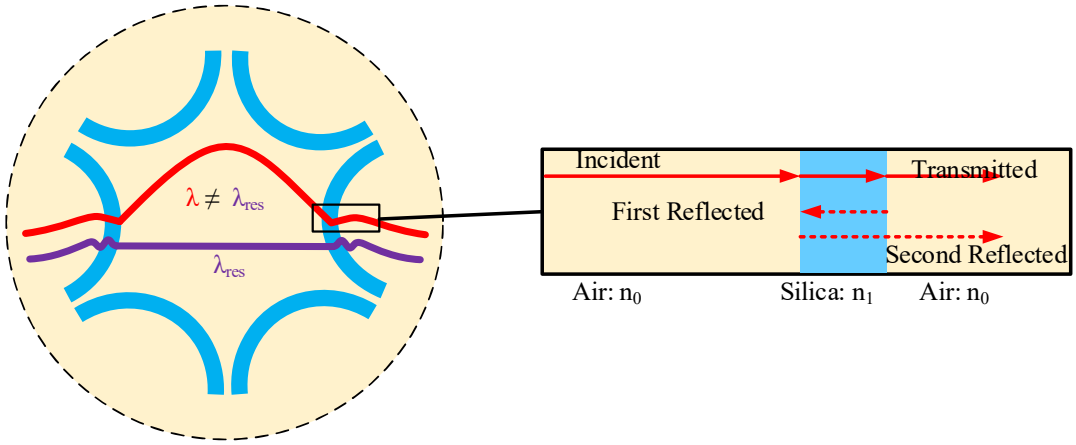

FIGURE 3.3: Schematic mechanism of anti-resonant hollow core fibre

As the light travels through mostly in the centre air core, the longitudinal propagation constant is expressed as $\beta = n_0 k$ (k is the wave vector). When phase matching occurs between the air mode and glass mode within the structure, transverse light propagates through the glass sheet comprising two light waves: the incident light wave that travels directly through the glass, and the second reflected light, which can be understood as a series of events involving the incident light passing through the glass-air interface, followed by the initial reflection at the air-glass interface, ultimately resulting in the second reflected light. Given the propagation constant of transversal mode $k_t = \sqrt{k^2 {n_1}^2 - \beta^2} \approx k\sqrt{{n_1}^2 - {n_0}^2}$, the phase difference between two light waves is $2k_t d$. If the phase difference $2k_t d = 2m\pi, m = 1,2,3,\ldots$, which is called as resonant condition, the two waves will interference constructively out of the glass sheet. Thus, the low loss operational wavelength sits between the resonant wavelengths [84]:

$$\lambda_m \approx \frac{2t\sqrt{n^2 - 1}}{m}, m = 1,2,3,\ldots \quad (3.1)$$

It indicates the transmission band would be separated in several orders, seen in FIGURE 3.4.

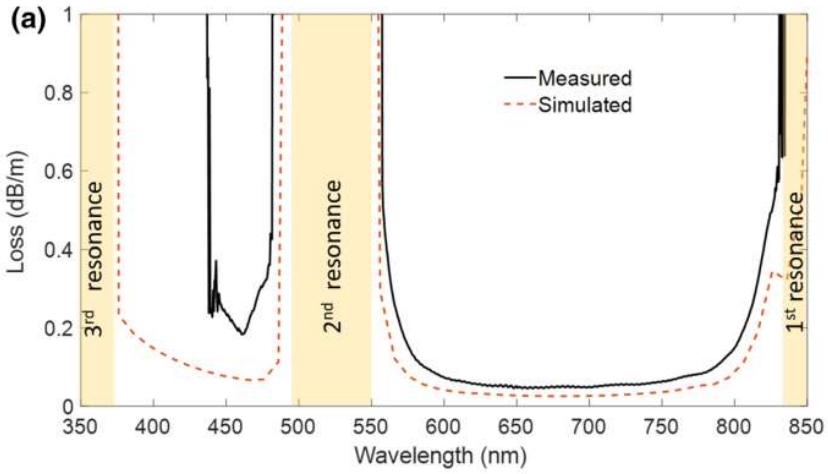

FIGURE 3.4: The transmission spectrum of antiresonant hollow core fibre from [85]

3.3 Connection between HCF and SMF

Today's low-loss HCFs have central hole of ~70-90 µm, which contains thin tubes that surround its core that typically has ~30 µm diameter, it is relatively lager than SMF and gives challenges when connecting HCF with SMF system, such as mode filed mismatch and Fresnel back-reflection. Limitation of coupling between SMF to HCF was studied in [106]. The mode field diameter (MFD) of HCF is believed to be 70% of the core size, which is about 20-30 um, while SMF-28 has MFD ~9 um. This huge mode mismatch leads to not only the power loss but also unwanted high order mode (HMD) coupling. An effective way is to employ an optical mode adaptor between SMF and HCF, Jung designed a small device (7 cm) using optical collimation techniques shown in FIGURE 3.5 [107]. Here the micro-lens is employed as mode adapter (MA) and sealed with SMF and HCF in a glass tube, providing 0.53 dB total insertion loss.

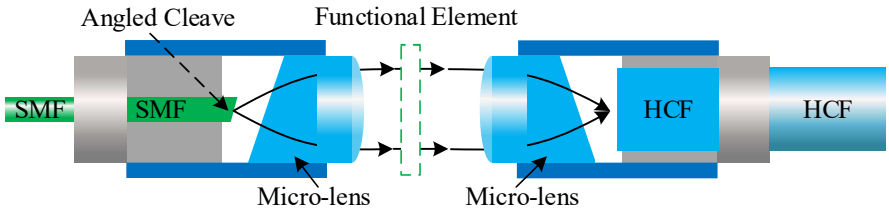

FIGURE 3.5: A schematic of 2-port hollow-core fibre components based on micro-optic collimator assembly (adapted from [107])

A short piece of gradient refractive index fibre (GRIN) can also be used as micro lens [108]. As shown in FIGURE 3.6. The GRIN is first spliced to the SMF, and then fixed in a fibre array, then the GRIN is polished to the length where the MFD reaches maximum, also called as 'quarter pitch', due to the similar size between MFD of GRIN and HCF, a low insertion loss (0.3 dB) is achieved.

Splicing these two fibres under CO_2 laser splicers, a robust connection without neglectable extra loss (<0.1 dB) can be realized.

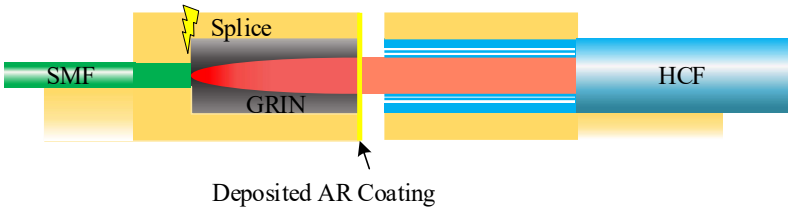

FIGURE 3.6: Schematic of the connection using a short piece of GRIN as mode adaptor.

Without inserting other optical elements, tapering the SMF to enlarge the MFD is another option [109][110]. Tapering SMF to small diameter, the mode will leak from core to silica leading an expanding MFD [109]. Cleaving the tapered fibre at position where the MFD is equal to that of HCF, and then inserting the tapered thin fibre end into the hollow core of HCF, gluing them together, gives low loss as 0.2 dB. Or employing the thermal expansion core SMF and reversely tapering the fibre to enlarge the core size, it provides the matching of both the size of outer diameter and MFD between SMF and HCF [110]. Besides the low insertion loss (0.88 dB), it also enables the splice-connection between SMF and HCF, which can be significant for some applications.

Despite the mode mismatching induced insertion loss, the Fresnel reflection also contributes to the total connection loss. The mechanism is shown in FIGURE 3.7. When light incidents from tapered SMF or MA (solid silica, n = 1.45) to HCF's hollow core (air, n = 1), Fresnel reflection happens on the end-face due to the refractive index difference, which is about 4% (0.15 dB). This strong Fresnel back-reflection will limit the applications of HCF, for example, when propagating high-power laser through HCF, this 4 % power loss will happen at the interface between SMF and HCF, furthermore, the Fresnel reflection will cross talk with back propagating signals, such as the Rayleigh scattering in HCF-based optical time domain reflectometry (OTDR) testing or the reflected signal from end mirrors in a HCF based MI.

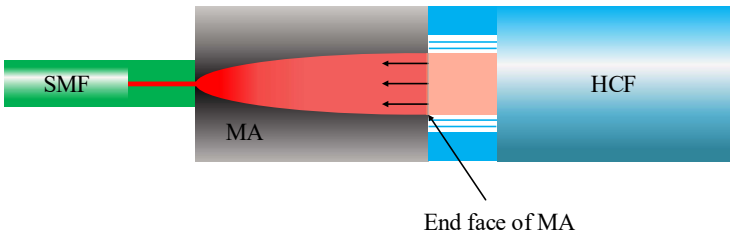

FIGURE 3.7: Schematic of Fresnel reflection from end face of MA to HCF.

Depositing anti-reflective (AR) coating on the end surface of MA or tapered SMF can reduce this strong reflection effectively. [111]achieved the glued connection with -45 dB low back-reflection and 0.15 dB insertion loss by coating the GRIN end-face. Employing high temperature toleration material (Ta_2O_5/SiO_2) on the end-face of reversely tapered SMF, which can survive after splicing, achieving the splice connection with -28 dB low reflection meanwhile <0.3 dB insertion loss. As mentioned above, GRIN with length of quarter pitch can be a MA when spliced with SMF, and easily spliced to the HCF, this method leads to a both mechanically stable and low loss connection, which has been employed in most of the connections in this thesis. Rather than a flat cleaved end of GRIN, cleaving the GRIN with small angle can reduce the reflection dramatically. This angled-splicing technique has been reported by [112] which provided -40 dB low back-reflection by cleaving the GRIN within only 2.2°. This small angle was easily achieved on HCF, allowing a robust splice-connection between HCF and SMF. In this thesis, this method is employed to construct the MI, avoiding the crosstalk of back-reflections from SMF-HCF interface and FRM.

3.4 Characters of HCF

HCFs guide the light mostly through its air core, and due to the characters of air, they naturally have several evident properties, such as low latency, low dispersion, high nonlinear threshold, and so on and due to these unique advantages, recently they are wildly used in many research applications, such as optical communication [113], gas sensing [114], time and frequency transfer [115], high power laser transmission [116] and so on. Here we will briefly introduce the backscattering, thermal phase sensitivity, pressure sensitivity of HCF which are very important parameters for our interferometer.

3.4.1 Backscattering

Backscattering limits the attenuation of low-loss HCF and theory has been reported recently [117]. The scattering is mainly from three parts: the Rayleigh scattering from air molecules in the hollow area (−100 dB/m at 1550 nm), the perturbation of glass refractive index which is very small as less than 0.1 % of light propagated though it, and the roughness of inside membrane. As [118] shows, the air molecules scattering contributes mostly for the total scattering, which then was measured by a none phase-sensitive OTDR system and reported to be 30 dB lower than SMF (see FIGURE 3.8).

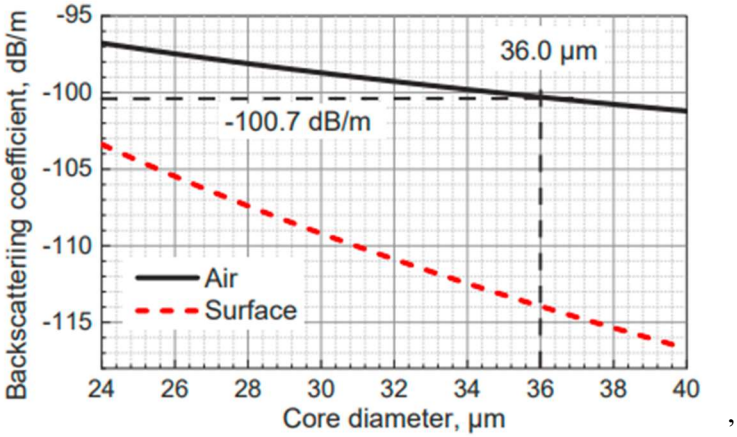

FIGURE 3.8: The Back scattering coefficients of the air and surface roughness in HCF with different core size [118]

To characterize the contribution from the surface roughness, optical frequency domain reflectometer (OFDR) was employed and about 40 dB lower (-115dB/m) backscattering than standard SMF was reported [119].

3.4.2 Pressure sensitivity

The fibre core refractive index change of SMF due to the opto-elastic effect has opposite sign to the pressure induced length change, cancelling part of the elongation effect [86], while in HCF, the air refractive index changes very little to the pressure, leading to a higher-pressure sensitivity which is dominated by the length change of silica cladding and coatings.

Pang et al. proposed a method to calculate the pressure sensitivity of PBGF, and designed HCF with thicker coatings to increase the sensitivity [121]. Though the guiding principle is different between PBGF and ARF, the pressure sensitivity can be calculated by the same method as they both have no solid cores where the opto-elastic effect happened, thus only the pressure induced length perturbation will be considered, the calculated pressure phase sensitivity $\frac{\Delta\varphi}{\varphi}/\Delta P$ of ARF is about 10^{-11} Pa^{-1}, here φ denotes the total phase delay of the fibre and $\Delta\varphi$ denotes the phase changes of the fibre delay due to the pressure change ΔP.

Chapter 4 Principle and prototype of thermally insensitive compensated fibre delay-line interferometer

In this chapter, we introduce the principle and prototype of the thermally insensitive fibre interferometer. First, we present the principle by deriving function of the thermal sensitivity of fibre delay-line interferometers and give the structures. Subsequently, we simulate thermal distributions of different winding patterns with the finite element analysis software to prove the method. Later we introduce the fabricated prototype of the thermally insensitive fibre interferometer and experimental setups, characterize the prototype by measuring the thermal induced phase change.

4.1 Principle of thermally insensitive compensated delay-line fibre interferometer

4.1.1 Thermal sensitivity of delay-line interferometer

Eq. (2. 30) shows the accumulated phase of a piece of fibre, when it comes to a delay-line fibre interferometer, such as a fibre MZI, providing a temperature variation, the thermal sensitivities of two fibre arms determine the perturbated accumulated phase as:

$$\Delta\varphi\left(T, L_1, L_2, S_{\varphi B1}, S_{\varphi B2}\right) = \int_o^{L_1}\int_{T_1}^{T_2} S_{\varphi 1} dT dL - \int_o^{L_2}\int_{T_1}^{T_2} S_{\varphi 2} dT dL, \qquad (4.\ 1)$$

$S_{\varphi 1}$ and $S_{\varphi 2}$ are the thermal phase sensitivities of two fibres arms, separately.

To simplify (4. 1), the fibre thermal phase sensitivity is assumed to be temperature independent which can be achieved when the temperature varies in small range (e.g., ±0.01 K, easily controlled by a common thermal system), thus we have:

$$\Delta\varphi\left(T, L_1, L_2, S_{\varphi B1}, S_{\varphi B2}\right) = \int_o^{L_1} S_{\varphi 1}(T_2 - T_1) dL - \int_o^{L_2} S_{\varphi 2}(T_2 - T_1) dL\,. \qquad (4.\ 2)$$

It is it is a reasonable assumption that the temperature along the fibres could be the same which depends on the thermal distributions because we can wind the two arms tightly together and control the surrounding temperature as uniform as possible. (4. 2) can be simplified as:

$$\Delta\varphi = (T_2 - T_1)\left(S_{\varphi_1}L_1 - S_{\varphi_2}L_2\right). \quad (4.\ 3)$$

Typically, the arms of interferometer are constructed using the same fibre resulting the same thermal phase sensitivity, $S_{\varphi_1} = S_{\varphi_2} = S_\varphi$, therefore, the phase perturbation can be further simplified as:

$$\Delta\varphi = \Delta T \Delta L S_\varphi. \quad (4.\ 4)$$

Where $\Delta T = T_2 - T_1$, $\Delta L = L_1 - L_2$. To normalise the phase change to the fibre delay length, fractional thermal phase response is defined as:

$$\frac{\Delta\varphi}{\varphi} = \frac{S_\varphi \Delta T \lambda}{2\pi n}, \quad (4.\ 5)$$

here n is the refractive index of fibre.

4.1.2 Structure of thermally insensitive fibre interferometer

It is hard to make (4. 4) be zero at room temperature, as the temperature perturbation ΔT can never be zero, and there is no fibre reported to be thermally sensitive at room temperature. However, the fibre interferometer is assumed to be made from one single fibre, both delay arm and reference arm. Considering two fibres with different thermal phase sensitivity, one has lower sensitivity S_{φ_d} can be employed as delay with longer length L_d, and the other one with higher sensitivity S_{φ_c} forming the reference arm is short, L_c, and used to compensate the thermal induced accumulated phase change from delay arm. The thermal induced phase difference can be expressed as:

$$\Delta\varphi = \frac{2\pi}{\lambda}\Delta T\left(S_{\varphi_c}L_c - S_{\varphi_d}L_d\right). \quad (4.\ 6)$$

To make $\Delta\varphi = 0$, the right part inside bracket should be zero,

$$S_{\varphi_c}L_c = S_{\varphi_d}L_d, \quad (4.\ 7)$$

or:

$$\frac{L_c}{L_d} = \frac{S_{\varphi_c}}{S_{\varphi_d}}. \tag{4. 8}$$

It means that when the length ratio between these two fibres equals to the reciprocal of their thermal sensitivity's ratio, the thermal induced phase change of this compensated interferometer at room temperature, under small temperature variation, can be zero, in other word, this interferometer can be thermally insensitive at room temperature.

Based on this compensation method, HCF with 2.2 rad /m/K thermal sensitivity is employed as the delay arm and compensated by SMF in the other arm, 48 rad /m/K, between which the length ratio is about 21.5. There are two kinds of compensate delay-line fibre interferometers MZI (see FIGURE 4.1) and MI (see FIGURE 4.2).

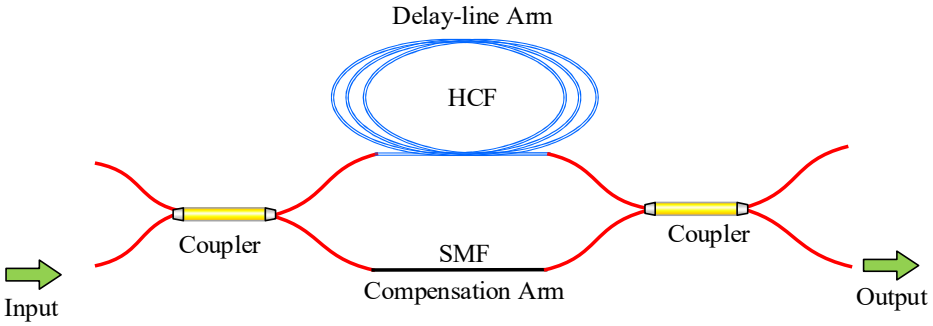

FIGURE 4.1: Schematic of the compensated fibre MZI, it consists of couplers, HCF as delay-line arm, and SMF as compensation arm.

Typically, MZI is formed with input coupler, main arms, and output coupler. To solve the polarization degradation problem, it can be updated to Michelson fibre interferometer by replacing the output coupler with two Faraday rotator mirrors (FRMs), see FIGURE 4.2.

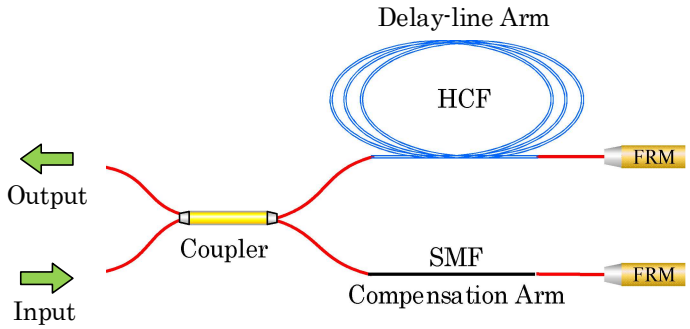

FIGURE 4.2: Schematic of the compensated fibre MI, it consists of coupler, HCF, SMF and FRM.

4.2 Simulations of winding patterns

As mentioned above, the compensation method assumes that fibres (HCF and SMF) in two arms experience the same temperature, which is hard to realize in practice due to the length difference, especially for the interferometer with long delay. It means that even when the interferometer is theoretically thermally insensitive by the compensation between HCF and SMF (HCF is 21.5 times longer as SMF), the thermal instability of two arms will cause phase unstable with thermal perturbation. To show this effect and give some strategies to achieve the target that 1000 times less thermal sensitive than SMF-based interferometer, three possible winding patterns are proposed and simulated in COMSOL. Finite element analysis software is powerful in the thermal effect simulation, so as to in the study of temperature variety of fibre coil Thermal unevenness is defined by calculating normalized phase difference perturbation between two fibre arms caused by the thermal distribution:

$$U_t = \frac{S_{\varphi 1} \int T_1 dl_1 - S_{\varphi 2} \int T_2 dl_2}{\Delta l \Delta T} \tag{4. 9}$$

here l,are the length of two arms, T is the temperature along the fibre and S_φ is the thermal sensitivity of fibres. It has the same unit of normalized thermal phase sensitivity to make an easier comparison. Three possible winding patterns are designed shown in FIGURE 4.3. In these patterns, HCF is winding in the same pattern, a hollow cylinder, while the SMFs are different. SMF in pattern1 is wound as a circle in the mid of HCF, in pattern2, it is wound from the top to the bottom of HCF in a spiral style, and in pattern3, SMF is like in patern1 while the position is from the top to the bottom of HCF.

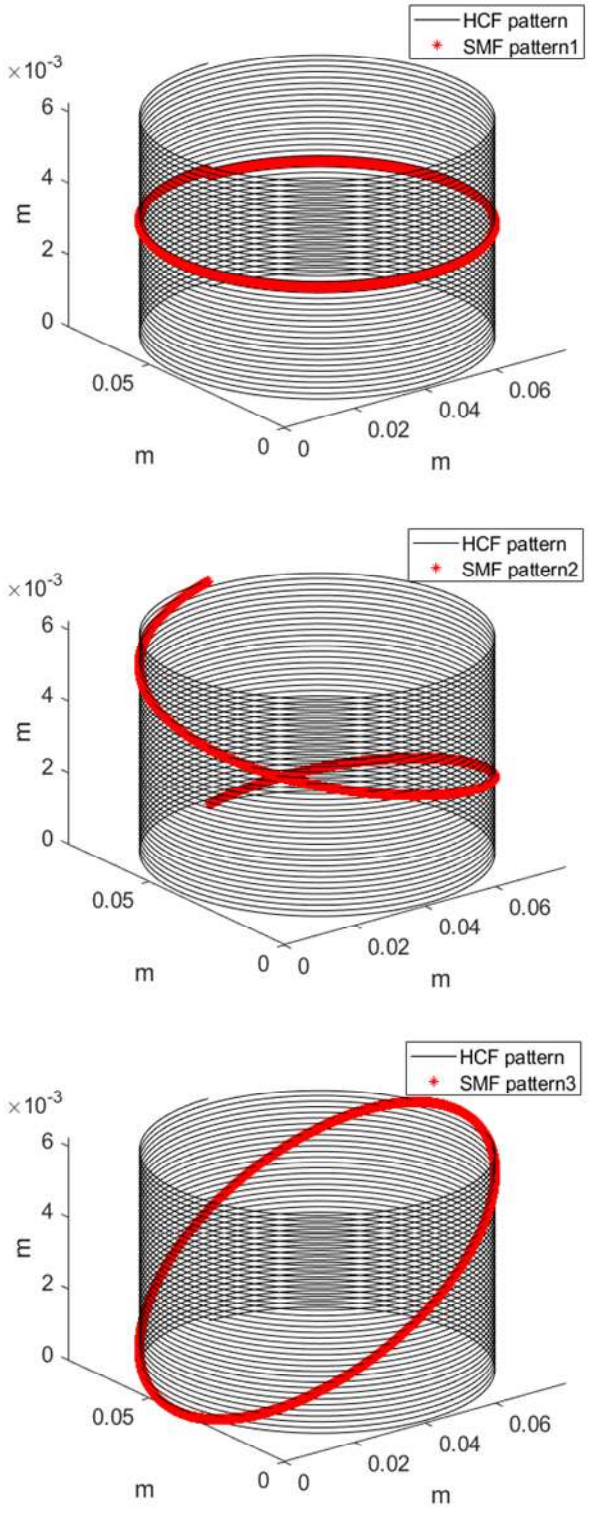

FIGURE 4.3: Three winding patterns designed for smaller temperature difference between HCF (black line) and SMF (red line)

Then these three winding patterns are then built in COMSOL, FIGURE 4.4 presents the 3D module of pattern2.

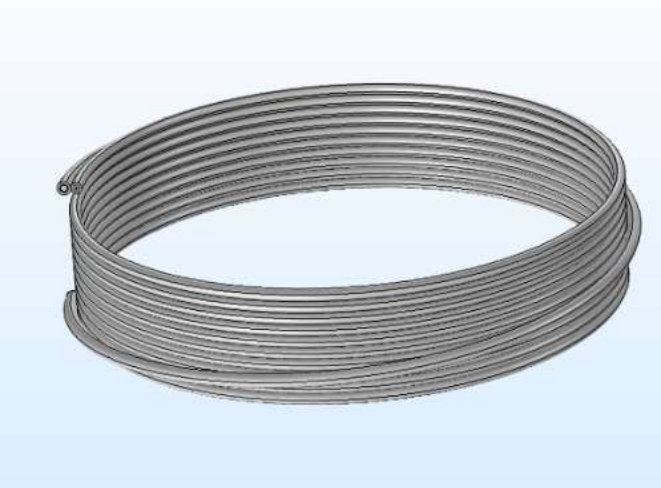

FIGURE 4.4: 3D module of fibre coil composed of HCF and SMF (built in COMSOL)

Parameters of the COMSOL model are shown in TABLE 4.1. It is a simplified module which simulated only the temperature distribution of the fibre coil, the elongation of fibres here is neglected for it has little influence on the thermal unevenness of the interferometer.

Definition	Parameter	Function/value	Value in SI
Turns of SMF coils	m	n/20	2
Turns of HCF coils	n	40	40
Thickness of air	t_air	1 cm	0.01 m
Thickness of coil pitch	t_pitch	2 μm	2 μm
Radius of SMF	r_smf	125 μm	125 μm
Radius of HCF	r_hcf	180 μm	180 μm
Radius of HCF coils	r_hcf_coil	3/4/5/7/10 cm	3/4/5/7/10 cm
Height of HCF	h_hcf	n×2×(r_hcf+t_pitch)	0.020384m
Height of SMF	h_smf	m×2×(r_smf+t_pitch)	0.001016 m
Radius of SMF coils	r_smf_coil	r_hcf_coil+r_hcf+r_smf	0.030305 m

TABLE 4.1: Main parameters used in COMSOL

To simulate an environmental thermal perturbation, the module of the interferometer is put into a virtual container filled with air shown in FIGURE 4.5.

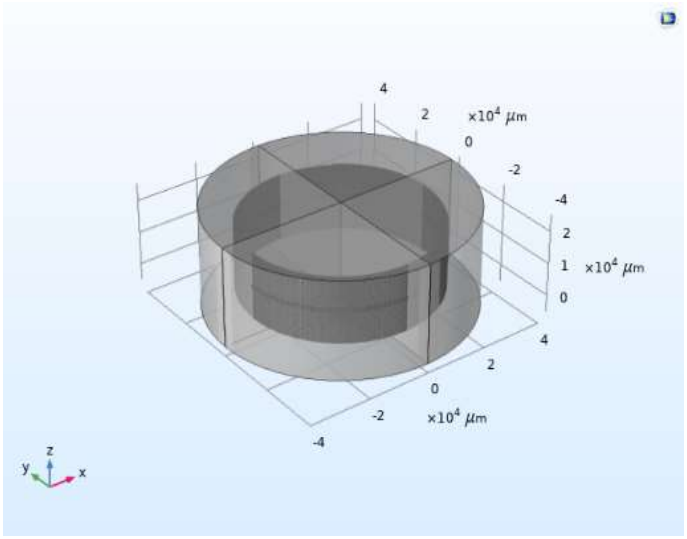

FIGURE 4.5: Fibre coil with air surrounded in COMSOL, which is in the centre part of air. The air container is 2 cm larger than that of fibre coil in thickness and height.

The thermal perturbations are designed to be three situations (Top, Side, Edge) as shown in FIGURE 4.6.

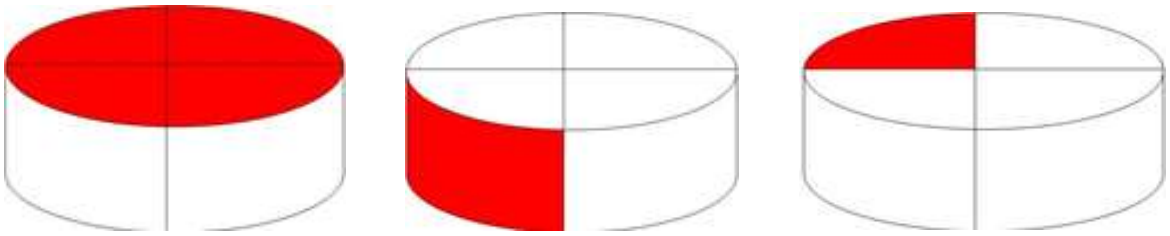

a b c

FIGURE 4.6: Scheme of three different thermal situations in COMSOL simulation. The cylinder represents the air around the fibre spool, white area is set as constant temperature (20 ℃), and red boundary is set as a higher temperature (30 ℃) to create a thermal fluctuation with time. Top (a): only top boundary Side(b): only a quarter of side boundary; Edge (c): only a quarter of top boundary.

The initial temperature of fibre spool and surrounding air is set to 20 °C, while the boundaries of three initial perturbations (shown in red in Fig. 11) are 30°C and the rest of the boundaries of these three situations are set as isolation. We can image that the temperature of the fibres will increase from 20 ℃ to 30 ℃, and the temperature of SMF and HCF is recorded every 2 seconds.

Three fibre coil patterns models with same radius (3 cm) are run in COMSOL, and the temperature distributions of the fibres are acquired. Using the definition of thermal unevenness (4. 9), we can compare these three patterns with each other, and can also have a comparison between the

thermal stabilities of compensated interferometer and SMF-based interferometer. The calculated thermal unevenness is shown in FIGURE 4.7.

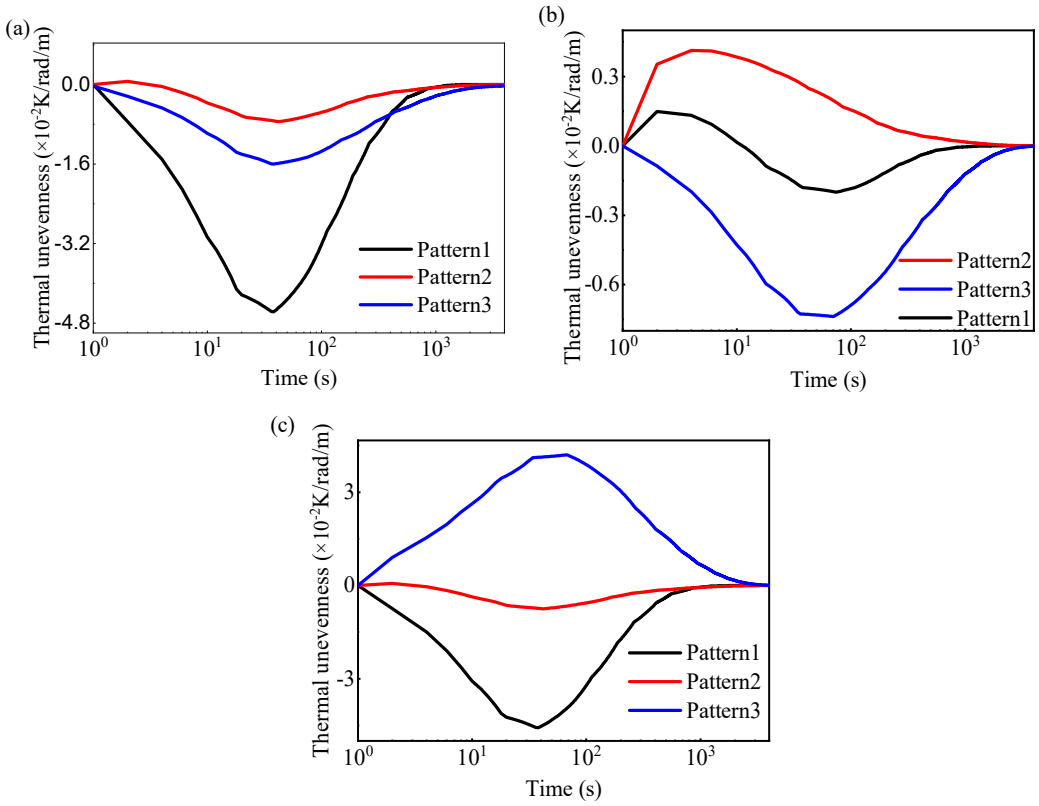

FIGURE 4.7: Thermal unevenness of three patterns in three different initial thermal situations (a: Top, b: Side, c: Edge). At start, thermal uniformities of three patterns are all zero. The negative and positive value of unevenness is due to the thermal time distribution difference of SMF and HCF, and here we consider the absolute value only.

For clarity, the time axis is shown in semi-log scale. In FIGURE 4.7, at the start point, the thermal unevenness of three patterns is zero as we set the ratio of length equals to that of thermal sensitivities between HCF and SMF, and then the unevenness changes, reaches the maximum, and with the temperature distribution slowly becoming uniform, the thermal unevenness goes back to zero again when the temperature in the whole container reaches 30 ℃ everywhere. To achieve our target of thousands of times better than the normalized thermal sensitivity of SMF based interferometer, the change of unevenness should be less than 3.3 $\times 10^{-2}$ rad/m/K. From the figure, in 10 ℃ thermal perturbation, the unevenness of patterns2 can still be under than 3.3 $\times 10^{-2}$ rad/K/m, the result means with winding pattern2, the thermal phase shift of the compensated interferometer caused by the thermal perturbation can be 1000 times less than that of SMF-based interferometer.

4.3 Fabrication of prototype

After the simulation, we fabricated the prototype of the compensated delay-line fibre interferometer. The structure is the same as in FIGURE 4.1, which is a compensated MZI. Compared to compensated MI, MZI suffers less back-reflection from the interface between SMF-HCF and is easier to fabricate. HCF here used is a 10.84 m dual-coated NANF, and SMF is SMF-28. Two 2×2 SMF couplers are used to form the interferometer. To integrate the HCF into the SMF system, we used the GRIN as mode field adaptor, spliced the HCF to SMF following the step shown in FIGURE 4.8.

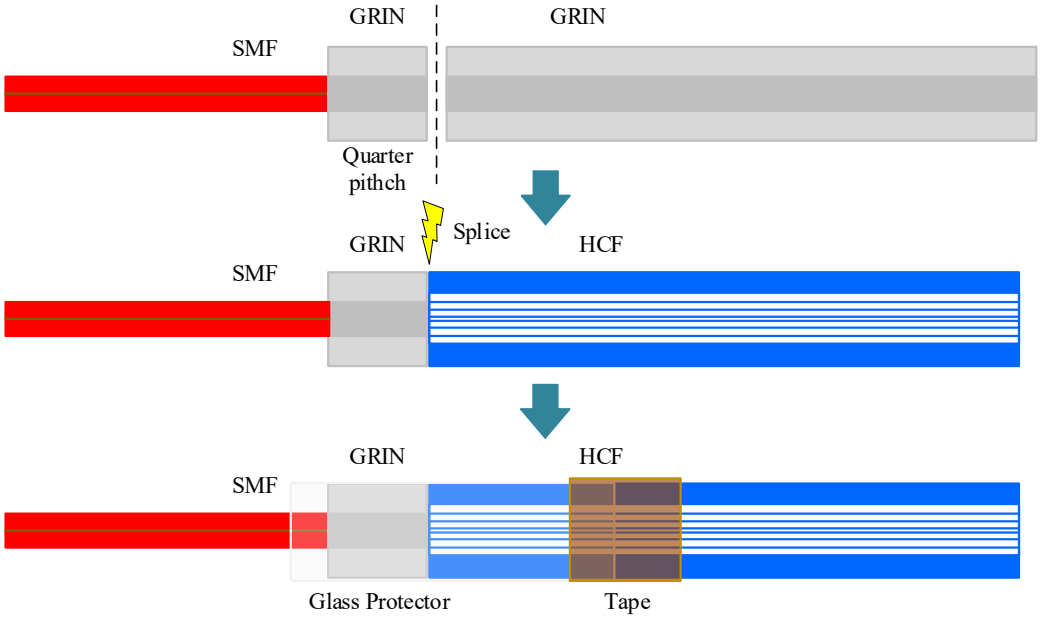

FIGURE 4.8: Schematic of the connection between HCF and SMF

One arm of the input coupler is spliced to the GRIN, which is then cleaved to ¼ length of the period (quarter pitch, shown in FIGURE 4.9). One end of HCF is cleaved and spliced with the cleaved GRIN, the connection was protected with a glass capillary and fixed with tape. Typically, thermal shrink protector was used to protect the spliced point, however, here it would be adventurous as thermal shrink protector has complex thermal sensitivity and could ruin the compensation. The other end of HCF is spliced to the one arm of the output SMF coupler in the same way. SMF in the compensation arm is connected to the SMF couplers following common splicing method which is available in commercial splicers, and all spliced points are protected by the same glass capillaries to cancel the effects. The total insertion loss of two spliced point is about 1 dB.

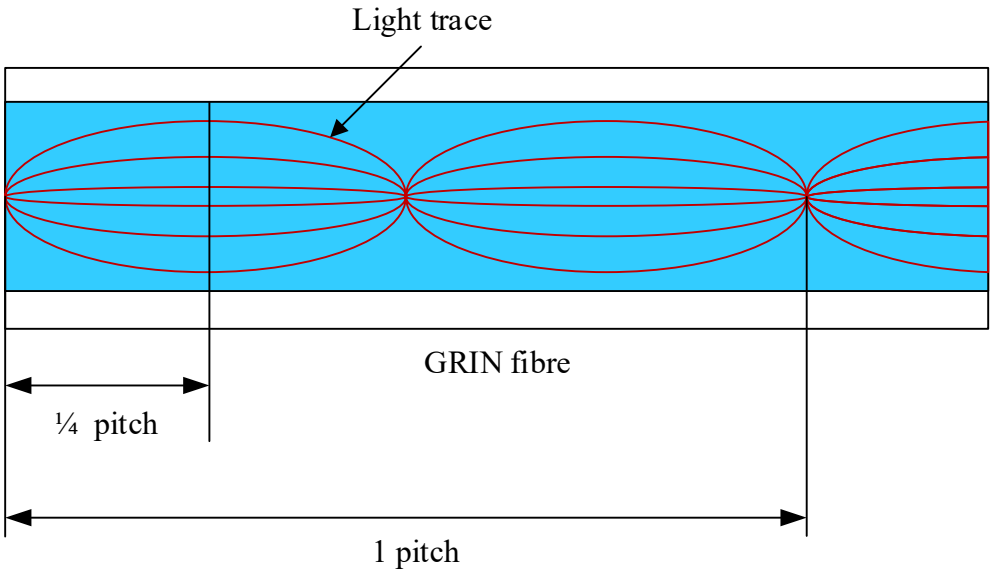

FIGURE 4.9: Schematics of the light traces in GRIN fibre.

To prove the idea of compensation, our plan is to first splice 0.78 m SMF on the other arm of the interferometer, and then decrease the length of SMF to be close to the theoretical compensated length which is about 0.54cm (20 time shorter than the HCF). Note here the pigtails of couplers are cut in short length (< 20 cm) and balanced in two arms to avoid the residual thermal response. HCF and SMF are coiled together with a diameter of 14 cm to experience the same temperature distribution thus makes the two arms has the thermal response at the same time, following our assumption.

4.4 Experiment setup and results

A well-controlled thermal chamber is necessary to characterize the thermal performance of the fabricated fibre interferometer. Here an octagon structure chamber was employed, which has 10 Peltier thermo-electric coolers (TECs) to control its temperature, one on the top, one on the bottom, and another eight on its sides, ensuring the thermal constant to be similar in different directions shown in FIGURE 4.10 (a). A control thermistor is placed in the chamber and fixed on the one side of the octagon, closed to the centre of where the TEC is placed, which is used to record the temperature for thermal stabilization. The temperature is read by a micro-controller, which stabilizes the temperature by controlling the current coupled into the TECs based on proportional-integral-derivative (PID) control method. The temperature range of this thermal control system is from 5 ℃ to 80 ℃ with precision ± 0.01K, meets our requirement as the goal is to make a thermally insensitive fibre interferometer at room temperature.

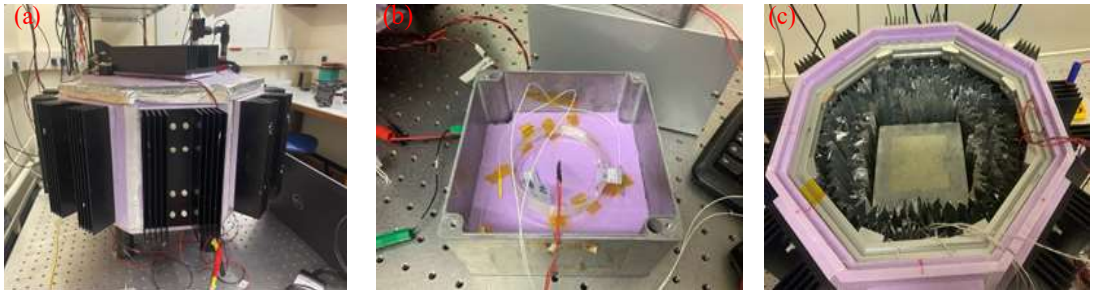

FIGURE 4.10: Photographs of the thermal chamber and metal box: (a) The outer appearance of the thermal chamber; (b) small metal chamber where compensated MZI is placed in; (c) the metal box in the opened thermal chamber which is filled with fold Aluminium film in space area.

Rather than being directly placed into the thermal chamber, the fabricated interferometer is firstly housed in a metal box (15 cm × 15 cm × 10 cm), where there is a piece of insulator (15 cm × 15 cm × 1 cm, see FIGURE 4.10 (b)) on the bottom to avoid the contact between the fibre interferometer and the box, providing a better thermal constant and making the temperature distribution on the interferometer more uniform. A thermistor is placed in the centre of the fibre spool to record the temperature of the box, as well as the interferometer because we believe the temperature gradient is too small to be considered inside the box. Then the box with interferometer inside was placed in the centre of the chamber, and the gap are filled with fold Aluminium films to make the temperature distribution furthermore uniform, shown in FIGURE 4.10 (c).

FIGURE 4.11 gives the positions of fibre spools.

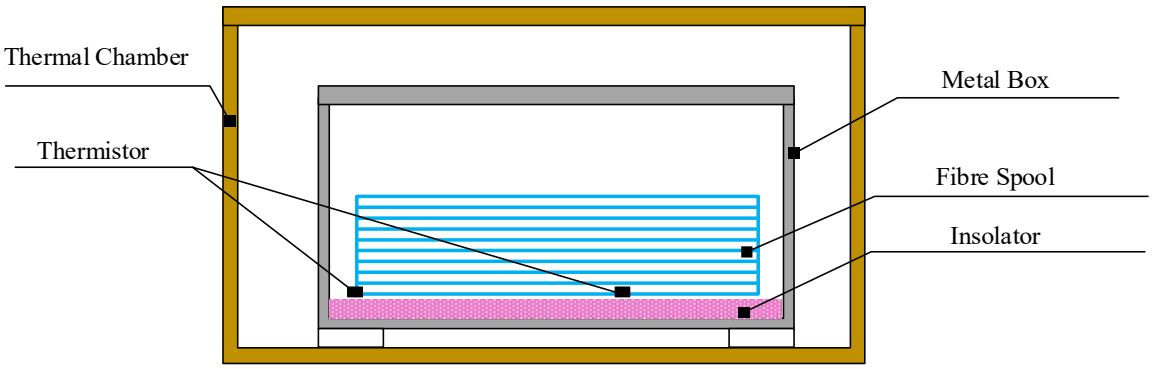

FIGURE 4.11: Schematic of the alignment of fibre spool and thermal chamber.

The thermal sensitivity of the fibre interferometer is measured by calculating the thermal accumulated phase change with the temperature changing from one stabilized stage to another. The light source is a narrow linewidth laser (RIO Orion from NuFern, emitting at 1558 nm, linewidth < 1 MHz), as the delay-line is about 10 m (30 MHz), such narrow linewidth is enough for our

measurement (while for later work, it will be locked to a carrier envelope offset stabilized comb (CEO-stabilized comb) to have a better stability). By setting the stabilization temperature of the thermal chamber, the inside box temperature is changed, and the thermal induced interferometric signal is detected by the photodetector. The scheme is shown in FIGURE 4.12.

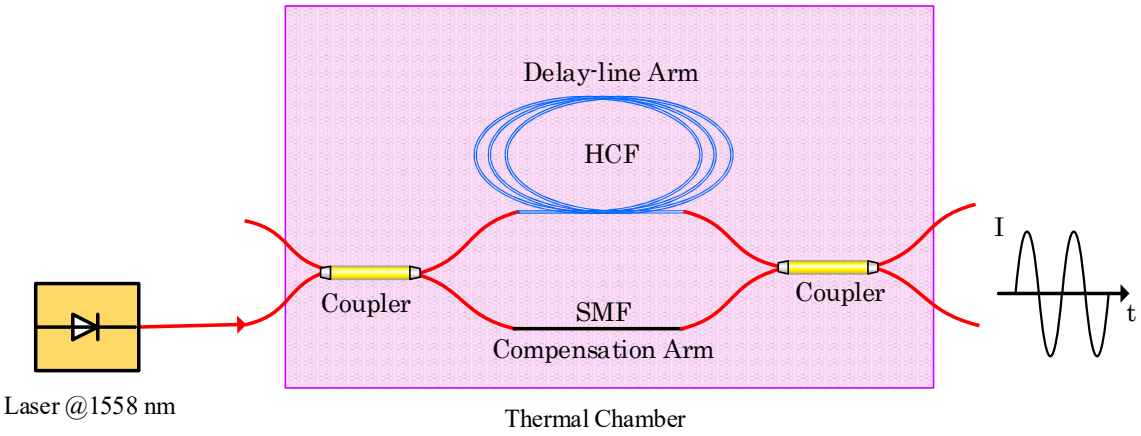

FIGURE 4.12: Scheme of the setup for measuring the thermal sensitivity of compensated interferometer.

For the thermal process of experiment, the temperature is first stabilized at 40 ℃, then decreased to 10 ℃, and stabilized again. FIGURE 4.13 shows the recorded temperature and interference fringes.

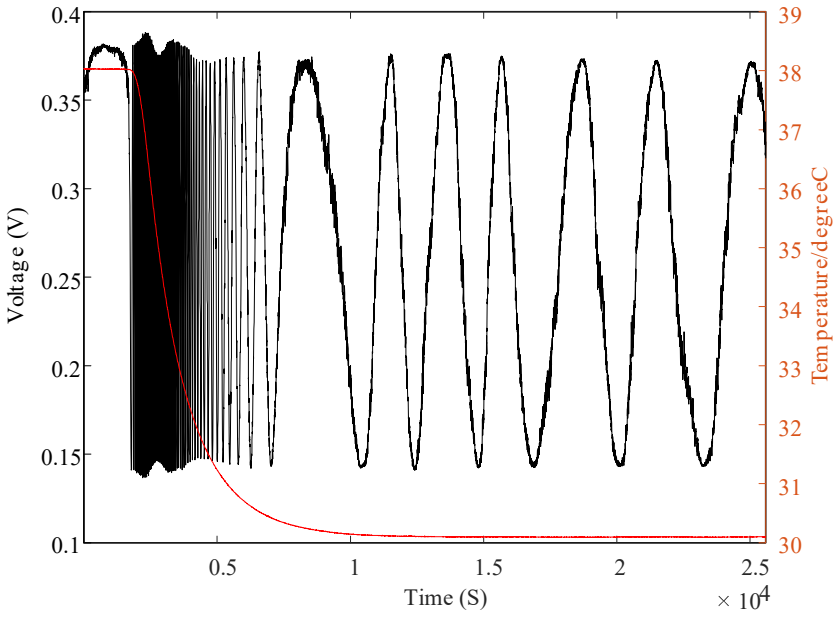

FIGURE 4.13: Recorded temperature change inside the box (red solid) and the output signal of the interference (black solid).

By counting the peaks and recording the temperature, the thermal sensitivity can be calculated from the fitting curve of relationship between phase change and temperature (see FIGURE 4.14). Note here the temperature shown was not the same as what we set on the thermal chamber, which is because the commercial control system has a different algorithm to translate the resistance of thermistor to voltage compared to our reading system, and we used what we read to show the results. Besides, phase data was not shown during stabilization stage at the start and end, this is due to the weak point of the counting method, which can hardly give the phase information when there is no full period of the sinusoidal-shaped data.

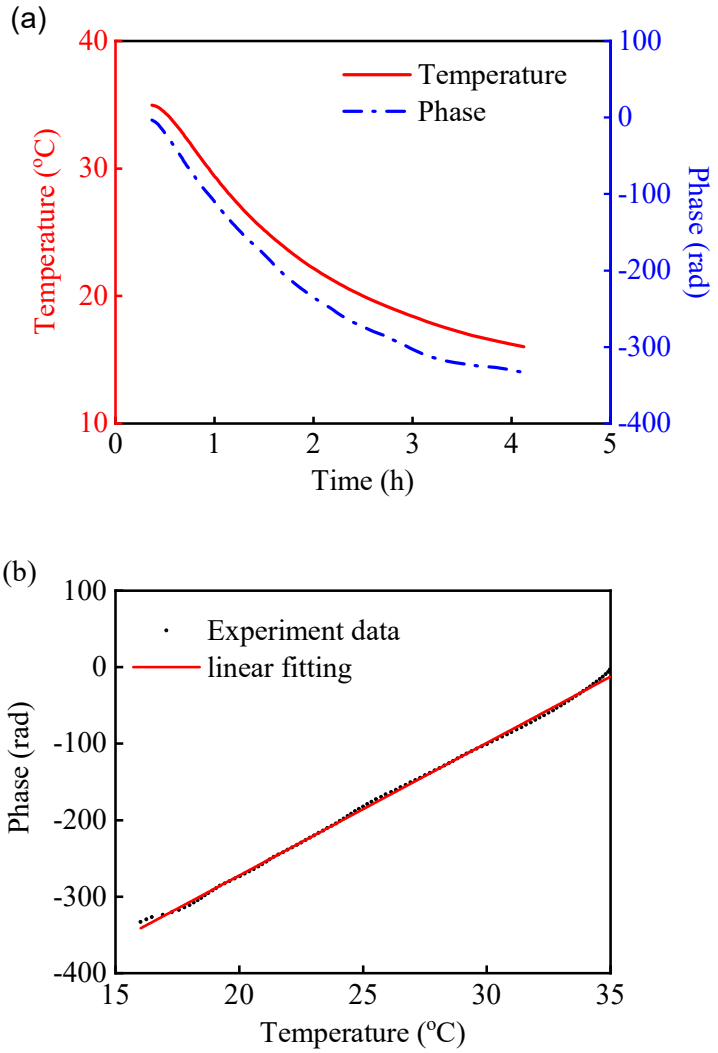

FIGURE 4.14: (a) Temperature inside the thermal chamber and accumulated phase measured for compensated MZI. (b) Relationship between temperature and accumulated phase change of compensated interferometer.

The measured thermal sensitivity of compensated MZI is 1.8 rad/m/K, which is very close to the calculated value of 1.6 rad/m/K (calculated using HCF and SMF previously-discussed thermal

sensitivities of 2.2 rad/K/m and 48 rad/K/m, respectively). To obtain lower thermal sensitivity, we subsequently reduced the SMF arm length to 64 cm and after characterizing thermal sensitivity further to 39 cm. The comparison between theoretical and experimental thermal sensitivities of the three interferometers are shown in TABLE 4.2.

Length of HCF (m)	Length of SMF (m)	Theoretical prediction (rad/K/m)	Experiment results (rad/K/m)
10.78	0.84	1.6	1.8
10.78	0.64	0.6	2.8
10.78	0.39	0.7	3.8

TABLE 4.2: The theoretical and experimental thermal sensitivities of compensated MZI with compensated SMF arm of different length

In TABLE 4.2, only the first experimental result is consistent with the calculation, while the other two are very different, which means the thermal sensitivities of fibres are not what we have expected, either the thermal sensitivity of HCF is much higher than we thought, or the SMF has smaller thermal sensitivity than reported before. Here the SMF used is a standard commercial fibre of which thermal sensitivity has been measure before, but the used HCF is a fibre sample that has not been used in any previous thermal sensitivity characterizations, and thus its thermal sensitivity may be different. Considering the SMF thermal sensitivity is as reported in literature (48 rad/K/m), our experimental results suggest the thermal sensitivity of the used HCF is 5 rad/K/m, which is more than two time higher than the calculated value of 2.0 rad/K/m and significantly higher than the previously-reported measured value of 2.4 rad/K/m.

To confirm this hypothesis, we fabricated the HCF-only interferometer by removing the SMF in our compensated interferometer from the compensation arm. we set the thermal process in two phases to see the thermal sensitivity of the HCF at different temperature range. The temperature was firstly stabilized at 40 °C, and then decreased to 30 °C, and after reaching stable temperature for about 6 hours, it was further decreased and stabilized at 20 °C. The recorded temperature and extracted thermal-induced phase change were shown in FIGURE 4.15.

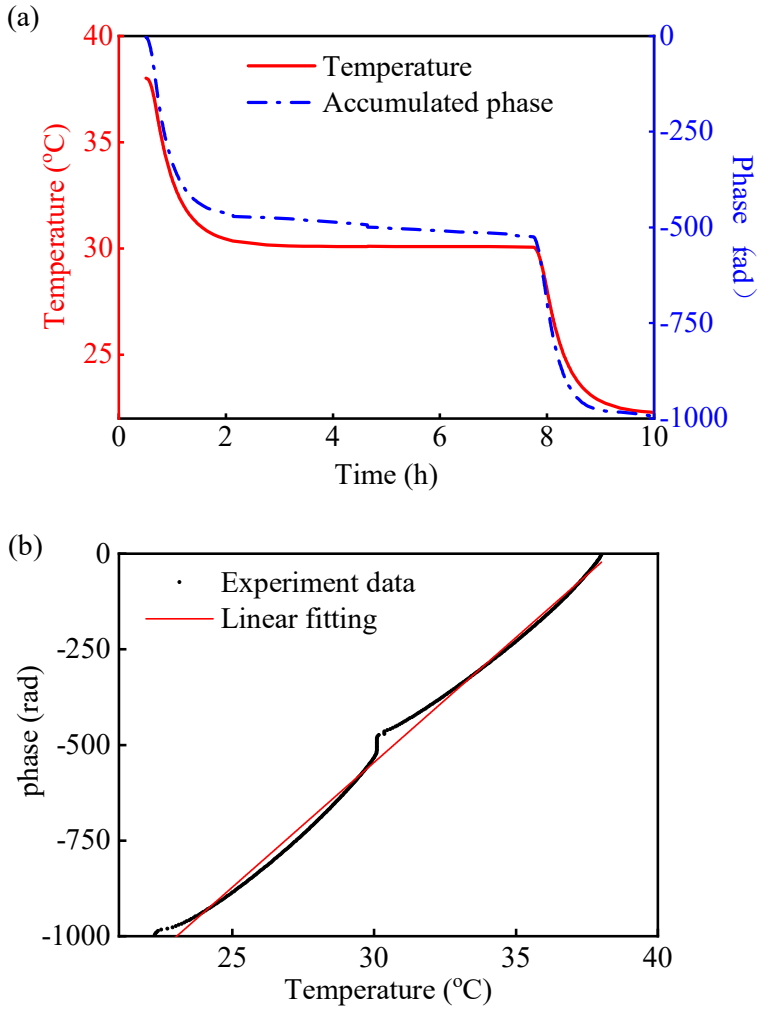

FIGURE 4.15: (a) Temperature inside the metal box and accumulated phase measured for 10.78 m HCF. (b) Relationship between temperature and accumulated phase change of here-used HCF.

Here are two main phenomena shown in the results. One is the thermal sensitivity of this HCF is 5.9 rad/m/K in average (20 ℃~30℃: 5.7 rad/K/m; 30 ℃~0℃: 6.0 rad/K/m), two times as higher as reported HCF, which would explain the difference between the theoretical expected and the experimental thermal sensitivity of the compensated interferometer prototype. It also suggests that 2 times longer SMF in the other arm are needed to compensate the thermal induced phase change of this HCF, and to have the same delay-length of the HCF only interferometer, 11% more HCF is needed, which will increase the expense. Besides, there is a long-term phase drifting of this HCF which is due to the viscoelastic effect from the coating and will be demonstrated in later chapter. In our previous theoretical derivation, the phase of two arms should be change at the same time, otherwise it would be hard to compensate each other.

Chapter 5 The first generation of thermally insensitive compensated fibre delay-line interferometer

In this chapter, we show the first generation of the thermally insensitive fibre delay-line interferometer. we first explore the coating's effect on fibre's thermal sensitivity by comparing two HCF with different coatings by the updated setups. Then we present the fabrication of characterization of the first generation of thermally insensitive interferometer. Finally, we introduce the optimization of the measuring system.

5.1 Coating's effect on HCFs

5.1.1 Updated experiment setup

In Chapter 4, we lost some phase data before the temperature change and after the stabilization, due to shortback of counting peaks method, when there are non-full period fringes or sign changes, we cannot distinguish the phase changes. Here we updated the setups to get better knowledge of the thermal response of the fibres which is shown in FIGURE 5.1.

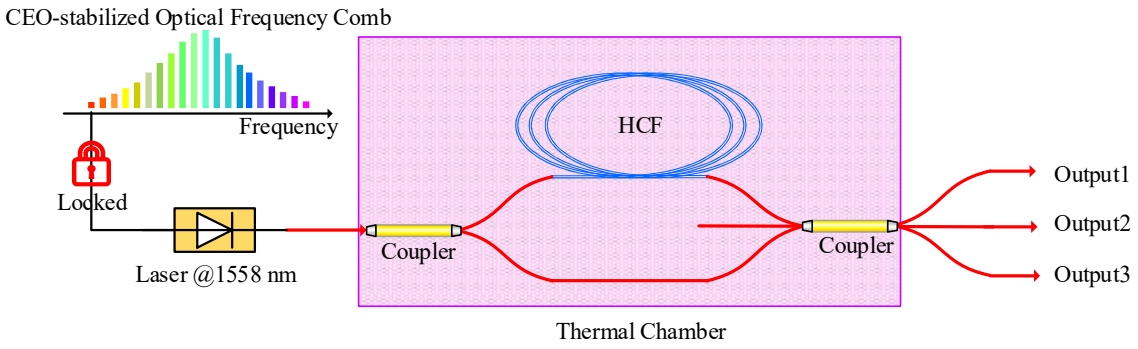

FIGURE 5.1: Measurement set-up used to characterize fibre thermal sensitivity. CEO-stabilized comb: carrier envelope offset stabilized optical frequency comb.

There are some updates compared to previous setup, first one is the laser now is locked on a carrier envelope offset (CEO) stabilized optical frequency comb (Menlo, FC1500-250). we filtered one wavelength from the comb output and beat with the laser we used, and the beat signal was used as error signal to correct the frequency perturbation of our laser. The frequency comb stabilized laser can have frequency with extremely small drift, ensures the phase changes read from the outputs of interferometer is only due to the thermal phase change of the fibre. The other update is a 3×3 coupler replacing the output 2×2 coupler, of which the three outputs are record by three photodetectors. In

FIGURE 4.14, the phase information has been missed because counting peak method cannot extract phase from the none-full period interferometric signals. The employment of 3×3 coupler will allow us to extract the phase with more precise resolution, most importantly, the relative sign change of the phase as well [122], to obtain the absolute sign change of phase, we have to tune the beat frequency between the comb laser and locked laser and see the phase change direction.

Except these, the thermal chamber is the same as previous, and the fibres were coiled with a diameter of 14 cm, the pigtails of couplers are cut short, well balanced in length to avoid the residual phase response from SMF.

5.1.2 Thinly-coated HCF

The HCF used in last chapter has higher thermal sensitivity than previous reported data, as well as the unexpected relatively strong thermal phase drift. In Chapter2, we have introduced a simple model to calculate the thermal phase sensitivity of fibres, however, strictly-speaking it works only for the bare fibres without coatings. The acrylate coatings typically used on optical fibres for protection and to improve their properties have significantly higher coefficients of thermal expansion than fused silica. When a fibre is heated, the coating elongates the fibre beyond what is expected for fused silica, it is relatively small effect, however, we believe it is the reason for the discrepancy. To prove this hypothesis, we tested another two new long HCFs, which have the same inner structure (both are NANF, but different coating shown in FIGURE 5.2).

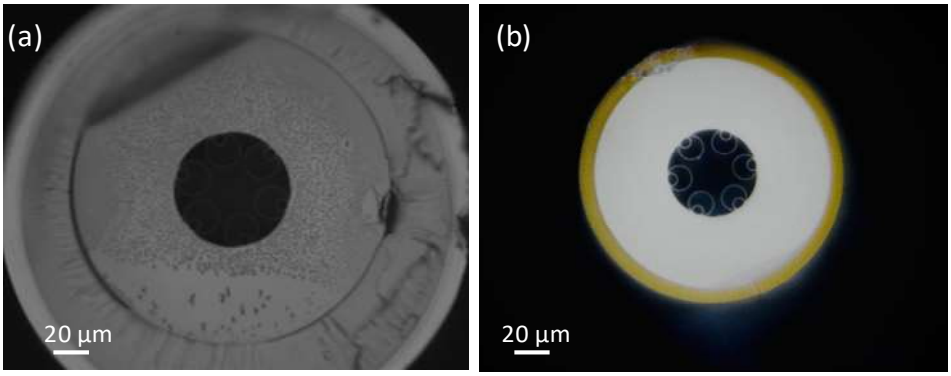

FIGURE 5.2: Microscopy photograph of the previous used HCF (a) and thinly-coated HCF (b).

Unfortunately, we didn't get the HCF with same cladding diameter but different coatings to have a fair comparison, but we believe this effect can be normalised as they are made from the same material, and the geometry parameters are list in TABLE 5. 1

Type of HCF	Thickness of acrylate coating (μm)	Outer diameter of silica glass (μm)	Inner diameter of silica glass (μm)
Dual-coated	45	296	87
Thinly-coated	10	185	70

TABLE 5. 1 Geometric parameters of two HCFs

FIGURE 5.3 shows the measured accumulated phase change in response to temperature change. For the thinly-coated HCF, the phase change follows the temperature change (e.g., when the temperature became stable, the accumulated phase was constant) and the extracted phase sensitivity (calculated from the phase difference at the three temperature points) is shown in FIGURE 5.3 (a). The situation is different for the dual-coated HCF, FIGURE 5.3 (b), where the phase keeps changing even when the temperature is stable. Following a temperature rise (from 20 ℃ to 38 ℃ and then from 38 ℃ to 59 ℃), the measured phase initially rose, but then continued to reduce for several hours. When decreasing the temperature, we observe the same effect but with an opposite sign. (Note here the drift direction is inconsistent with that shown in last chapter which indicates that the phase will keep increasing when temperature is stabilized after decreasing, and this is due to the counter peaks algorithm can't distinguish the sign change of the sinusoidal fringes as we mentioned above). The drift of phase at constant temperature eventually stopped when the temperature was kept constant. In FIGURE 5.3 (b), we see this for example at the temperature of 59 ℃ (time of 12-22 hours) and at 20 ℃ (time of 36-60 hours).

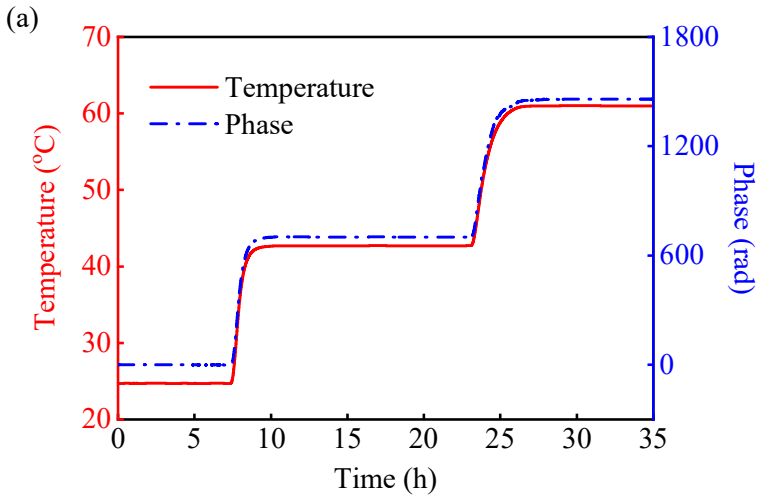

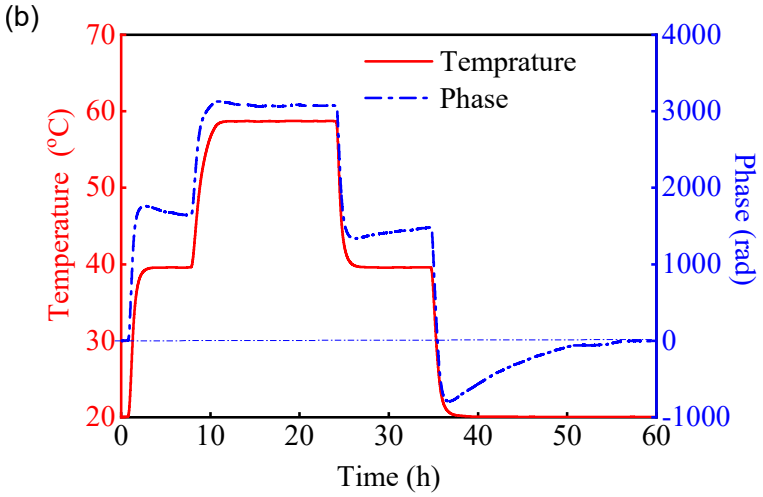

FIGURE 5.3: Temperature inside the thermal chamber and accumulated phase measured: (a) 24-m long thinly-coated HCF; (b) 30-m long dual-coated HCF.

Besides the time-dependent behaviour, the overall thermal sensitivity of the dual-coated HCF is larger than the thinly-coated HCF, as shown in FIGURE 5.4, in which the phase measured at five stable temperature points in FIGURE 5.3 (b) is used for the calculation. The error bars correspond to the difference between the values measured when increasing and decreasing the temperature. The thermal sensitivity of thinly-coated fibre is about 1.6 rad/m/K, which is smaller than the theoretical calculation, and we will explain it later. As for dual-coated HCF, the thermal sensitivity is about 2.8 rad/m/K, not consistent with the results in last chapter, 5.9 rad/m/K. As we used the same fibre, the thermal sensitivity would not be significantly different in two independent measurements. Comparing the phase change of two measurements from temperature 40 to 20 °C, we can see in later one the phase change overshot is about 80% of the stabled phase, and due to the shortcoming of counting peaks method which cannot distinguish the sign of the sinusoidal waveforms, we counted this overshot as the thermal phase change, induced this discrepancy. It indicates that phase demodulation method based on 3×3 coupler is necessary for the later work. For comparison, we also plot in FIGURE 5.4 the thermal sensitivity results measured on our typical single-coated HCF (data adopted from [66]). we see that the thermal sensitivities of the two single-coated HCFs differ by about 20%, with the thinly-coated HCF achieving a lower sensitivity result than expected from the uncoated HCF (2.4 rad/m/K, as discussed earlier).

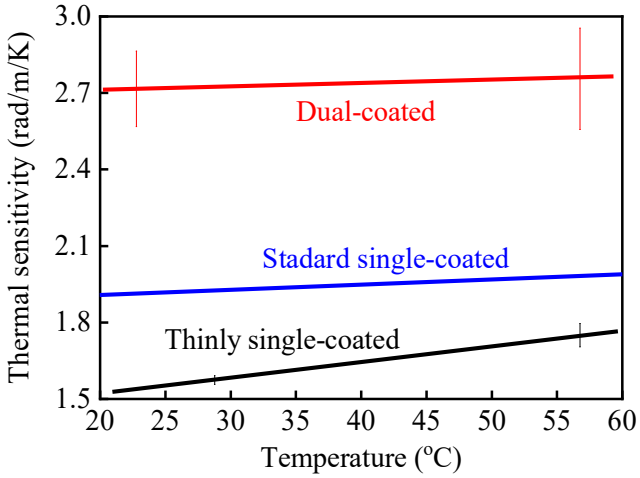

FIGURE 5.4: Phase thermal sensitivity of three measured HCFs (thinly-coated, standard single-coated and dual-coated) calculated from data shown in FIGURE 5.3 (thinly-coated and dual-coated) and from the data in [66] (standard single-coated).

5.1.3 Theoretical analysis and simulations

To explain the results, more specifically, the different thermal sensitivities and phase drifting of fibres made of the same materials, the coatings' contribution is considered using the model proposed by Dangui et al. [62]. FIGURE 5.5 shows the structure of the HCF, note here the micro-structure is neglected.

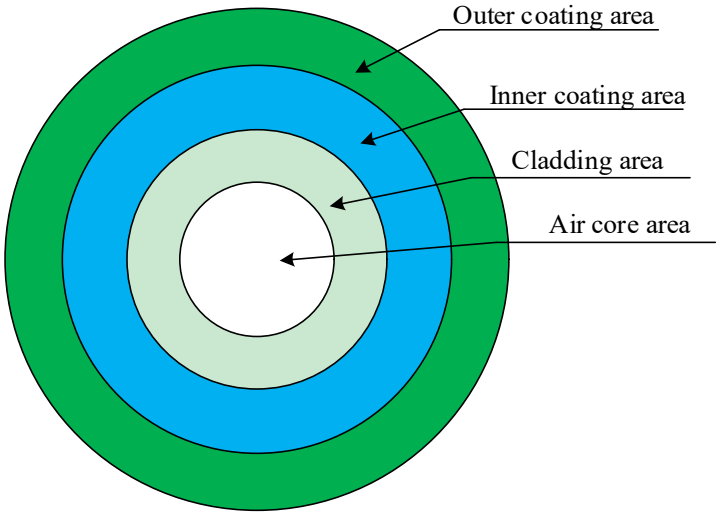

FIGURE 5.5: Schematics of the hollow core fibre structures

The thermal coefficient of expansion of a coated fibre in this model is:

$$\alpha_{coated\ fiber} = \frac{\alpha_{silica}E_{silica}A_{silica} + \sum_{i(}\alpha^{i}{}_{coating}E^{i}{}_{coating}A^{i}{}_{coating})}{E_{silica}A_{silica} + \sum_{i(}E^{i}{}_{coating}A^{i}{}_{coating})} \quad (5.\ 1)$$

where A denotes the cross-sectional area and E the Young's modulus of silica glass and the coating material. For a HCF with single-material coatings, (5. 1) can be written as:

$$\alpha_{coated\ fib} = \frac{\alpha_{silica}E_{silica}A_{silica} + \alpha_{coating}E_{coating}A_{coating}}{E_{silica}A_{silica} + E_{coating}A_{coating}} \quad (5.\ 2)$$

I will consider room temperature (25 °C) and the representative coating parameters given in [62]: $E_{coating} = 35$ MPa, $\alpha_{coating}$= 180 ppm/K, $E_{silica} = 72.5$ GPa and α_{silica}= 0.55 ppm/K. Given $E_{coating} \ll E_{silica}$ and considering $A_{coating} \sim A_{silica}$, we can simplify (5. 2) to:

$$\alpha_{coated_{fib}} \cong \alpha_{silica} + \alpha_{coating}\frac{E_{coating}}{E_{silica}}\frac{A_{coating}}{A_{silica}} \quad (5.\ 3)$$

Considering the above numbers, we get:

$$\alpha_{coated_{fib}} \cong 0.55\,\text{ppm/K} + 0.08\,\text{ppm/K}\frac{A_{coating}}{A_{silica}} \quad (5.\ 4)$$

I see that the larger cross-sectional area that a coating occupies, the more strongly overall fibre expansion may happen. With the parameters in TABLE 5. 1, we get calculated thermal sensitivity of dual-coated and thinly-coated HCF as 2.66 rad/m/K (0.61 ppm/K), 2.48 rad/m/K (0.57 ppm/K). Note here the calculated thermal sensitivity of thinly-coated HCF is significantly different to the measured results, even when neglecting the coating influence in (5. 3) the value is 0.55 ppm/K, which is still significantly higher than the measured results, 0.42 ppm/K. This is not in contradiction with values reported in the literature, where fused silica glass has been demonstrated to have a thermal expansion coefficient at room temperature spanning a relatively large range from 0.38 ppm/K to 0.55 ppm/K. This result is also consistent with our previous measurements [66] shown in, in which we measured a value of 0.47 ppm/K (already below that of 0.55 ppm/K) even for a single-coated HCF with standard coating thickness. we conclude that the silica coefficient of thermal expansion for optical fibres (and in particular HCF) can be as low as 0.38 ppm/K.

In FIGURE 5.3 (b) we show that besides a higher value of thermal phase sensitivity, the HCF coating is also responsible for the phase relaxation effect, where the light phase keeps changing many hours after the temperature has been stabilized. To understand better this effect, we modelled the thermal behaviour of the dual-coated HCF sample in COMSOL Multiphysics. The diameter of the coating and silica cladding of the modelled fibre were set to be the same as the manufactured sample, while the contribution from the inner tubes (microstructure) to the thermal sensitivity was neglected. In COMSOL, two independent physics interfaces (Solid mechanics and Heat transfer in solids) were employed and coupled together to simulate the thermal elongation of an optical fibre,

including both heat transfer and the mechanical properties. we modelled the coating layers as viscoelastic materials, which are characterized (besides the elastic properties) by a relaxation time that describes the relaxation of thermal stress. In the simulations, we considered the temperature observed in the experiment (shown FIGURE 5.3 (b)). we fitted all the parameters from their initial values obtained in the literature and relevant datasheets [123][124], in particular, Young's modulus, thermal expansion coefficients, and relaxation time. compares the measured (shown in FIGURE 5.3 (b)) and fitted phase changes in response to temperature change. we was able to obtain an excellent fit, especially in term of the relaxation caused by the coating viscoelastic properties. It is worth mentioning that we was not able to obtain a good fit with $\alpha_{silica} = 0.55$ ppm/K, especially in terms of the relaxation. However, using $\alpha_{silica} = 0.38$ ppm/K as discussed above allowed us to achieve a good fit, as shown FIGURE 5.6. The fitted time constant of the coating varies between 60 000 s at 25ºC and 6000 s at 60 ºC. we consider this reasonable, as the other coating parameters (Young's modulus in particular) also change significantly with temperature. To avoid this thermal relaxation induced phase shift, we suggest using a thick HCF silica cladding jacket in conjunction with a thin coating. Such a design also reduces the thermal phase sensitivity of the HCF, as we show here experimentally and as was previously demonstrated numerically [66].

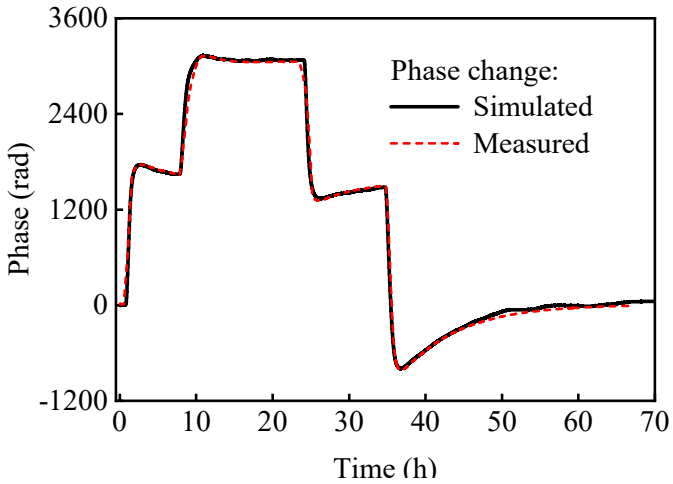

FIGURE 5.6: Comparison of measured (shown in FIGURE 5.3 (b)) and simulated thermal sensitivity of dual-coated HCF considering viscoelastic behaviour of the coating.

5.2 Fabrication of compensated fibre interferometer with different SMFs

After getting better performance HCF (with small thermal sensitivity and less thermal induced phase drifting), we returned to our project and made temperature-compensated interferometer. Here we employed 24 m HCF, for SMF, we first tried the standard one. To compensate the thermal phase change of 24 m HCF, 1 m standard SMF was used to fabricate the

compensated interferometer, of which the thermal sensitivity was measured in the updated setup (See FIGURE 5.7, slightly different FIGURE 5.1 as we spliced a short piece of SMF in non-HCF arm). The laser was locked to the optical comb to ensure the frequency stability, and the HCF and SMF were wound together to experience the same temperature variation Three outputs of 3×3 coupler allowed to extract the phase change of the interferometer.

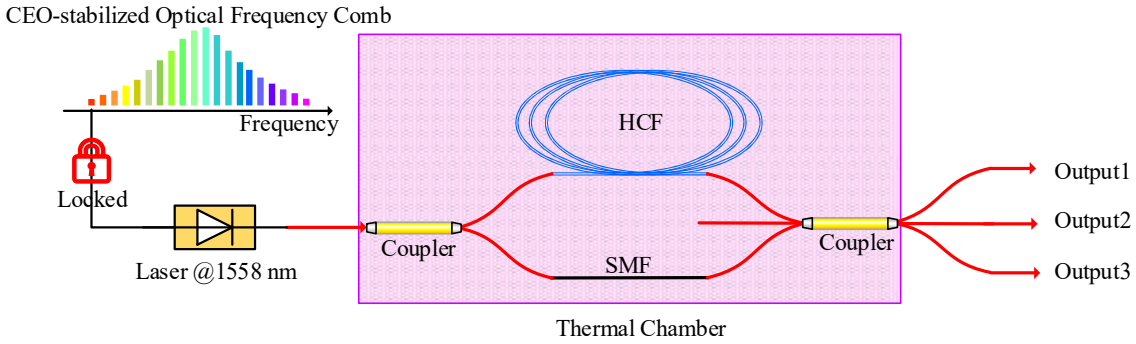

FIGURE 5.7: Measurement set-up to characterize the thermal sensitivity of delay-line interferometers.

For the thermal process, temperature here is firstly stabilized at 25 ℃, and then increased to 45 ℃. After long stabilization time (10 hours), the temperature is increased to 65 ℃, followed by 20 hours of measurement. Temperature and accumulated phase change are shown FIGURE 5.8(a). When temperature was stabilized at 45 ℃, the phase decreased by about 10 rad. As we have not observed this with HCF, this effect is attributed to the SMF and in particular its coating. From 45 ℃ to 65 ℃, the phase first increases, but then decreases until it gets stable. Data in FIGURE 5.8 (a) shows that the sign of the compensated interferometer thermal sensitivity has changed, as the first temperature increase result in the phase increase, but the further temperature increases lead to the phase decrease. As we have measured earlier, the thermal sensitivity of HCF changes little with temperature. Thus, we attribute this behaviour to a change in the SMF thermal sensitivity.

Earlier research confirmed that the thermal sensitivity of SMF can also be influenced by its coating [61]. With temperature increase, thermal sensitivity of dual coated and bare SMF can be very different. Specifically, at temperature of 0 ℃ to 30 ℃, thermal sensitivity of coated SMF decreases, while it increases for bare SMF. This decrease in the coated SMF causes the thermal phase of compensated interferometer to strongly change with temperature, as this trend is the opposite to that of the bare HCF. This makes the compensation working only at a specific temperature with over(under) compensation quickly rising as the temperature is moved from this specific point. Bare SMF would be the best option, but it would be extremely fragile, thus, using a thinly-coated SMF for compensation in our compensated interferometer would be preferred.

A thinly-coated SMF (coating thickness of 10 μm), which should behave very close to uncoated fibre but less fragile, was manufactured in the ORC. we used 1.2 m long (not the optimized compensation length) of this fibre in the compensating arm and change the temperature in steps every 10 ℃ from 25 ℃ to 65 ℃, FIGURE 5.8(b).

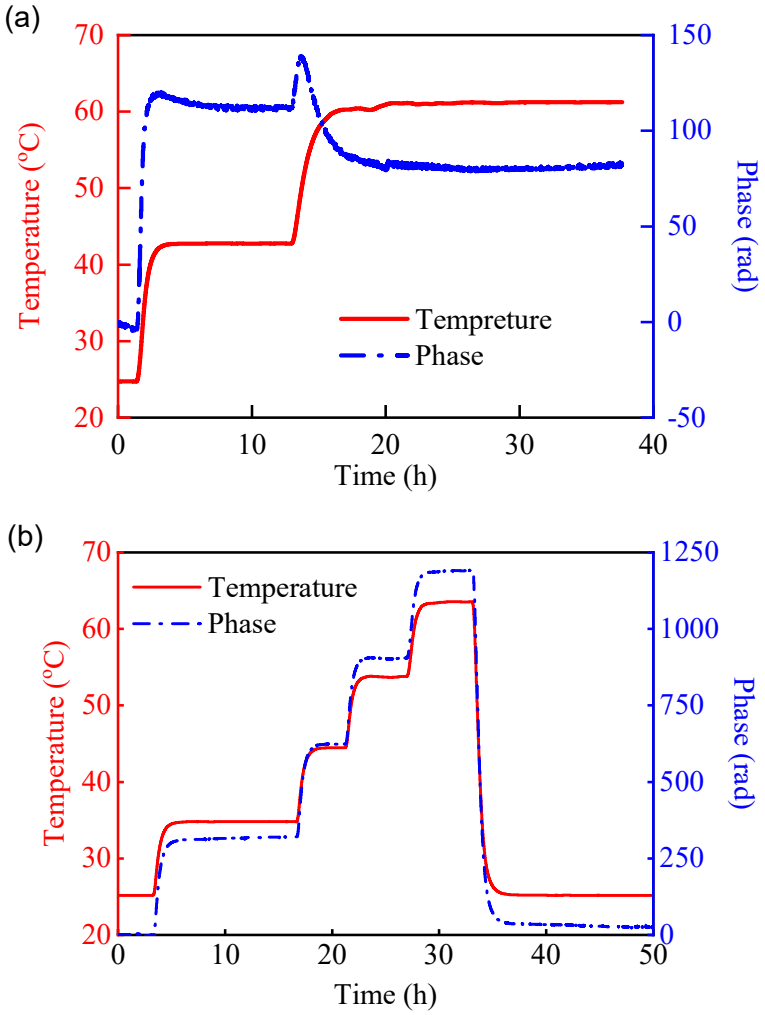

FIGURE 5.8: Accumulated phase change (blue curve) of compensated MZI with coated SMFs with temperature increasing (red curve): (a) Dual-coated SMF; (b) Single thinly-coated SMF.

From FIGURE 5.8 (b), the thermal accumulated phase follows the temperature change well (without any over/undershoots as seen previously), while there is only a small difference between the phase change in different temperature range, which means that the thermal sensitivity of compensated interferometer is slightly temperature dependent. The thermal sensitivity of thinly-single-coated SMF is calculated as 39 rad/K/m in average, which is smaller than that of standard SMF (reported as 48 rad/K/m) and even uncoated SMF (calculated as 40 rad/K/m). The origin may be in the composition of the SMF core, which can alter the thermo-optic coefficient significantly.

As we measured the thermal sensitivity S_φ of 1.57 rad/m/K for the thinly-coated HCF (T-HCF) and 39.3 rad/m/K for thinly-coated standard SMF (T-SSMF) at 28°C in last chapter, when 40 m length of T-HCF is employed to be the delay arm of our compensated fibre delay-line interferometer, based on the compensation principle, a 1.6-m long T-SSMF was thus required to produce the same phase change in response to temperature (length ratio of 1:25). The thermal sensitivity of this interferometer is measured.

5.3 Characterization of compensated fibre interferometer

In (2. 29) we showed the two factors responsible for the thermal sensitivity of fibres, the thermal expansion, and thermo-optics effects of guiding material. For the first part, as HCF and SMF are both made of silica glass, they should have the same temperature dependent relationship, while for the thermo-optics of air is significantly different from the doped solid core. Considering the temperature influence on the thermal sensitivity, when the fibre works in a relative smaller temperature range, the temperature dependent relationship can be approximated to be linear. Then the thermal sensitivity of HCF and SMF can be simplified as:

$$S_{\varphi HCF} = a_{HCF}T + b_{HCF} \tag{5. 5}$$

$$S_{\varphi SMF} = a_{SMF}T + b_{SMF} \tag{5. 6}$$

Appling.(4. 2), we have the phase change:

$$\Delta\varphi = \int_o^{L_1} dL \int_{T_1}^{T_2} (a_{HCF}T + b_{HCF})dT - \int_o^{L_2} dL \int_{T_1}^{T_2} (a_{SMF}T + b_{SMF})dT \tag{5. 7}$$

As the fibres are wound together, the temperature along the fibre is still believed to be the same, thus we would have.

$$\Delta\varphi(T) = L_1\left(\frac{1}{2}a_{HCF}T^2 + b_{HCF}T + c_{HCF}\right) - L_2\left(\frac{1}{2}a_{SMF}T^2 + b_{SMF}T + c_{SMF}\right) \tag{5. 8}$$

$$= \frac{1}{2}(a_{HCF}L_1 - a_{SMF}L_2)T^2 + (b_{HCF}L_1 - b_{SMF}L_2)T + c_{HCF}L_1 - c_{SMF}L_2$$

It shows that the phase change is a quadratic function of temperature as seen in Fig. 3, and it also indicates the zero thermal sensitivity temperature can be tuned by changing the length ratio slightly which will be discussed later.

5.3.1 Thermal sensitivities of delay-line interferometers

The result of thermal sensitivity measurement of the compensated delay-line fibre interferometer is shown in FIGURE 5.9. The accumulated phase firstly decreased, reaching a turning point at around 28°C, then increased. we did not show the whole temperature range but emphasized the phase thermal sensitivity crossing zero which is an important indicator for stabilizing the interferometer with as low thermal perturbation as possible. Our principle in Chapter 4 is a reasonable approximation, to explain this polynomial liked shape function in a large range of temperature variation, the temperature dependent thermal sensitivity of fibre needs to be considered which has already been shown in FIGURE 5.4.

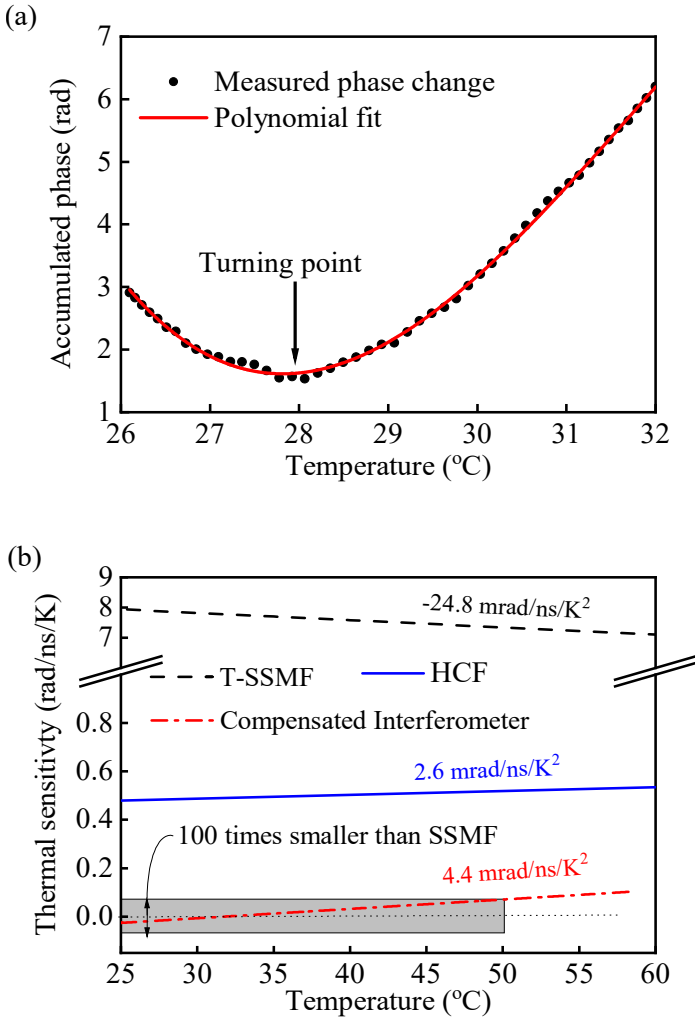

FIGURE 5.9: (a) Dynamically measured phase change of the compensated delay-line interferometer from 26°C to 32°C (black scatter points), and the 3rd order polynomial fit (red line). (b) Measured thermal sensitivity of T-SSMF (black, dashed), T-HCF (blue, solid), and the compensated delay-line (dash-dot, red) interferometers, measured from 25 to 60°C. The shown numbers refer to the slopes of the corresponding curves.

Due to it guiding light through air, the optical delay length of HCF is the same as its physical length differs from SMF. To have a fair comparison between delay-line interferometers made of standard single mode fibre (SSMF), HCF and our compensated delay-line interferometer, we normalize the interferometer thermal phase sensitivity to unit delay:

$$P_\varphi = \frac{1}{\tau}\frac{d\varphi}{dT} \tag{5. 9}$$

where τ is the delay introduced by the delay-line interferometer and φ is the phase difference of the two arms. The delay-normalized thermal sensitivities P_φ of our compensated delay-line interferometer together with those of T-SSMF and T-HCF measured with the dynamic method are plotted in FIGURE 5.10. Here we see that P_φ of T-HCF (~0.5 rad/ns/K) is about 16 times smaller than that of T-SSMF (~8 rad/ns/K). It is worth mentioning that the T-SSMF sensitivity is slightly smaller than that of SSMF reported to have S_φ = 48 rad/m/K, which is a value corresponding to P_φ = 9.6 rad/ns/K. For the compensated delay-line interferometer, P_φ measured over the temperature range of 25-55 °C is almost 7 times smaller than that of T-HCF and over 100 times lower than that of T-SSMF. Additionally, it crosses zero (detail shown in FIGURE 5.9) at 28°C, where the interferometer is essentially thermally insensitive.

To verify the obtained results, we carried out the static measurement for the compensated interferometer over four temperature ranges (25-27°C, 27-29°C, 29-31°C, and 31-33°C), FIGURE 5.10. Both dynamic and static measurements agree well and show that the thermal phase sensitivity of the compensated delay-line interferometer crossed zero at 28°C. In the temperature range of 27-29°C in which the interferometer can be kept using, e.g., a simple closed-loop temperature control of ±1 K, the interferometer achieves $|P_\varphi| < 4.8$ mrad/ns/K, which is over 2000 times lower than that of SSMF-based interferometer.

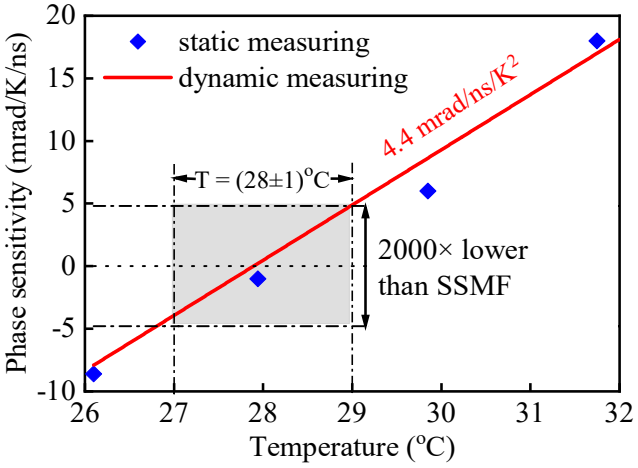

FIGURE 5.10: The dynamically measured (red line) and statically measured (black scatter points) thermal phase sensitivity of the compensated delay-line interferometer. Both show the zero thermal phase sensitivity crossing at a temperature of 28°C.

5.3.2 Tuning of the zero thermal sensitivity crossing temperature

Zero thermal interferometer sensitivity was achieved at a particular temperature (28°C in our experiment) as both, this zero-sensitivity temperature should be shiftable by changing the length of the fibres. It is more practical to change the T-SSMF fibre length, as it has a large thermal sensitivity coefficient and thus only small changes in its length produce an appreciable shift in the interferometer zero thermal phase sensitivity temperature without changing significantly the delay produced in the compensated delay-line interferometer. FIGURE 5.11 shows experimental data obtained when changing the T-SSMF length. we see that a change in the T-SSMF length of 20 cm shifted the zero-sensitivity point from 27 to 47 °C. Thus, setting the zero sensitivity with ±1 °C accuracy requires control of the T-SSMF length of ±1 cm, which is easy-to-achieve with a standard fibre cleaver and splicer. Further modification of the length imbalance beyond what we show here should enable us to lower the zero sensitivity point down to -71 °C (for zero length T-SSMF) [64] or to increase it beyond 47 °C.

In practice, it is desirable to achieve a very low interferometer thermal sensitivity over as large a temperature range as possible. This requires the interferometer thermal phase sensitivity slope to be as small as possible. This slope can be calculated using simple algebra from thermal sensitivity coefficient slopes a of T-HCF and T-SSMF defined as:

$$S_{\varphi}(T) = a(T - T_{room}) + S_{\varphi_{room}} \tag{5. 10}$$

where T_{room} is room temperature, and S_{φ_room} is the thermal sensitivity coefficient at room temperature. Data shown in FIGURE 5.10 lead to a_{T-SSM} = -0.12 rad/m/K^2 (corresponding to -24.8

mrad/ns/K^2) and $a_{HCF} = 8.5$ mrad/m/K^2 (2.6 mrad/ns/K^2), respectively, from which we calculated the slope of the compensated interferometer thermal sensitivity of 4.4 mrad/ns/K^2. This value agrees with the slope obtained by linear fitting of the compensated delay-line interferometer thermal sensitivity. The obtained thermal sensitivity coefficient slopes of T-SSMF and T-HCF also allow us to calculate the extra length of T-SSMF that should be added to increase the zero thermal phase sensitivity temperature of the compensated delay-line interferometer by $\Delta T = T - T_{room}$:

$$\Delta L_{SSMF} = \frac{a_{HCF}\Delta T + S_{\varphi_{room}HCF}}{a_{T-SSMF}\Delta T + S_{\varphi_{room}T-SSMF}} \times L_{HCF} \qquad (5.\ 11)$$

We plot this dependence in FIGURE 5.11 (red solid). Compared to the measured data (FIGURE 5.11, black scatter points), it gives a slightly larger slope, which we believe is due to the too large temperature range considered (from 28 to 46°C), over which the thermal sensitivity coefficients of T-SMF and T-HCF are no longer linear.

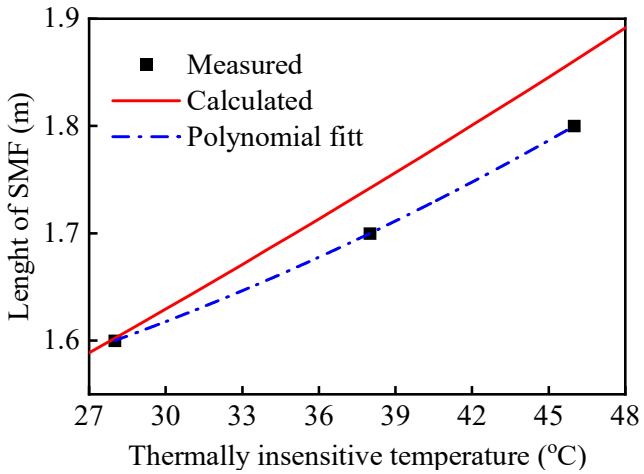

FIGURE 5.11: The measured (black scatter), fitted (2nd order polynomial fit, blue dash-dot) and calculated (red solid,) relationship between the T-SSMF length and compensated delay-line interferometer zero thermal sensitivity temperature when the HCF arm is kept 40 m.

To obtain a smaller thermal sensitivity slope (than that obtained in FIGURE 5.10) and thus lower thermal sensitivity over a larger temperature range, a_{T-SSMF} and a_{HCF} would need to be better "matched", e.g., to have the same sign. we believe this can be achieved, e.g., by a careful selection of the dopants in the T-SSMF fibre core or a different choice of coating material (e.g., metallic or polyimide).

5.3.3 Wavelength dependence

All our experiments were performed with laser source emitting at 1558 nm. Here, we predict how the compensated delay-line interferometer thermal sensitivity changes with the operation

wavelength. The wavelength-dependent thermal sensitivity coefficient of an optical fibre can be written as:

$$S_{\varphi}(\lambda) = \frac{2\pi}{\lambda}\left(\frac{dn_{eff}}{dT}(\lambda) + \frac{n_{eff}(\lambda)}{L}\frac{dL}{dT}\right) \quad (5.\ 12)$$

The first term of the right-hand side is the wavelength dependent thermo-optic effect, and the second term is related to the fibre chromatic dispersion and thermally induced expansion. The thermo-optic effect in a sealed HCF is very weak [120]and for SSMF, it can be described by expansion：

$$\frac{dn}{dT}(\lambda) = c_0 + c_1\lambda^{-2} + c_2\lambda^{-4} + c_3\lambda^{-6} \quad (5.\ 13)$$

With $C_{0,1,2,3}$ = 9.39059; 0.235290; -1.31856×10^{-3} and 3.028887×10^{-4}. The calculated $S_{\varphi}(\lambda)$ of SSMF and HCF considering this dependence, $n_{eff}(\lambda)$ of both fibres calculated in COMSOL Multiphysics, and $\frac{dL}{dT}$ = 0.3 ppm/K is shown. Using these data, the wavelength dependent thermal sensitivity of the compensated delay-line interferometer is calculated and shown in FIGURE 5.12.

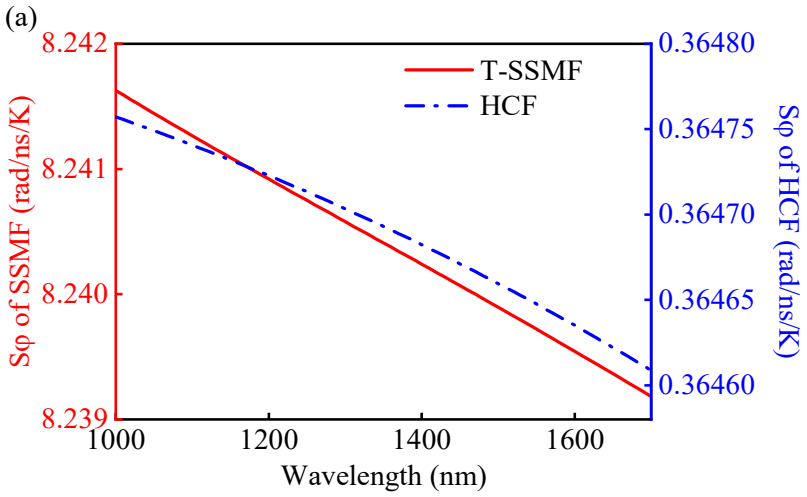

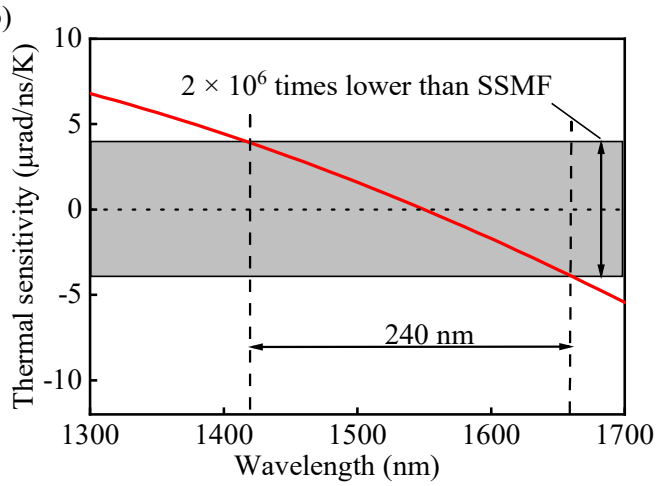

FIGURE 5.12: (a) Calculated wavelength-dependent thermal sensitivity coefficient of T-SSMF and T-HCF; (b) Calculated thermal sensitivity of the compensated delay-line interferometer as a function of wavelength with zero thermal sensitivity set to 1550 nm.

The thermal sensitivity is within ± 4.8 μrad/ns/K between 1420 and 1660 nm (240 nm span), which is over 2×10^6 times smaller than that of the SSMF based interferometer. Unfortunately, we could not confirm this experimentally, as we did not have a tuneable laser that could be locked to the optical frequency comb.

5.4 Optimizations of the measuring system

To further optimize the measuring system, we did two updates. One is to reduce the polarization perturbation due to the polarization extinction ratio is not high enough between connection of fibre links from laser to the interferometer, the other one is to improve the pressure stability of the system by sealing the box where interferometer is enclosure.

5.4.1 Polarization noise reduction

When there is an environmental variation, e.g., temperature change or vibration, on the transport fibre link from the laser to the interferometer, the polarization direction of light propagate inside the fibre will be rotated. As the HCF and SMF we used here are not polarization maintaining, the light in the two axes (fast and slow axis) will couple with each other along the fibres, the interference of the light output from SMF and HCF will cause extra noise of the interferometer. To avoid this polarization degrading, a fibre-based polarizer (fast-axis blocked) is placed between the laser and interferometer, which allows only light propagates in slow axis. Electric field of light after the polarizer can be expressed as:

$$E(t) = E_0(t)\,cos(2\pi ft + \varphi)\,. \tag{5. 14}$$

$E_0(t)$ is the field change due to the polarization change before the polarizer, f is the frequency of light source, and φ is the phase. By photodetector we can have the amplitude:

$$A(t) = A_0(t). \tag{5. 15}$$

It transfers the polarization perturbation to amplitude perturbation of the light source,

For the interference signal, it is:

$$\mathrm{I(t)} = \mathrm{A_0}(t)\left(\mathrm{a_1} + \mathrm{a_2} + \sqrt{\mathrm{a_1 a_2}}\cos(\Delta\varphi)\right). \tag{5. 16}$$

$\mathrm{a_1}$, $\mathrm{a_2}$ is the power ratio of two arms compared to the monitoring, which are depended on the split ratio of coupler and the loss of fibres. By monitoring the light power $\mathrm{A_0}(t)$ after the polarizer, we can easily remove this amplitude perturbation by data processing.

The updated setup was shown in FIGURE 5.13. Laser stabilized to comb propagated first through the fast-axis block polarizer making the light only slow-axis polarization which transfers the polarization perturbation into amplitude perturbation. Then the light was split by a 1:99 PM coupler, 1% port was employed as the power monitoring, and the 99% is coupled into the interferometer. The rest part is the same as previous chapters.

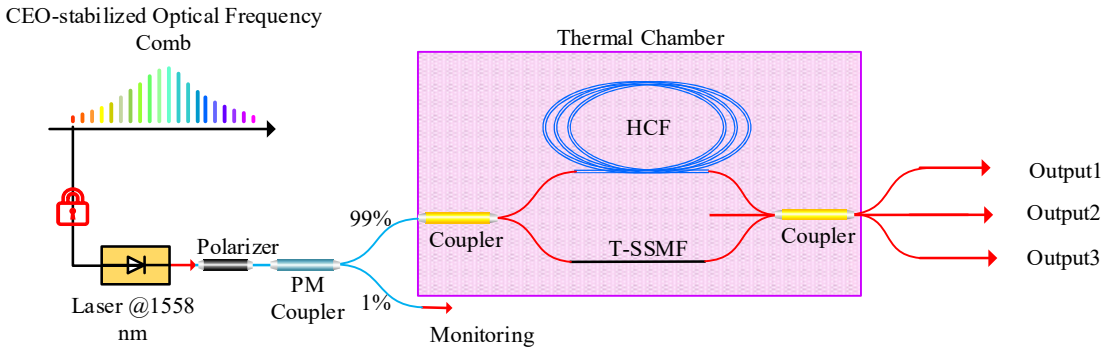

FIGURE 5.13: Updated setup for polarization noise reduction. Polarizer here makes the light propagated only slow-axis polarization and transfers the polarization perturbation to amplitude noise, which can be reduced by dividing the monitoring power.

FIGURE 5.14 shows the raw data of the output (black dash dot), by dividing the monitoring power, the noise is reduced (red solid).

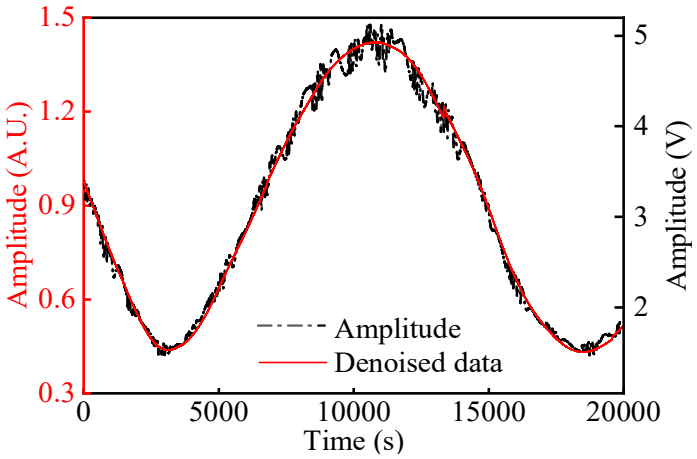

FIGURE 5.14: The raw data of output signal (black dash-dot) and processed data with noise reduced (red solid).

5.4.2 Pressure perturbation reduction

After the denoise of the polarization and amplitude, we stabilized the temperature on zero-sensitivity point. Theoretically, there should not be any thermal induced phase perturbation, but coating relaxation caused drifting. However, when removing the drifting, the phase keeps being perturbated, showing there are still some thermal irrelevant phase changes, shown in FIGURE 5.15

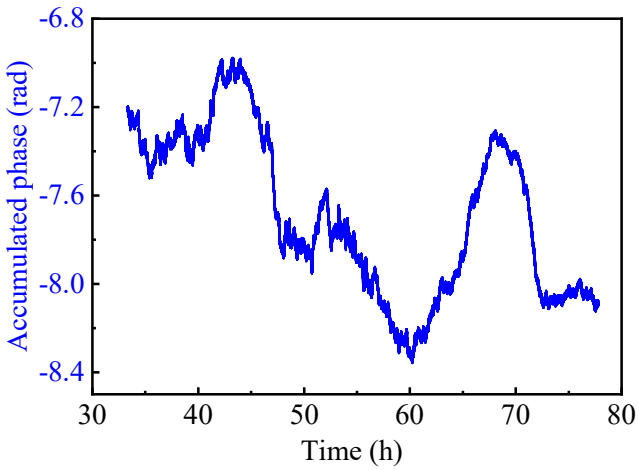

FIGURE 5.15: The phase perturbation after stabilizing the temperature.

Considering the pressure sensitivity of HCF and SMF, which is about 1.5×10^{-5} ppm/Pa (HCF), and 1.15×10^{-5} ppm/Pa (SMF). The pressure change of atmospheric pressure is about ±20 mbar, and this will cause a pressure induced phase change of our delay-line interferometer, 6.6×10^{-5} rad/m/Pa, for a length ration as 21.5:1 (HCF: SMF). Here we added a barometer inside the box and studied the relationship between phase and pressure perturbation is shown in FIGURE 5.16. The

accumulated phase perturbation has a nearly linear relationship with the atmospheric pressure change. Notice there is a drop at 101 mbar, it can be the influence of the moisture.

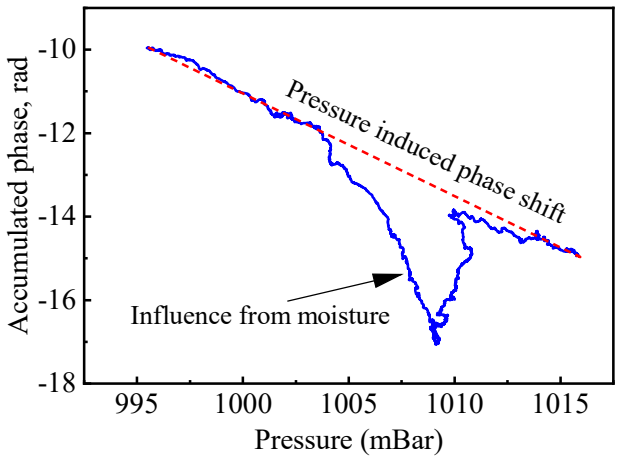

FIGURE 5.16: The relationship between atmospheric pressure and accumulated phase change of the interferometer (box is unsealed).

To get rid of this atmospheric pressure induced phase perturbation, the metal box was seal with silicone glue. After sealing, the pressure variation inside the box is about ±1 mbar, 20 times better than unsealed one (see from FIGURE 5.17)

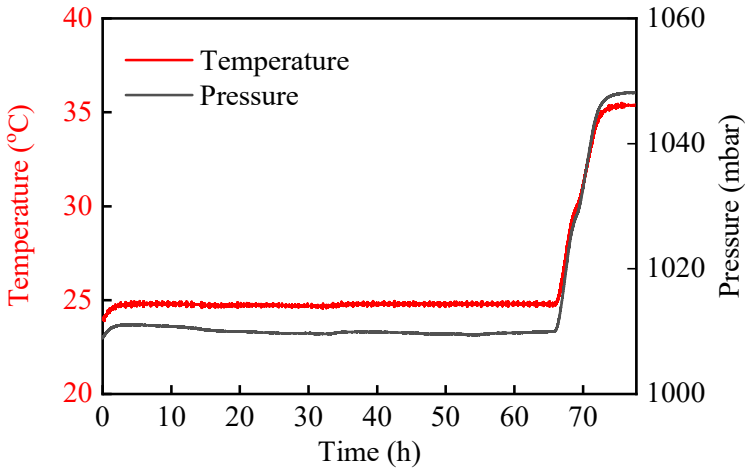

FIGURE 5.17: The temperature and pressure inside the metal box after being sealed by silicon.

Note here the pressure in sealed box is a function of temperature, using the ideal gas function to describe the relationship of physical parameters inside the sealed box:

$$PV = nkT \tag{5. 17}$$

P is the pressure, V is the volume, n is the number of molecules, k is the Boltzmann constant, and T is the temperature. For a box sealed in room temperature, which means no gas molecules leaking (n is a constant), when neglect its expansion (V is constant), define the $N = \frac{nk}{V}$, the initial pressure inside would be atmospheric temperature:

$$P_0 = \frac{nkT_0}{V} = NT_0 \tag{5. 18}$$

$$N = \frac{P_{Atm}}{T_{Room}} = \frac{1.01 \times 10^5}{-248} = \frac{410Pa}{K} \tag{5. 19}$$

Thus:

$$P = 410T \tag{5. 20}$$

Normalizing the thermal induced pressure sensitivity of fibre in sealed box to temperature, it is 6.2×10^{-3} ppm/K for HCF and 4.7×10^{-3} ppm/K for SMF. Note here the thermally insensitive length ration of HCF and SMF would be changed a little bit, in other word, for a well-compensated fibre interferometer, which is thermally insensitive at temperature at $T_0 > T_{room}$, when it is sealed in a box, the zero-sensitivity temperature will be increase to $T_0' > T_0$, due to the thermal induced pressure sensitivity.

Here we plotted the phase change with temperature stabilized over a long time in an unsealed/sealed box in FIGURE 5.18 and FIGURE 5.19. The phase of interferometer in unsealed box perturbates over 60 h, which is due to atmospheric pressure change, while the interferometer in sealed box outputs the phase with certain slope, which is believed to be the drift caused by coating's relaxation. Therefore, it is necessary sealing the box to have a long-term stabilized interferometer.

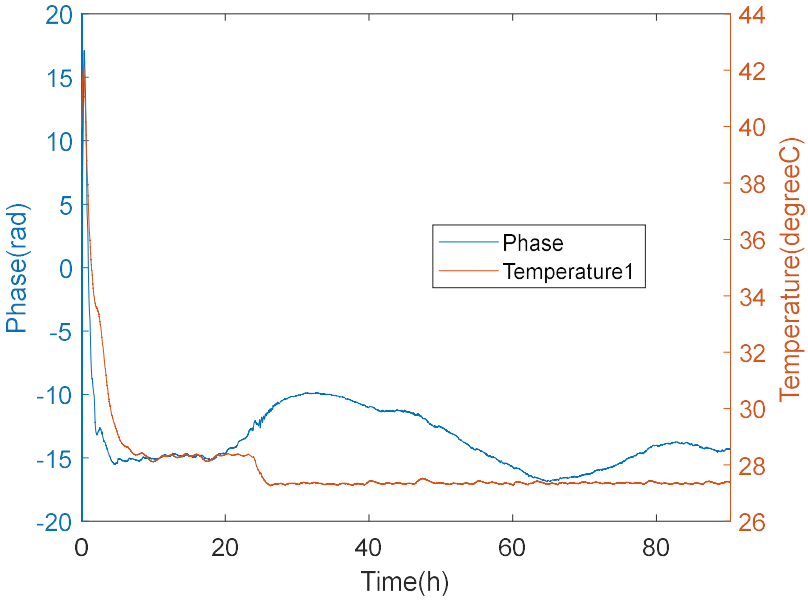

FIGURE 5.18: The relationship between phase and temperature before sealing the box.

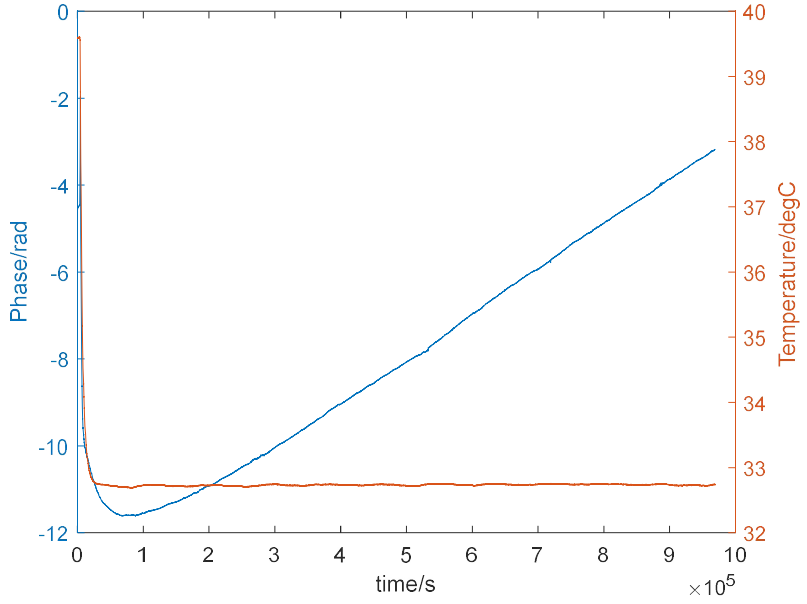

FIGURE 5.19 The relationship between phase and temperature after sealing the box.

Chapter 6 Iteration and characterization of the thermally insensitive compensated fibre delay-line interferometer

In this chapter, we introduce two iterated thermally insensitive fibre interferometer. we first present the new HCF with better mechanical strength. Then we show the second generation of thermally insensitive interferometer and characterize the long-term stability. Finally, we introduce the third generation of fibre delay-line Michelson interferometer.

6.1 New thinly-coated HCF

After sealing the box, the fibre suffered higher pressure when temperature increased, the thinly-coated fibre broke several times, as the coating and silica glass are relatively thin compared to common fibres. To get both mechanical robust and thermal stable fibre, we designed and fabricated a new HCF which has thicker silica cladding and thin coating.

6.1.1 Geometric parameters

The structure of new HCF is shown in FIGURE 6.1. Compared with previous thinly-coated HCF, this fibre has glass cladding as thick as 230 μm, and 30 μm coating. Apart from the geometric parameters, it has only five inner tubes while previous one has six, this design is for depressing the high order mode [104].

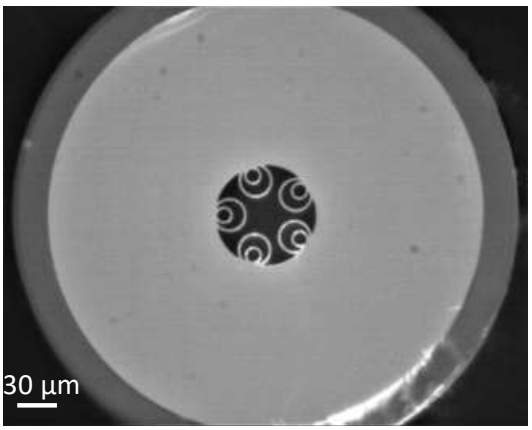

FIGURE 6.1: Microscopy photograph of the cross-section of new thinly-coated hollow core fibre.

6.1.2 Thermal sensitivity of new thinly-coated HCF

Theoretical thermal sensitivity is measured by the same setup in FIGURE 5.1, 1.64 rad/m/K, which is consistent with theoretical calculation. For the measurement, we first stabilized the temperature at 26^{O}C, then increased it to 40^{O}C, and kept it at this temperature for several hours. we recorded the temperature inside the chamber, and power at the three output photodiodes, which we used to retrieve the phase changes, FIGURE 6.2 (a). Subsequently, we processed these data into a phase-temperature plot, which is shown in FIGURE 6.2 (b).

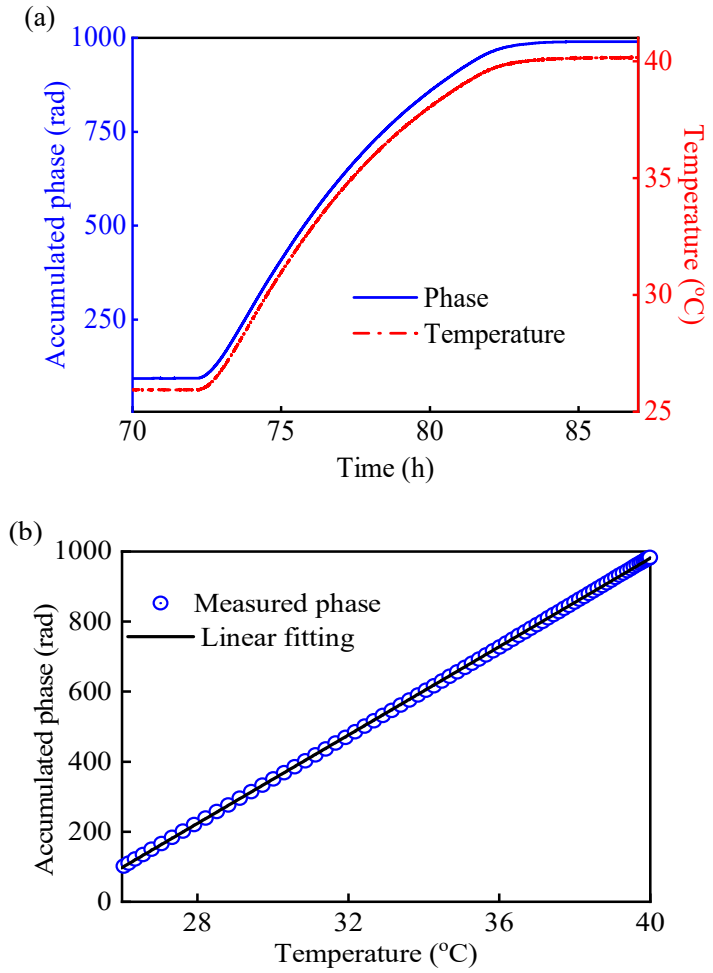

FIGURE 6.2: Phase change of here-reported HCF in response to change in the temperature. (a) recorded over time and (b) extracted phase-temperature plot showing linear dependence with its slope corresponding to thermal sensitivity.

From FIGURE 6.2(b), we see that the thermal response of HCF shows a linear relationship between accumulated phase change and temperature, which can be well fitted with a linear curve, which is also shown in FIGURE 6.2(b). Analysing FIGURE 6.2(a) and (b) suggests that the viscoellastic coating influence is strongly suppressed. For example, it would have introduced a phase drift at the end of the experiment, where the temperature is constant (FIGURE 6.2(a)), as the

viscoelastic coating would keep relaxing. This would have also resulted in a change in the slope of the curve shown FIGURE 6.2(b) towards the end of the experiment. The linear fitting of FIGURE 6.2(b) gives HCF thermal sensitivity of 1.64 rad/K/m, which is in line with our expectations.

6.2 Second generation of compensated fibre interferometer

With the new thinly-coated HCF, second generation compensated fibre interferometer was fabricated. Here HCF is 40 m and of which thermal phase change is compensated by a 2.55-m thinly-coated SMF. By adjusting the length of SMF, the zero-sensitivity temperature is tuned to 28 °C, which is close to the room temperature and easy to be stabilized. After sealing the box, the thermally insensitive temperature was moved to 30.8 °C, as shown in FIGURE 6.3.

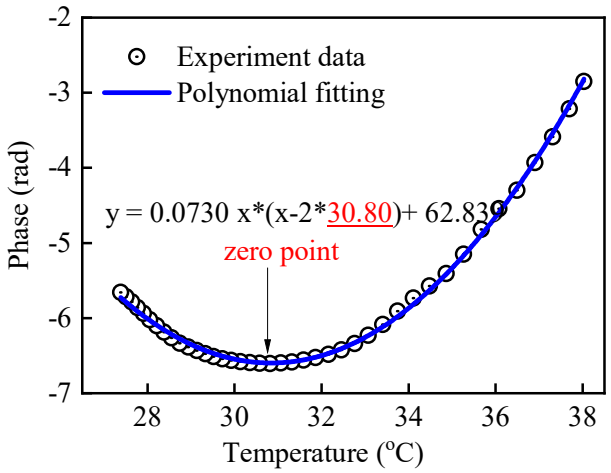

FIGURE 6.3: Relationship between thermal induced phase change and temperature. The extracted phase (black circles) is fitted with polynomial function (blue solid), and the zero-sensitivity temperature is 30.8 °C.

To characterize the second generation thermally insensitive compensated fibre interferometer, the thermal stability under temperature perturbation environment has been tested, and long-term phase stability has been characterized when temperature is stabilized at the zero point.

6.2.1 Thermal stability in temperature variation system

To evaluate the thermal stability of the compensated fibre interferometer under thermal environment with strong perturbation, new thermal process of the thermal system is designed. By gradually reducing the central temperature from 34.5°C to 29.5°C in increments of 1°C and configuring each step's temperature as a sinusoidal function of time, with a period of approximately 10 hours and an amplitude of 1°C, we observed the phase variations of the compensated interferometer within this ±0.5°C temperature perturbation environment, as illustrated in FIGURE

6.4. The phase curve exhibits a sinusoidal pattern that mirrors the temperature variations over time. As the central temperature decreases from 34.5°C to 32.5°C, the amplitude of the phase curve diminishes from 1 rad to 0.5 rad. Conversely, as the temperature further decreases from 32.5°C to 29.5°C, the amplitude increases from 0.5 rad to 1 rad. Additionally, at higher temperatures, the phase change exhibits an opposite sign compared to the temperature change, while at lower temperatures, it aligns with the temperature variations.

Notably, the compensated fibre interferometer demonstrates superior thermal stability, with its lowest thermal sensitivity measured at 32.5 °C, reaching approximately 12.5 mrad/m/K. This sensitivity is about 3200 times better than that of an SMF-based fibre interferometer, which exhibits a thermal sensitivity of around 40 rad/m/K. These results agree well with the measured thermal sensitivity, further highlighting the exceptional thermal stability achieved by the compensated fibre interferometer.

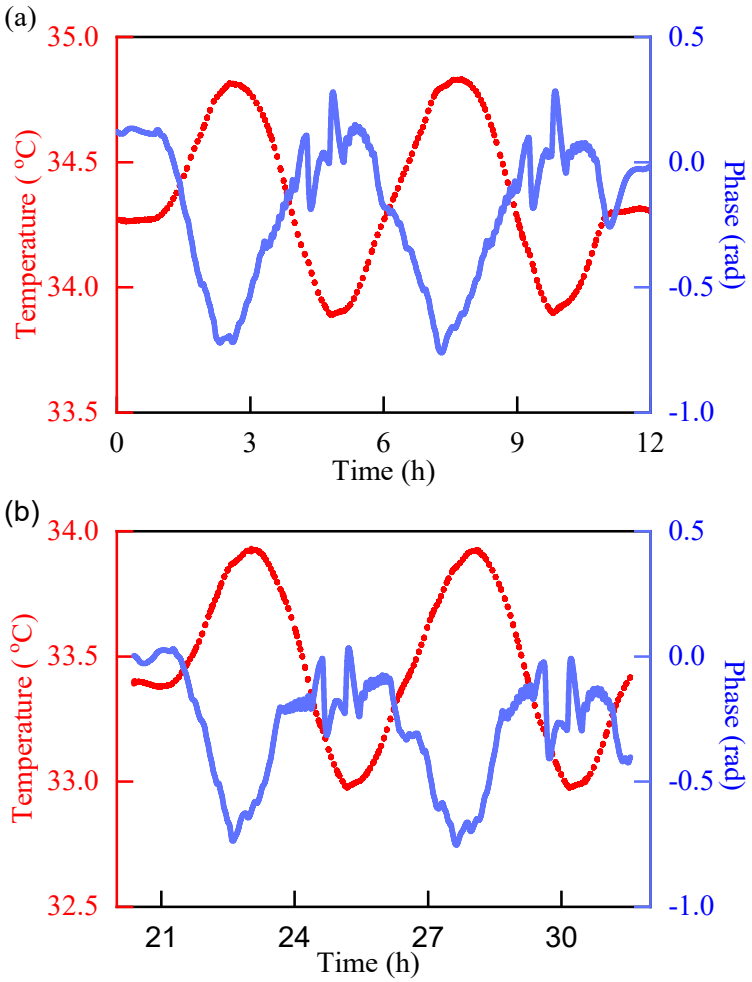

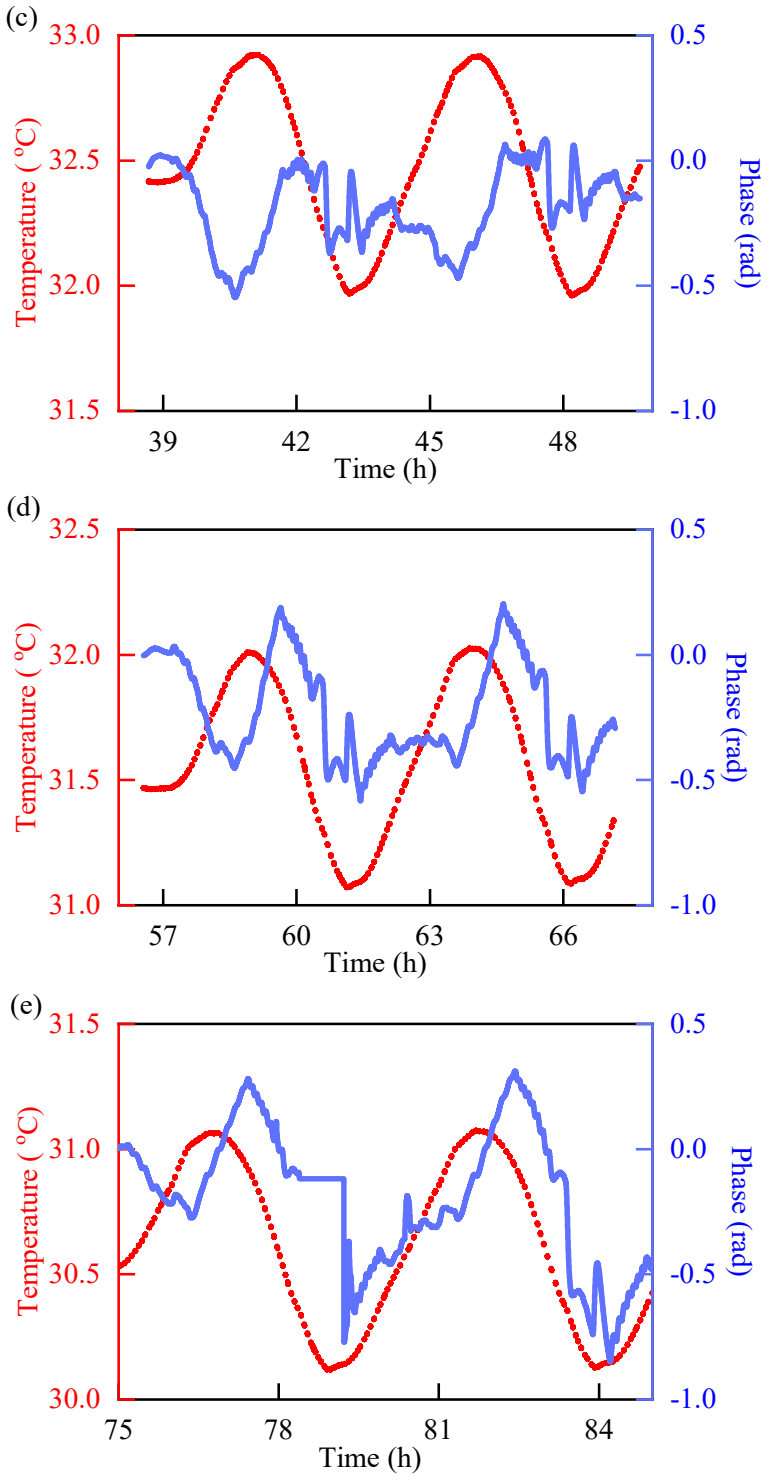
(c)
33.0
32.5
32.0
31.5
Temperature (°C)
0.5
0.0
-0.5
-1.0
Phase (rad)
39
42
45
48
Time (h)
(d)
32.5
32.0
31.5
31.0
Temperature (°C)
0.5
0.0
-0.5
-1.0
Phase (rad)
57
60
63
66
Time (h)
(e)
31.5
31.0
30.5
30.0
Temperature (°C)
0.5
0.0
-0.5
-1.0
Phase (rad)
75
78
81
84
Time (h)

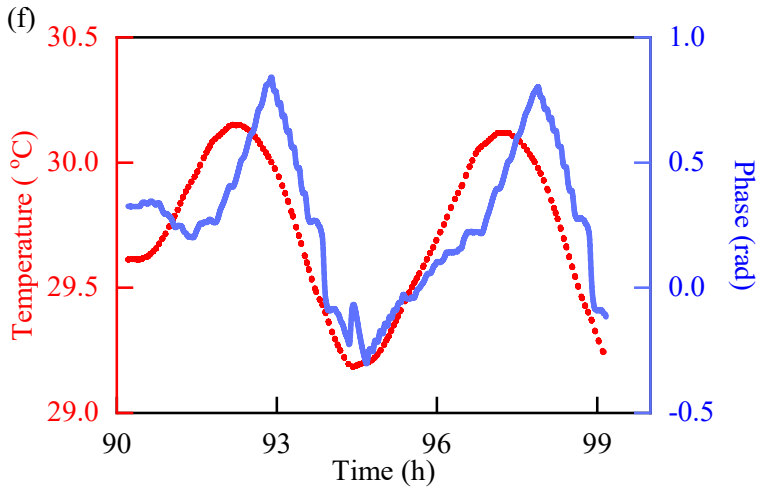

FIGURE 6.4:The phase change of the interferometer (blue solid) with temperature perturbation (red dash) at different centre temperature. Temperature is controlled to be a sinusoidal wave, of which the amplitude is about ±0.5 °C. The drift of the phase has been removed, and the phase change reaches minimum at same scale temperature perturbation at 31-32°C and 32-33 °C.

6.2.2 Long term stability and laser stabilization

Stabilizing the temperature at 32 °C, the long-term phase perturbation of thermally insensitive fibre interferometer is obtained, FIGURE 6.5(a). The phase drifting is due to the relaxation of coating, of which the slope is about 10Hz/s obtained by linear fitting. When the drift is removed, the thermal induced phase perturbation is shown in FIGURE 6.5 (b), and this small perturbation may be due to the thermal distribution of the interferometer is not ideally uniform.

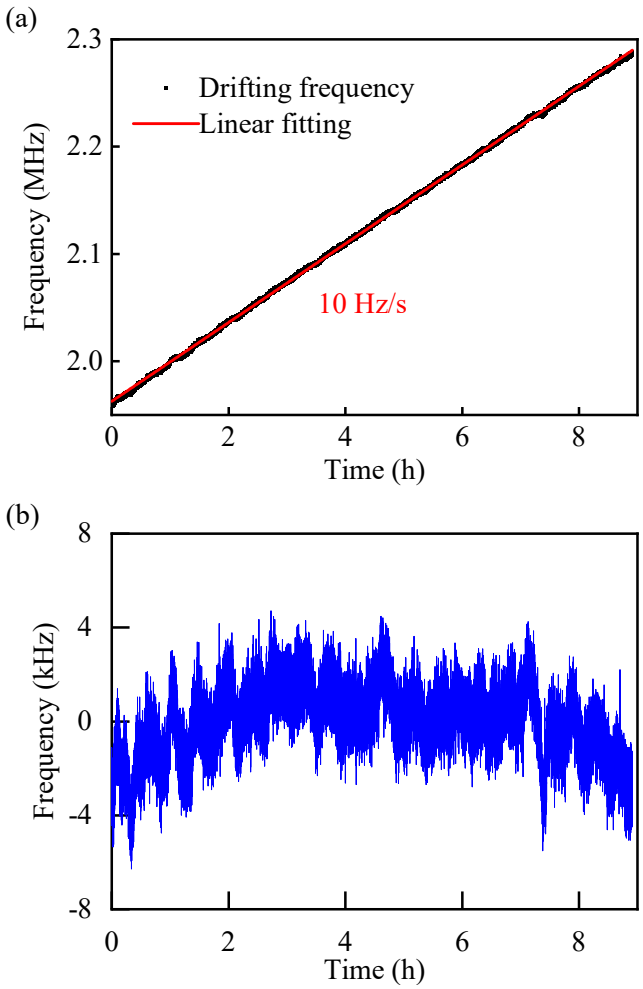

FIGURE 6.5: Phase (here transferred to frequency) perturbation of compensated interferometer at zero-sensitivity temperature: 31 °C (±0.01 °C): (a) Frequency drifting of the compensated fibre interferometer when temperature is stabilized at 32°C. (b) the frequency perturbation after removing the linear drift.

Allan deviation is commonly used to evaluate the frequency instability of interferometer and lasers [125]. I calculated Allan deviation of the phase perturbation (over 10^4 s) in FIGURE 6.5 (b) and compared that of with commercial lasers, see FIGURE 6.6.

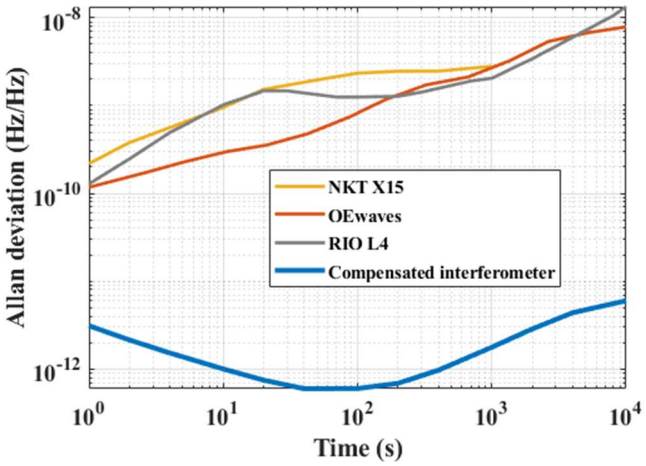

FIGURE 6.6: Allan deviation of the thermally insensitive fibre interferometer which is stabilized at temperature 31 °C. and some commercial lasers.

From 1 s to 10^4, Allan deviation of compensated fibre interferometer is always slower than that of commercial lasers. At 1 s, it is about 2×10^{-10}, which in this short time scale is dominated by the flicker and white PM noise, while at 100 s, where the temperature perturbation determined, it reaches the minimum, 6×10^{-12}, which is about three orders of magnitude stable than commercial lasers. Even for longer time scale, 10^3 to 10^4 s, it slightly increases and not over 10^{-11} at 10^4 s.

6.3 Third generation of compensated fibre interferometer

The MZI suffers from the polarization degradation which will degrade its performance. As discussed in Chapter3, employing FRMs is the most descent method to reduce the polarization degradation. Here we update our structure of the compensated interferometer from MZI to MI by removing the output coupler and adding the FRMs. SMF and HCF are connected using the angle-splicing method to reduce the back-reflection. The structure is shown in FIGURE 6.7. and it has several differences compared with the previous MZI. First, the 2×2 coupler is removed, and two FRMs are spliced to the end of the fibre spool, which will provide a polarization maintenance and double the delay length. Then the 3×3 coupler was used as both input and output ports. Shown in the figure, the connection between GRIN and HCF was not a flat connection but with an angle, which is about 2.5°, it reduced the back-reflection (from GRIN to HCF or HCF to GRIN) down to < -40 dB (-43 dB for the first connection point, and -40 dB for the other), extra connection loss of 2 dB was added which is still acceptable. To improve the visibility, we added extra loss (-4.5 dB) in the compensated arm. The spare port of 3×3 coupler was cut short and blocked by cleaved in large angle and covered with refractive index matching gel to get rid of the Rayleigh scattering along the SMF and the back-reflection from the end surface. The stability of this interferometer will be evaluated by stabilizing the free running laser in later chapter.

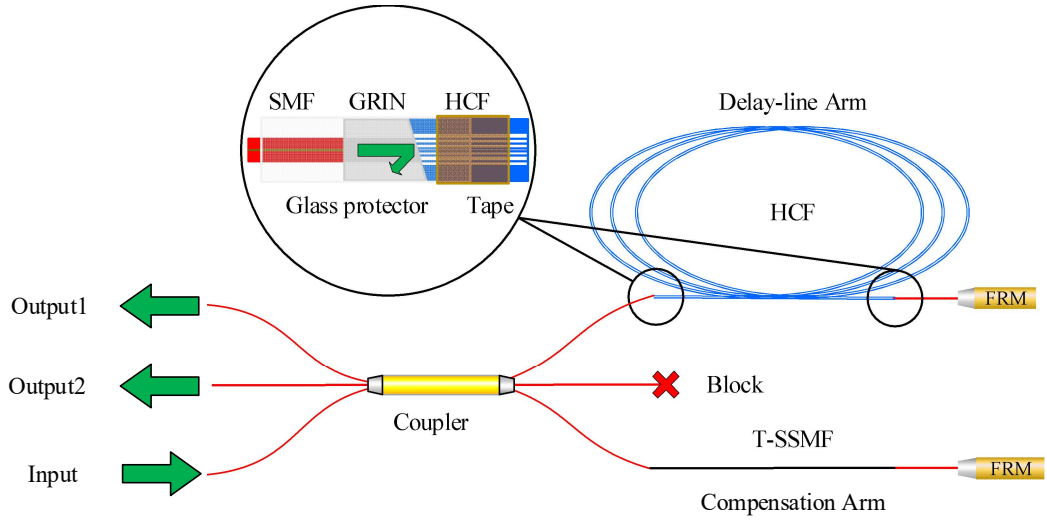

FIGURE 6.7: Structure of the compensated Michelson. Here angle-splicing connection between HCF and SMF system is employed to decrease the reflection from the interface between GRIN and HCF, the spare port of 3×3 coupler is blocked, to avoid the back-reflection from the end face.

Chapter 7 Demonstration of laser stabilization to thermally insensitive fibre interferometers

In this chapter, we demonstrate the application of laser stabilization of the thermally insensitive fibre delay-line interferometer. we introduce the laser stabilization to the thermally insensitive MZI and thermally insensitive MI, including the stabilization systems and the results.

7.1 Configuration of laser stabilization

7.1.1 Laser stabilized to the thermally insensitive Mach-Zehnder interferometer

The configuration of laser stabilization to the thermally insensitive Mach-Zehnder interferometer is shown in FIGURE 7.1. The laser employed here is a Rio laser (RIO Orion from NuFern, PLANEX 1550 nm Laser Diode) [126], of which the maximum modulation frequency is 1.5 GHz. The working current is set as 85 mA, and temperature is 27 °C. It is modulated to 50 kHz by the laser stabilization device, Moku: Go [127]. Light was split into two ports: 10% was send into the thermally insensitive fibre MZI, of which the output is received by the photodetector, and transfer optical signal to electrical signal and sent to Moku: Go; 90% is sent to beat with the optical frequency comb output, which is picked by an optical filter, here polarization controller (PC) is used to control the polarization of light beam out of the SMF optical filter, optimizing interference between two beams. The beat signal is then detected by photodetector and filtered by bandpass filter which is then recorded by the frequency counter.

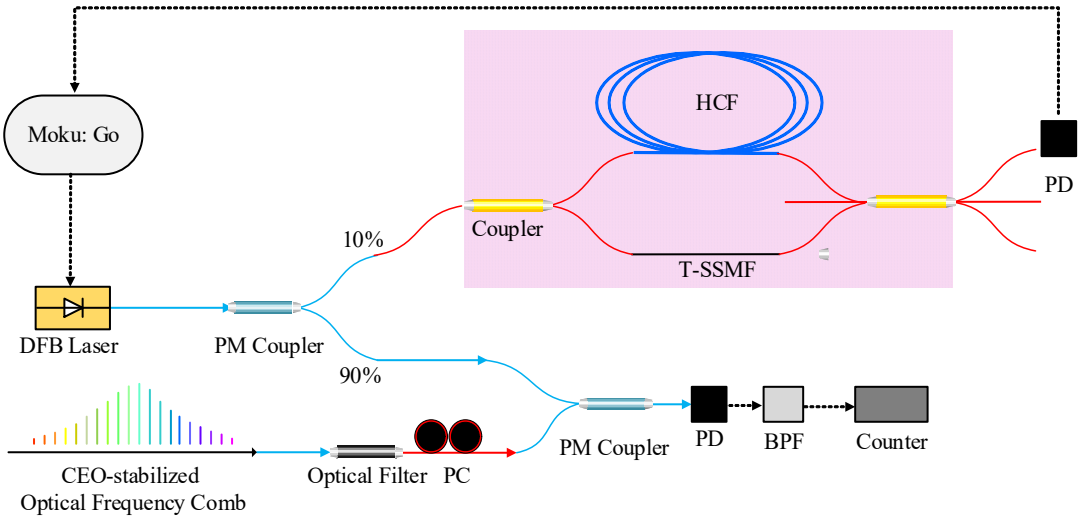

FIGURE 7.1: Schematic of the laser stabilized to the thermally insensitive Mach-Zehnder interferometer and beat with optical frequency comb. PC: polarization controller; PD: Photodetector; BPF: band pass filter.

The configuration of Moku: Go is shown in FIGURE 7.2. The detected light signal is mixed with modulation frequency (50 kHz), which is also sent to the laser modulating the frequency. The mixed signal is then filtered by a lowpass filter, of which the up limit is set as 5 kHz. The filtered signal is sent to the fast controller, it is a PID control system. Before close the loop, the scan is on, by tuning the scan frequency and amplitude, the error signal is optimized. Once close the loop, the scan is off, and by tuning the PID parameters in fast control panel, the laser is stabilized. The centre frequency can be slightly shifted by adjusting the offset voltage at the cross point after the modulation.

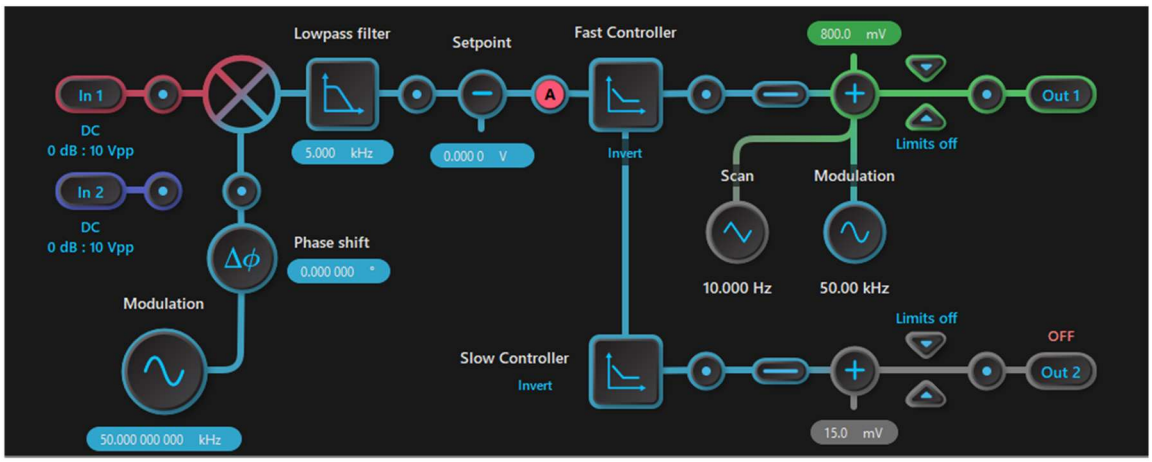

FIGURE 7.2: Configuration of the Moku: Go in software interface.

Here only the fast control is employed to achieve the stabilization as we want a simple and quick experiment to demonstrate the application of our thermally insensitive delay-line fibre interferometer.

7.1.2 Laser stabilized to the thermally insensitive Michelson interferometer

The configuration of laser stabilization to the thermally insensitive Mach-Zehnder interferometer is shown in FIGURE 7.3. It is almost the same as the configuration shown in FIGURE 7.1. And the configuration of the Moku: Go was also set with the same parameters.

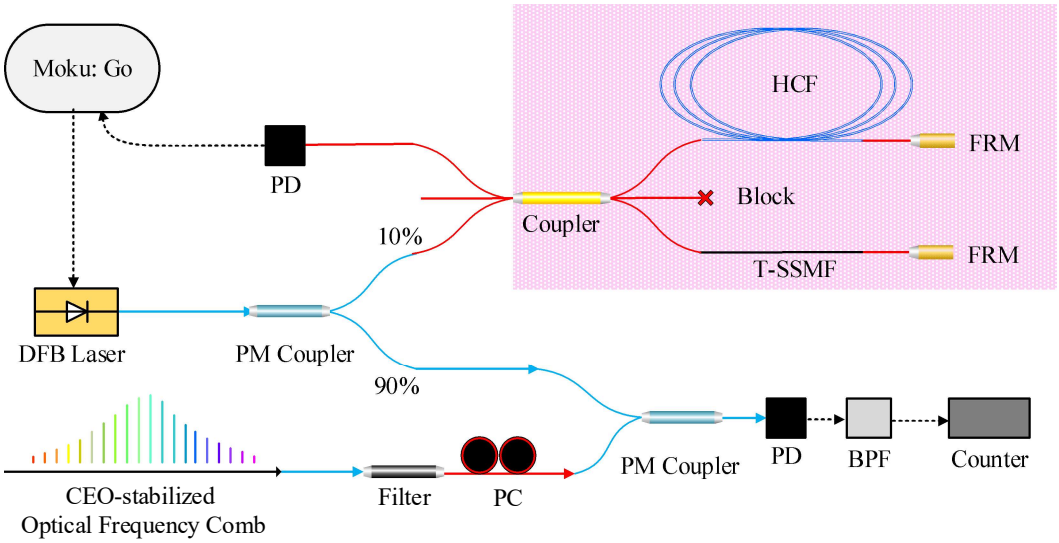

FIGURE 7.3: Schematic of the laser stabilized to the thermally insensitive Michelson interferometer and beat with optical frequency comb.

7.2 Results of laser stabilization

7.2.1 Laser stabilized to the thermally insensitive Mach-Zehnder interferometer

The beat frequency between laser stabilized to the thermally insensitive MZI and comb laser is recorded and shown in FIGURE 7.4. From the figure, there is a linear drift of the beat frequency which is about 10 Hz/s, close to the measured phase output. This drift is believed to be the relaxation of fibre coatings of both SMF and HCF, which may take years to finish. Besides the drift, the frequency beat has small perturbation which has the same period with the temperature perturbation of room temperature. Then the Allan deviation is calculated and compared with the measured phase of the thermally insensitive fibre MZI, note here both have been removed the linear drift.

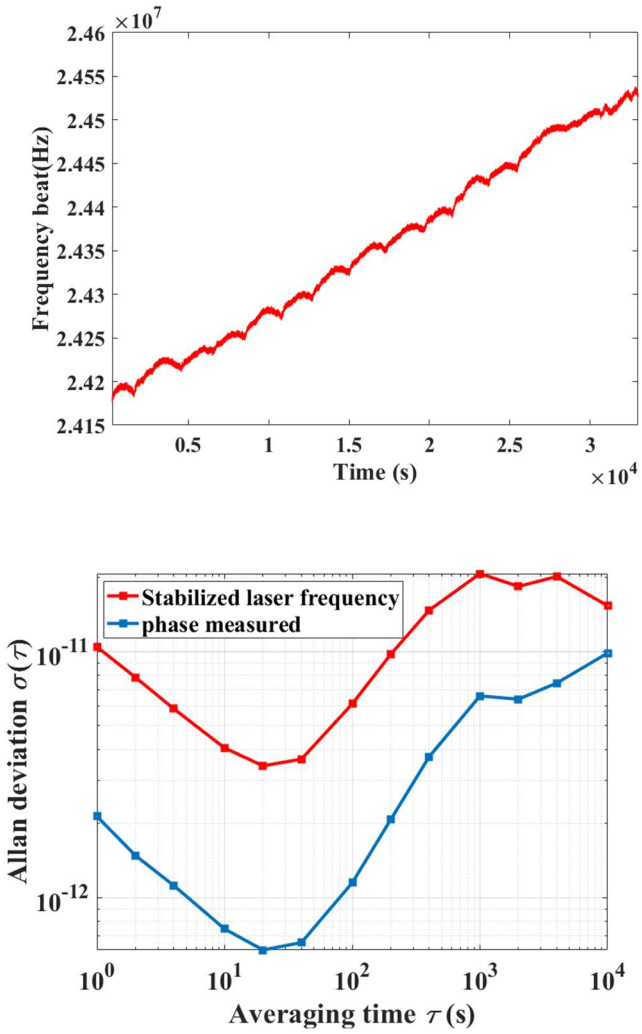

FIGURE 7.4: Frequency stability of the stabilized laser. Top: the beat frequency between the stabilized laser and comb locked laser. Bottom: the comparison of the Allan deviation between interferometer stabilized laser frequency and measured phase of the interferometer.

Compare the stability of measured phase, which has been transferred to frequency for comparison, and the beat frequency, the has the stabilized laser frequency worse stability than measured phase, which is about five times for average. As the same interferometer is used, the difference would be due to the extra noise introduced in laser stabilization systems, because it is more complicate than the phase demodulation programme and only simple configurations employed here. Over the time scale, they have similar tendency, go down to the minimum at around 50 s, and go up reach a flat level over 1000 s. Though the stabilized laser frequency is not as good as measured phase, it is still better than that of free running laser, especially for long-term scale (over one order of magnitude >100 s), shown in FIGURE 7.5. for short-term stability, it is limited by the high frequency noise, such as acoustic vibration, shot noise and so on, which have not been optimized in this thesis, while the thermal perturbation influences the low frequency stability as discussed above, and can be improved by stabilizing to the thermally insensitive fibre interferometer.

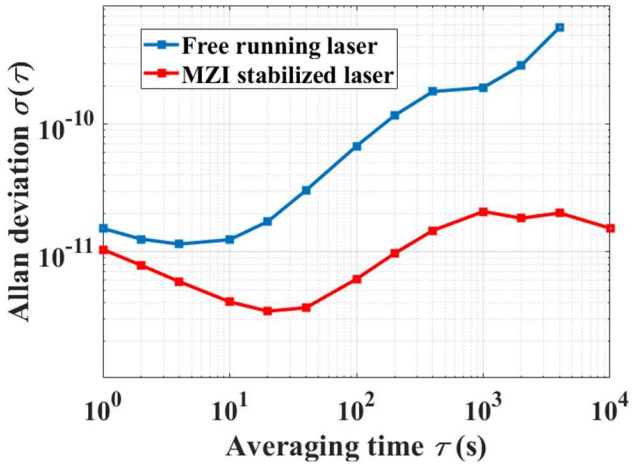

FIGURE 7.5: Comparison of frequency stability between free running laser and thermally insensitive MZI stabilized laser.

7.2.2 Laser stabilized to the thermally insensitive Michelson interferometer

The thermally insensitive MI has double delay length, and it is polarization insensitive, which is supposed to have better performance, however, when it come to the stabilized laser frequency, the stability is worse than that stabilized to the MZI. FIGURE 7.6 shows the beat frequency between comb laser and stabilized laser (left), and calculated Allan deviation of beat frequency with drift and with drift removed (right).

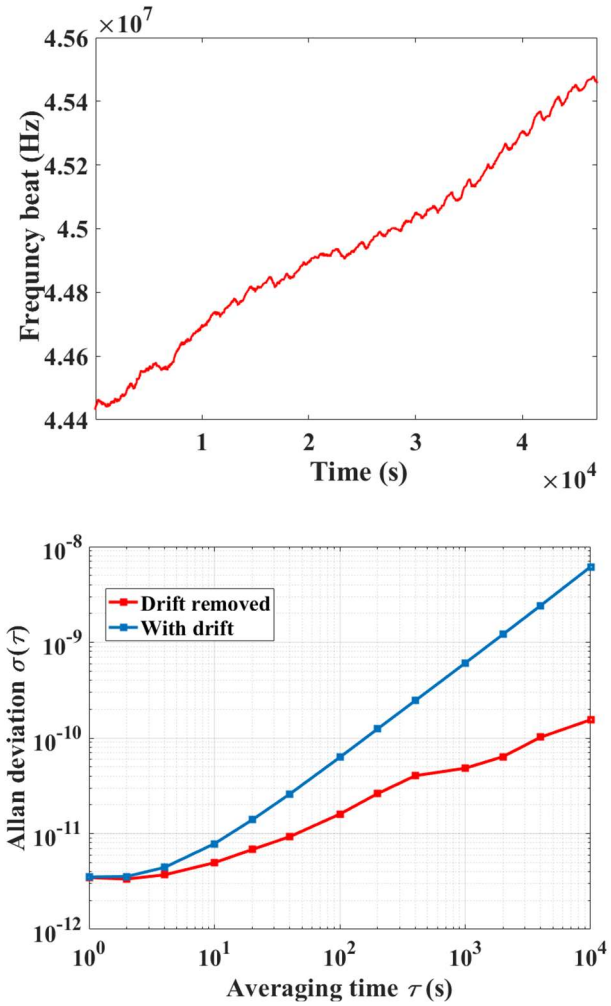

FIGURE 7.6: Top: beat frequency between fibre MI stabilized laser and OFC. Bottom: Allan deviation of the beat frequency with and without drift.

See from FIGURE 7.6, the beat frequency has the same drift as the laser stabilized to the thermally insensitive MZI, because the interferometers are made from the same fibres and stabilized at the same zero-sensitivity temperature. Besides the small periodical perturbation, which is believed caused by the temperature variation, the beat frequency has another low frequency perturbation. Here the HCF is angled cleaved and spliced with the GRIN, this back-reflection reduction method will lead to the high order mode coupling and might introduce mode interference noise. The Allan deviation of the beat frequency shows it is not as good as the beat frequency of laser stabilized to the thermally insensitive MZI. To get better results, more work needs to be done in the future.

Chapter 8 Conclusions and future work

In this chapter, we conclude the entire content and give an outlook for future work.

8.1 Conclusions

Work reported in this thesis proposed a novel structure of delay-line fibre interferometer that operates with zero thermal sensitivity at room temperature. Three generations of this interferometer were built and characterized in detail.

To achieve the thermally insensitive fibre delay-line interferometer at room temperature, we proposed a thermally insensitive fibre-compensated delay-line interferometer, which employed HCF with low thermal sensitivity as the delay arm and SMF with high thermal sensitivity in the other arm to compensate for the accumulated thermal phase change of HCF. Simulation in COMSOL showed that the compensated interferometer can be 1000 times more thermally stable than the SMF-based interferometer with the same delay length under a 1°C temperature variation when the length ratio between HCF and SMF is about 21.5:1.

The first fabricated prototype of the thermally insensitive fibre delay-line Mach-Zehnder interferometer employed a 10.8 m dual-coated HCF designed and fabricate for telecom applications. To characterize the interferometer, we built an experimental setup to measure the thermally-induced phase change by counting the peaks of interference fringes with temperature variation. However, the measured thermal sensitivity using different SMF lengths in the compensating arm did not agree with the predictions. To investigate this, we measured the thermal sensitivity of HCF with a more accurate phase extraction method that employed a 3×3 coupler to construct the interferometer. we also stabilized the interrogating laser to a carrier-envelope-offset stabilized optical frequency comb to avoid any errors due to the laser carrier frequency drift. Results showed that the thermal sensitivity of the dual-coated HCF is about 5.8 rad/m/K, which is over two times larger than in the previously reported HCF. Additionally, we observed a drift in the phase change even after the stabilization of temperature, which was found to be due to the viscoelastic properties of the coating. This effect was found to be very strong in the dual-coated HCFs. These results suggested that the latest generation of HCFs that have dual-layer coating (similarly to SMFs) performs worse in terms of thermal stability than the earlier single-coated designs.

Following our study, an HCF with thin single-layer coating was designed and fabricated in the ORC. By replacing the dual-coated HCF with a single thinly-coated HCF (10 μm thickness of

coating), whose thermal sensitivity was measured to be 1.7 rad/m/K and compensating with single thinly-coated SMF (also manufactured in the ORC, 10 μm thickness of coating) in the other arm, we fabricated the first generation of thermally insensitive fibre delay-line interferometer. Zero thermal sensitivity was achieved at 28°C, and the zero-sensitivity temperature was tuned from 28°C to 45°C via control of the SMF length. Compared with an SMF-based interferometer, the compensated delay-line interferometer showed about 1000 times lower thermal sensitivity when the temperature was ± 1 °C away from the zero-sensitivity temperature and 100 times lower thermal sensitivity in a large temperature range of 25–50°C. The relationship between the thermal sensitivity changes and wavelength showed the compensated interferometer was expected to achieve 2 million lower sensitivities than its SMF counterpart even when the wavelength was tuned by as much as 240 nm.

To further stabilize the interferometer output, we improved the polarization control and implemented feedback to further reduce power fluctuations due to fluctuations in the polarization. Additionally, we placed the interferometer inside a metallic box that we sealed with silicone, avoiding phase perturbation due to ambient pressure fluctuations. Box sealing reduced ambient pressure variations by a factor of 20, significantly improving interferometer long-term stability.

The HCF with 10 μm thick coting unfortunately kept breaking. we fabricated the second generation thermally insensitive fibre delay-line interferometer with HCF fabricated in the ORC that had thicker glass cladding and relatively thin single-layer coating (30 μm). The thermal sensitivity was measured as 1.64 rad/m/K, which is a value very close to the 10 μm coated HCF, making the coating influence (especially in terms of the phase drifting) similar to the 10 μm coated HCF. However, mechanical stability was strongly improved, without any fibre breaks observed during the experiments. The zero-sensitivity temperature was tuned to be 30.8°C. To characterize the thermal instability of compensated interferometer under small temperature variations, the temperature in the thermal chamber was set to be a sinusoidal function of time, of which the amplitude was about 1°C. The smallest thermal instability was measured to be 8 mrad/m/K at 31–33°C. Thus, the temperature was stabilized at 31°C, and long-term phase variations were characterized by calculating the Allan deviation after removing the observed long-term phase drift of 10 Hz/s. Comparing this result to Allan deviation measured with commercially-available stable lasers, the compensated interferometer had lower Allan deviation in the 1-10^4 s time scale. At 100 s time scale, it reached three orders of magnitude better stability. To double the delay length and reduce the instabilities due to polarization, we fabricated thermally insensitive Michelson interferometer by employing the angle-splicing HCF-SMF technique and Faraday rotator mirrors, which represents the third generation of our compensated interferometer design.

To demonstrate the application of the thermally insensitive fibre delay-line interferometers, preliminary experiments for laser stabilization via PDH method were carried out. Stability was

characterized by comparing the locked laser to our carrier-envelope-offset stabilized optical frequency comb. Results showed that stabilized laser frequency follows the linear drift measured in the interferometer. To evaluate the long-term stability, the Allan deviation of the beat frequency was calculated. The thermally insensitive interferometer stabilized laser showed worse long-term stability than that of the interferometer characterized by the phase measurement, which is due to the more complicated system of laser stabilization and the fact that less attention has been paid to reducing the extra noise in this work; however, it is still one order of magnitude better than the free-running laser. The minimum Allan deviation of 3×10^{-12} was achieved with averaging time of 20 s. It kept stable around 2×10^{-11} at 1000 s time scales.

In conclusion, I believe the proposed compensated fibre delay-line interferometers have the potential to enhance performance in applications requiring thermally insensitive fibre interferometers operating at room temperature.

8.2 Future work

While research summarized in this thesis represents significant advancement in the field of thermally-insensitive interferometers, there are still several opportunities to further improve the performance.

1. Low-loss, low-back-reflection connections. The third generation of the thermally insensitive fibre interferometer employed angled splicing between the HCF and SMF to reduce back-reflection from the air-glass interface. However, this approach introduced high-order mode transmission, accumulated thermal perturbation at the connection point, and limited the delay length due to higher loss. Utilizing the latest reported method, which involves splicing angle-cleaved mode field adaptors to the HCF with an offset, could provide a low back-reflection connection with lower loss. This would improve the overall performance and stability of the interferometer.

2. Increased the delay length. The HCF used in this thesis is relatively lossy, which limits the maximum achievable delay length of the interferometer. Designing an HCF with the same thermal stability but lower loss would allow for longer delay lengths and significantly improve the interferometer's performance, particularly in laser stabilizations where longer delay lengths can be beneficial.

3. Uniform thermal distribution. In this thesis, the temperature distribution inside the box was assumed to be uniform everywhere, and the time constants of the HCF and SMF were the same. While this assumption works well for shorter delay lengths (e.g., <100 m), it may not hold true for longer delay lengths, such as tens or hundreds of meters. For such cases, it is essential to design special winding spools to ensure a more uniform thermal distribution along the length of the fibre.

Additionally, employing a vacuum chamber could provide an opportunity to achieve the best possible performance for this compensated interferometer by minimizing external temperature influences.

These suggested improvements have the potential to further enhance the thermally insensitive fibre interferometer's performance, making it even more versatile and valuable for various applications, including laser stabilization and other precision measurement tasks.

Reference

[1] Martienssen, W., & Spiller, E. (1964). Coherence and fluctuations in light beams. *American Journal of Physics*, *32*(12), 919-926.

[2] Whybray, M. (2011). Measuring the Speed of Light.

[3] Lawall, J., & Kessler, E. (2000). Michelson interferometry with 10 pm accuracy. *Review of Scientific Instruments*, *71*(7), 2669-2676.

[4] Morthier, G., Sun, J., Gyselings, T., & Baets, R. (1998, February). A novel optical decision circuit based on a Mach-Zehnder interferometer and gain-clamped semiconductor optical amplifiers. In *OFC'98. Optical Fibre Communication Conference and Exhibit. Technical Digest. Conference Edition. 1998 OSA Technical Digest Series Vol. 2 (IEEE Cat. No. 98CH36177)* (pp. 198-199). IEEE.

[5] Michelson, A. A. (1928). Experimental determination of the velocity of light. *The Scientific Monthly*, *27*(6), 562-565.

[6] Ludlow, A. D., Boyd, M. M., Ye, J., Peik, E., & Schmidt, P. O. (2015). Optical atomic clocks. *Reviews of Modern Physics*, *87*(2), 637.

[7] Vaughan, M. (2017). *The Fabry-Perot interferometer: history, theory, practice and applications*. Routledge.

[8] Singh, M., Tuck, C. J., & Fernando, G. F. (1999). Multiplexed optical fibre Fabry-Perot sensors for strain metrology. *Smart materials and structures*, *8*(5), 549.

[9] Swart, P. L. (2004). Long-period grating Michelson refractometric sensor. *Measurement Science and Technology*, *15*(8), 1576.

[10] Atherton, P. D., Reay, N. K., Ring, J., & Hicks, T. R. (1981). Tunable fabry-perot filters. *Optical Engineering*, *20*(6), 806-814.

[11] Abbott, B. P., Abbott, R., Adhikari, R., Ajith, P., Allen, B., Allen, G., ... & Giardina, K. D. (2009). LIGO: the laser interferometer gravitational-wave observatory. *Reports on Progress in Physics*, *72*(7), 076901.

[12] https://jrogel.com/ligo-architects-win-nobel-prize-in-physics/

[13] Faix, O. (1992). Fourier transform infrared spectroscopy. In *Methods in lignin chemistry* (pp. 83-109). Berlin, Heidelberg: Springer Berlin Heidelberg.

[14] Robinson, J. M., Oelker, E., Milner, W. R., Zhang, W., Legero, T., Matei, D. G., ... & Ye, J. (2019). Crystalline optical cavity at 4 K with thermal-noise-limited instability and ultralow drift. Optica, 6(2), 240-243.

[15] Black, E. D. (2001). An introduction to Pound–Drever–Hall laser frequency stabilization. *American journal of physics*, *69*(1), 79-87.

[16] Li, L., Xia, L., Xie, Z., & Liu, D. (2012). All-fibre Mach-Zehnder interferometers for sensing applications. *Optics express*, *20*(10), 11109-11120.

[17] Kashyap, R., & Nayar, B. (1983). An all single-mode fibre Michelson interferometer sensor. *journal of Lightwave Technology*, *1*(4), 619-624.

[18] Wada, A., Tanaka, S., & Takahashi, N. (2011). Optical fibre vibration sensor using FBG Fabry–Perot interferometer with wavelength scanning and Fourier analysis. *IEEE Sensors Journal*, *12*(1), 225-229.

[19] Merlo, S., Norgia, M., & Donati, S. (2000). Fibre gyroscope principles. *Handbook of Fibre Optic Sensing Technology*, 1-23.

[20] Nash, P. (1996). Review of interferometric optical fibre hydrophone technology. *IEE Proceedings-Radar, Sonar and Navigation*, *143*(3), 204-209.

[21] Lu, Y., Zhu, T., Chen, L., & Bao, X. (2010). Distributed vibration sensor based on coherent detection of phase-OTDR. *Journal of lightwave Technology*, *28*(22), 3243-3249.

[22] Świerad, D., Häfner, S., Vogt, S., Venon, B., Holleville, D., Bize, S., ... & Sterr, U. (2016). Ultra-stable clock laser system development towards space applications. *Scientific Reports*, *6*(1), 33973.

[23] Pitkin, M., Reid, S., Rowan, S., & Hough, J. (2011). Gravitational wave detection by interferometry (ground and space). *Living Reviews in Relativity*, *14*, 1-75.

[24] Barish, B. C., & Weiss, R. (1999). LIGO and the detection of gravitational waves. *Physics Today*, *52*(10), 44-50.
[25] McFerran, J. J., Ivanov, E. N., Bartels, A., Wilpers, G., Oates, C. W., Diddams, S. A., & Hollberg, L. (2005). Low-noise synthesis of microwave signals from an optical source. *Electronics Letters*, *41*(11), 1.
[26] Schioppo, M., Kronjaeger, J., Silva, A., Ilieva, R., Paterson, J. W., Baynham, C. F. A., ... & Grosche, G. (2022). Comparing ultrastable lasers at 7×10^{-17} fractional frequency instability through a 2220 km optical fibre network. *Nature communications*, *13*(1), 212.
[27] Kessler, T., Hagemann, C., Grebing, C., Legero, T., Sterr, U., Riehle, F., ... & Ye, J. (2012). A sub-40-mHz-linewidth laser based on a silicon single-crystal optical cavity. *Nature Photonics*, *6*(10), 687-692.
[28] Kéfélian, F., Jiang, H., Lemonde, P., & Santarelli, G. (2009). Ultralow-frequency-noise stabilization of a laser by locking to an optical fibre-delay line. *Optics letters*, *34*(7), 914-916.
[29] Alnis, J., Schliesser, A., Wang, C. Y., Hofer, J., Kippenberg, T. J., & Hänsch, T. W. (2011). Thermal-noise-limited crystalline whispering-gallery-mode resonator for laser stabilization. *Physical Review A*, *84*(1), 011804.
[30] Washburn, B. R., Diddams, S. A., Newbury, N. R., Nicholson, J. W., Yan, M. F., & Jørgensen, C. G. (2004). Phase-locked, erbium-fibre-laser-based frequency comb in the near infrared. Optics letters, 29(3), 250-252.
[31] Sheard, B. S., Heinzel, G., Danzmann, K., Shaddock, D. A., Klipstein, W. M., & Folkner, W. M. (2012). Intersatellite laser ranging instrument for the GRACE follow-on mission. Journal of Geodesy, 86, 1083-1095.
[32] Chiodo, N., Djerroud, K., Acef, O., Clairon, A., & Wolf, P. (2013). Lasers for coherent optical satellite links with large dynamics. Applied optics, 52(30), 7342-7351.
[33] Seymour-Smith, N., Blythe, P., Keller, M., & Lange, W. (2010). Fast scanning cavity offset lock for laser frequency drift stabilization. Review of Scientific Instruments, 81(7).
[34] Galiev, R. R., Kondratiev, N. M., Lobanov, V. E., Matsko, A. B., & Bilenko, I. A. (2020). Optimization of laser stabilization via self-injection locking to a whispering-gallery-mode microresonator. Physical Review Applied, 14(1), 014036.
[35] Hansch, T. W., & Couillaud, B. (1980). Laser frequency stabilization by polarization spectroscopy of a reflecting reference cavity. Optics communications, 35(3), 441-444.
[36] Numata, K., Kemery, A., & Camp, J. (2004). Thermal-noise limit in the frequency stabilization of lasers with rigid cavities. *Physical review letters*, *93*(25), 250602.
[37] Stoehr, H., Mensing, F., Helmcke, J., & Sterr, U. (2006). Diode laser with 1 Hz linewidth. *Optics letters*, *31*(6), 736-738.
[38] Nazarova, T., Riehle, F., & Sterr, U. (2006). Vibration-insensitive reference cavity for an ultra-narrow-linewidth laser. *Applied Physics B*, *83*, 531-536.
[39] Ludlow, A. D., Huang, X., Notcutt, M., Zanon-Willette, T., Foreman, S. M., Boyd, M. M., ... & Ye, J. (2007). Compact, thermal-noise-limited optical cavity for diode laser stabilization at 1×10^{-15}. *Optics letters*, *32*(6), 641-643.
[40] Alnis, J., Matveev, A., Kolachevsky, N., Udem, T., & Hänsch, T. W. (2008). Subhertz linewidth diode lasers by stabilization to vibrationally and thermally compensated ultralow-expansion glass Fabry-Pérot cavities. *Physical Review A*, *77*(5), 053809.
[41] Millo, J., Magalhães, D. V., Mandache, C., Le Coq, Y., English, E. M. L., Westergaard, P. G., ... & Santarelli, G. (2009). Ultrastable lasers based on vibration insensitive cavities. *Physical Review A*, *79*(5), 053829.
[42] He, L., Zhang, J., Wang, Z., Chang, J., Wu, Q., Lu, Z., & Zhang, J. (2023). Ultra-stable cryogenic sapphire cavity laser with an instability reaching 2×10^{-16} based on a low vibration level cryostat. *Optics Letters*, *48*(10), 2519-2522.
[43] Zhang, W., Robinson, J. M., Sonderhouse, L., Oelker, E., Benko, C., Hall, J. L., ... & Ye, J. (2017). Ultrastable silicon cavity in a continuously operating closed-cycle cryostat at 4 K. *Physical review letters*, *119*(24), 243601.
[44] Guo, J., McLemore, C. A., Xiang, C., Lee, D., Wu, L., Jin, W., ... & Bowers, J. E. (2022). Chip-based laser with 1-hertz integrated linewidth. *Science advances*, *8*(43), eabp9006.
[45] Chen, Y. T. (1989). Use of single-mode optical fibre in the stabilization of laser frequency. *Applied optics*, *28*(11), 2017-2021.

[46] Cranch, G. A. (2002). Frequency noise reduction in erbium-doped fibre distributed-feedback lasers by electronic feedback. *Optics letters*, *27*(13), 1114-1116.
[47] Sheard, B. S., Gray, M. B., & McClelland, D. E. (2006). High-bandwidth laser frequency stabilization to a fibre-optic delay line. *Applied optics*, *45*(33), 8491-8499.
[48] Cliche, J. F., Allard, M., & Têtu, M. (2006, May). High-power and ultranarrow DFB laser: the effect of linewidth reduction systems on coherence length and interferometer noise. In *Laser source and system technology for defense and security II* (Vol. 6216, pp. 83-93). SPIE.
[49] Crozatier, V., Gorju, G., Bretenaker, F., Le Gouët, J. L., Lorgeré, I., Gagnol, C., & Ducloux, E. (2006). Phase locking of a frequency agile laser. *Applied physics letters*, *89*(26).
[50] Takahashi, K., Ando, M., & Tsubono, K. (2008, July). Stabilization of laser intensity and frequency using optical fibre. In *Journal of Physics: Conference Series* (Vol. 122, No. 1, p. 012016). IOP Publishing.
[51] Huang, J., Wang, L., Duan, Y., Huang, Y., Ye, M., Li, L., ... & Li, T. (2019). Vibration-insensitive fibre spool for laser stabilization. *Chinese Optics Letters*, *17*(8), 081403.
[52] Jeon, I., Ahn, C., Kim, C., Park, S., Jeon, W., & Kim, J. (2023, May). Compact and Robust Laser Stabilization System Using a Vibration-Insensitive All-Fibre Ring-Resonator. In *CLEO: Science and Innovations* (pp. SM2K-5). Optica Publishing Group.
[53] Li, T., Argence, B., Haboucha, A., Jiang, H., Dornaux, J. L., Koné, D., ... & Burt, E. (2011, May). Low vibration sensitivity fibre spools for laser stabilization. In *2011 Joint Conference of the IEEE International Frequency Control and the European Frequency and Time Forum (FCS) Proceedings* (pp. 1-3). IEEE.
[54] Huang, Y., Hu, D., Ye, M., Wang, Y., Li, Y., Li, M., ... & Li, T. (2023). All-fibre-based ultrastable laser with long-term frequency stability of 1.1× 10-14. *Chinese Optics Letters*, *21*(3), 031404.
[55] Kong, J., Lucivero, V. G., Jiménez-Martínez, R., & Mitchell, M. W. (2015). Long-term laser frequency stabilization using fibre interferometers. *Review of Scientific Instruments*, *86*(7).
[56] Merkel, B., Repp, D., & Reiserer, A. (2021). Laser stabilization to a cryogenic fibre ring resonator. *Optics Letters*, *46*(2), 444-447.
[57] Bousonville, M., Bock, M. K., Felber, M., Ladwig, T., Lamb, T., Schlarb, H., ... & Jablonski, S. (2012, April). New phase stable optical fibre. In *Proc. Beam Instrum. Workshop* (pp. 101-103).
[58] Bondza, S. (2019). Design of a temperature insensitive fibre interferometer for long-term laser frequency stabilization using metal coated fibres.
[59] Dragic, P., Cavillon, M., & Ballato, J. (2017). On the thermo-optic coefficient of P 2 O 5 in SiO 2. *Optical Materials Express*, *7*(10), 3654-3661.
[60] Feng, Z., Michaud-Belleau, V., Sahu, J. K., Nilsson, J., Codemard, C. A., Zhang, X., ... & Slavík, R. (2020, September). Fibre interferometry with low temperature sensitivity. In *2020 IEEE Photonics Conference (IPC)* (pp. 1-2). IEEE.
[61] Zhu, W., Fokoua, E. R. N., Taranta, A. A., Chen, Y., Bradley, T., Petrovich, M. N., ... & Slavík, R. (2019). The thermal phase sensitivity of both coated and uncoated standard and hollow core fibres down to cryogenic temperatures. *Journal of Lightwave Technology*, *38*(8), 2477-2484.
[62] Dangui, V., Kim, H. K., Digonnet, M. J., & Kino, G. S. (2005). Phase sensitivity to temperature of the fundamental mode in air-guiding photonic-bandgap fibres. *Optics Express*, *13*(18), 6669-6684.
[63] Slavík, R., Marra, G., Fokoua, E. N., Baddela, N., Wheeler, N. V., Petrovich, M., ... & Richardson, D. J. (2015). Ultralow thermal sensitivity of phase and propagation delay in hollow core optical fibres. *Scientific reports*, *5*(1), 15447.
[64] Zhu, W., Fokoua, E. N., Chen, Y., Bradley, T., Petrovich, M. N., Poletti, F., ... & Slavík, R. (2019). Temperature insensitive fibre interferometry. *Optics Letters*, *44*(11), 2768-2770.
[65] Feng, Z., Sakr, H., Hayes, J. R., Fokoua, E. N., Ding, M., Poletti, F., ... & Slavík, R. (2023). Hollow-core fibre with stable propagation delay between− 150° C and+ 60° C. *Optics Letters*, *48*(3), 763-766.
[66] Slavík, R., Fokoua, E. N., Bukshtab, M., Chen, Y., Bradley, T. D., Sandoghchi, S. R., ... & Richardson, D. J. (2019). Demonstration of opposing thermal sensitivities in hollow-core fibres with open and sealed ends. *Optics letters*, *44*(17), 4367-4370.
[67] Ding, M., Fokoua, E. N., Hayes, J. R., Sakr, H., Horak, P., Poletti, F., ... & Slavík, R. (2022). Hollow-core fibre Fabry–Perot interferometers with reduced sensitivity to temperature. *Optics Letters*, *47*(10), 2510-2513.

[68] Wei, X., Taranta, A., Shi, B., Ding, M., Feng, Z., Richardson, D. J., ... & Slavík, R. (2023). Support-Free Thermally Insensitive Hollow Core Fibre Coil. *Journal of Lightwave Technology*, *41*(10), 3145-3152.
[69] Scofield, J. H. (1994). Frequency-domain description of a lock-in amplifier. American journal of Okoshi, T. (1985). Polarization-state control schemes for heterodyne or homodyne optical fibre communications. *IEEE Transactions on Electron Devices*, *32*(12), 2624-2629.
[70] Martinelli, M., & Martelli, P. (2017). Polarization, mirrors, and reciprocity: birefringence and its compensation in optical retracing circuits. *Advances in Optics and Photonics*, *9*(1), 129-168.
[71] Merlo, S., Norgia, M., & Donati, S. (2000). Fibre gyroscope principles. *Handbook of Fibre Optic Sensing Technology*, 1-23.
[72] Bergh, R. A., Lefevre, H. C., & Shaw, H. J. (1981). All-single-mode fibre-optic gyroscope. *Optics letters*, *6*(4), 198-200.
[73] Yoshino, T., Kurosawa, K., Itoh, K., & Ose, T. (1982). Fibre-optic Fabry-Perot interferometer and its sensor applications. *IEEE Transactions on Microwave Theory and Techniques*, *30*(10), 1612-1621.
[74] Pfeifer, H., Ratschbacher, L., Gallego, J., Saavedra, C., Faßbender, A., von Haaren, A., ... & Meschede, D. (2022). Achievements and perspectives of optical fibre Fabry–Perot cavities. *Applied Physics B*, *128*(2), 29.
[75] Jiang, H. (2010). *Development of ultra-stable laser sources and long-distance optical link via telecommunication networks* (Doctoral dissertation, Université Paris-Nord-Paris XIII).
[76] Wanser, K. H. (1992). Fundamental phase noise limit in optical fibres due to temperature fluctuations. *Electronics letters*, *28*, 53.
[77] Glenn, W. H. (1989). Noise in interferometric optical systems: An optical Nyquist theorem. *IEEE journal of quantum electronics*, *25*(6), 1218-1224.
[78] Bartolo, R. E., Tveten, A. B., & Dandridge, A. (2012). Thermal phase noise measurements in optical fibre interferometers. *IEEE Journal of Quantum Electronics*, *48*(5), 720-727.
[79] Duan, L. (2012). General treatment of the thermal noises in optical fibres. *Physical Review A*, *86*(2), 023817.
[80] Dong, J., Huang, J., Li, T., & Liu, L. (2016). Observation of fundamental thermal noise in optical fibres down to infrasonic frequencies. *Applied Physics Letters*, *108*(2).
[81] Lagakos, N., Bucaro, J. A., & Jarzynski, J. (1981). Temperature-induced optical phase shifts in fibres. *Applied optics*, *20*(13), 2305-2308.
[82] White, G. K. (1973). Thermal expansion of reference materials: copper, silica and silicon. *Journal of Physics D: Applied Physics*, *6*(17), 2070.
[83] Li, Z., Meng, Z., Liu, T., & Yao, X. S. (2013). A novel method for determining and improving the quality of a quadrupolar fibre gyro coil under temperature variations. *Optics Express*, *21*(2), 2521-2530.
[84] Poletti, F. (2014). Nested antiresonant nodeless hollow core fibre. *Optics express*, *22*(20), 23807-23828.
[85] Pisani, N., Numkam Fokoua, E., Davidson, I. A., Poletti, F., Slavík, R., Lowe, D., ... & Sutton, G. (2022). Toward gamma ray immune fibre-optic phosphor thermometry for nuclear decommissioning. International Journal of Thermophysics, 43(4), 47.
[86] Lagakos, N., & Bucaro, J. A. (1981). Pressure desensitization of optical fibres. *Applied optics*, *20*(15), 2716-2720.
[87] Budiansky, B., Drucker, D. C., Kino, G. S., & Rice, J. R. (1979). Pressure sensitivity of a clad optical fibre. *Applied optics*, *18*(24), 4085-4088.
[88] Hartog, A., & Gold, M. (1984). On the theory of backscattering in single-mode optical fibres. *Journal of Lightwave Technology*, *2*(2), 76-82.
[89] Takada, K., Okamoto, K., Sasaki, Y., & Noda, J. (1986). Ultimate limit of polarization cross talk in birefringent polarization-maintaining fibres. *JOSA A*, *3*(10), 1594-1603.
[90] Noda, J., Okamoto, K., & Sasaki, Y. (1986). Polarization-maintaining fibres and their applications. *Journal of Lightwave Technology*, *4*(8), 1071-1089.
[91] Hobbs, P. C. (2022). *Building electro-optical systems: making it all work*. John Wiley & Sons.
[92] Poletti, F., Petrovich, M. N., & Richardson, D. J. (2013). Hollow-core photonic bandgap fibres: technology and applications. *Nanophotonics*, *2*(5-6), 315-340.
[93] Smith, C. M., Venkataraman, N., Gallagher, M. T., Müller, D., West, J. A., Borrelli, N. F., ... & Koch, K. W. (2003). Low-loss hollow-core silica/air photonic bandgap fibre. *Nature*, *424*(6949), 657-659.

[94] Amezcua-Correa, R., Gérôme, F., Leon-Saval, S. G., Broderick, N. G. R., Birks, T. A., & Knight, J. C. (2008). Control of surface modes in low loss hollow-core photonic bandgap fibres. *Optics Express*, *16*(2), 1142-1149.

[95] Poggiolini, P., & Poletti, F. (2022). Opportunities and challenges for long-distance transmission in hollow-core fibres. *Journal of Lightwave Technology*, *40*(6), 1605-1616.

[96] Benabid, F., Knight, J. C., Antonopoulos, G., & Russell, P. S. J. (2002). Stimulated Raman scattering in hydrogen-filled hollow-core photonic crystal fibre. *Science*, *298*(5592), 399-402.

[97] Wang, Y. Y., Couny, F., Roberts, P. J., & Benabid, F. (2010, May). Low loss broadband transmission in optimized core-shape Kagome hollow-core PCF. In *Conference on Lasers and Electro-Optics* (p. CPDB4). Optica Publishing Group.

[98] Belardi, W., & Knight, J. C. (2013). Effect of core boundary curvature on the confinement losses of hollow antiresonant fibres. *Optics Express*, *21*(19), 21912-21917.

[99] Debord, B., Amsanpally, A., Chafer, M., Baz, A., Maurel, M., Blondy, J. M., ... & Benabid, F. (2017). Ultralow transmission loss in inhibited-coupling guiding hollow fibres. *Optica*, *4*(2), 209-217.

[100] Belardi, W., & Knight, J. C. (2014). Hollow antiresonant fibres with reduced attenuation. *Optics letters*, *39*(7), 1853-1856.

[101] Gao, S. F., Wang, Y. Y., Ding, W., Jiang, D. L., Gu, S., Zhang, X., & Wang, P. (2018). Hollow-core conjoined-tube negative-curvature fibre with ultralow loss. *Nature communications*, *9*(1), 2828.

[102] Bradley, T. D., Hayes, J. R., Chen, Y., Jasion, G. T., Sandoghchi, S. R., Slavík, R., ... & Poletti, F. (2018, September). Record low-loss 1.3 dB/km data transmitting antiresonant hollow core fibre. In *2018 European Conference on Optical Communication (ECOC)* (pp. 1-3). IEEE.

[103] Jasion, G. T., Bradley, T. D., Harrington, K., Sakr, H., Chen, Y., Fokoua, E. N., ... & Poletti, F. (2020, March). Hollow core NANF with 0.28 dB/km attenuation in the C and L bands. In *Optical Fibre Communication Conference* (pp. Th4B-4). Optica Publishing Group.

[104] Sakr, H., Bradley, T. D., Jasion, G. T., Fokoua, E. N., Sandoghchi, S. R., Davidson, I. A., ... & Poletti, F. (2021, June). Hollow core NANFs with five nested tubes and record low loss at 850, 1060, 1300 and 1625nm. In Optical Fibre Communication Conference (pp. F3A-4). Optica Publishing Group.

[105] Jasion, G. T., Sakr, H., Hayes, J. R., Sandoghchi, S. R., Hooper, L., Fokoua, E. N., ... & Poletti, F. (2022, March). 0.174 dB/km hollow core double nested antiresonant nodeless fibre (DNANF). In *2022 Optical Fibre Communications Conference and Exhibition (OFC)* (pp. 1-3). IEEE.

[106] Zuba, V., Mulvad, H. C. H., Slavík, R., Sakr, H., Poletti, F., Richardson, D. J., & Fokoua, E. N. (2023). Limits of Coupling Efficiency into Hollow-core Antiresonant Fibres. *Journal of Lightwave Technology*.

[107] Jung, Y., Kim, H., Chen, Y., Bradley, T. D., Davidson, I. A., Hayes, J. R., ... & Richardson, D. J. (2020). Compact micro-optic based components for hollow core fibres. *Optics express*, *28*(2), 1518-1525.

[108] Suslov, D., Komanec, M., Numkam Fokoua, E. R., Dousek, D., Zhong, A., Zvánovec, S., ... & Slavík, R. (2021). Low loss and high performance interconnection between standard single-mode fibre and antiresonant hollow-core fibre. *Scientific Reports*, *11*(1), 8799.

[109] Huang, W., Cui, Y., Li, X., Zhou, Z., Li, Z., Wang, M., ... & Wang, Z. (2019). Low-loss coupling from single-mode solid-core fibres to anti-resonant hollow-core fibres by fibre tapering technique. *Optics express*, *27*(26), 37111-37121.

[110] Wang, C., Yu, R., Debord, B., Gérôme, F., Benabid, F., Chiang, K. S., & Xiao, L. (2021). Ultralow-loss fusion splicing between negative curvature hollow-core fibres and conventional SMFs with a reverse-tapering method. *Optics Express*, *29*(14), 22470-22478.

[111] Wang, C., Yu, R., Xiong, C., Zhu, J., & Xiao, L. (2023). Ultralow-loss fusion splicing between antiresonant hollow-core fibres and antireflection-coated single-mode fibres with low return loss. *Optics Letters*, *48*(5), 1120-1123.

[112] Zhang, C., Fokoua, E. N., Fu, S., Ding, M., Poletti, F., Richardson, D. J., & Slavík, R. (2022). Angle-spliced SMF to hollow core fibre connection with optimized back-reflection and insertion loss. *Journal of Lightwave Technology*, *40*(19), 6474-6479.

[113] Poletti, F. E., Wheeler, N. V., Petrovich, M. N., Baddela, N., Numkam Fokoua, E., Hayes, J. R., ... & Richardson, D. J. (2013). Towards high-capacity fibre-optic communications at the speed of light in vacuum. *Nature Photonics*, *7*(4), 279-284.

[114] Zhao, P., Zhao, Y., Bao, H., Ho, H. L., Jin, W., Fan, S., ... & Wang, P. (2020). Mode-phase-difference photothermal spectroscopy for gas detection with an anti-resonant hollow-core optical fibre. *Nature communications*, *11*(1), 847.

[115] Feng, Z., Marra, G., Zhang, X., Fokoua, E. R. N., Sakr, H., Hayes, J. R., ... & Slavík, R. (2022). Stable Optical Frequency Comb Distribution Enabled by Hollow-Core Fibres. *Laser & Photonics Reviews*, *16*(11), 2200167.

[116] Mulvad, H. C. H., Abokhamis Mousavi, S., Zuba, V., Xu, L., Sakr, H., Bradley, T. D., ... & Poletti, F. (2022). Kilowatt-average-power single-mode laser light transmission over kilometre-scale hollow-core fibre. *Nature Photonics*, *16*(6), 448-453.

[117] Numkam Fokoua, E., Michaud-Belleau, V., Genest, J., Slavík, R., & Poletti, F. (2021). Theoretical analysis of backscattering in hollow-core antiresonant fibres. *APL Photonics*, *6*(9).

[118] Slavík, R., Fokoua, E. R. N., Bradley, T. D., Taranta, A. A., Komanec, M., Zvánovec, S., ... & Richardson, D. J. (2022). Optical time domain backscattering of antiresonant hollow core fibres. *Optics Express*, *30*(17), 31310-31321.

[119] Michaud-Belleau, V., Fokoua, E. N., Bradley, T. D., Hayes, J. R., Chen, Y., Poletti, F., ... & Slavík, R. (2021). Backscattering in antiresonant hollow-core fibres: over 40 dB lower than in standard optical fibres. *Optica*, *8*(2), 216-219.

[120] Fokoua, E. N., Petrovich, M. N., Bradley, T., Poletti, F., Richardson, D. J., & Slavík, R. (2017). How to make the propagation time through an optical fibre fully insensitive to temperature variations. *Optica*, *4*(6), 659-668.

[121] Pang, M., & Jin, W. (2009). Detection of acoustic pressure with hollow-core photonic bandgap fibre. *Optics express*, *17*(13), 11088-11097.

[122] Koo, K. P., Dandridge, A., & Tveten, A. B. (1983). Performance characteristics of a passively stabilised fiber interferometer using a (3×3) fiber directional coupler. *In Proc. First international conference on optical fibre sensors*, 200-204.

[123] White, G., K., (1973). "Thermal expansion of reference materials: copper, silica and silicon," *Journal of Physics D: Applied. Physics*. 6 ,2070-2078

[124] Li, X., Lin, S., Liang, J., Zhang, Y., Oigawa, H., and Ueda, T. (2011), "Fiber-optic temeprature sensor based on difference of thermal expansion coefficient between fused silica and metallic materials," *IEEE Photonics,* 4, 155-162.

[125] Land, D. V., Levick, A. P., & Hand, J. W. (2007). The use of the Allan deviation for the measurement of the noise and drift performance of microwave radiometers. Measurement Science and Technology, 18(7), 1917.

[126] https://rio-lasers.com/1550nm-laser-diode/

[127] https://www.liquidinstruments.com/products/hardware-platforms/mokugo/

Appendix

1 Phase extraction method

Based on the definition of thermal sensitivity of compensated interferometers, besides the length and index, the temperature and phase changes are also essential. The temperature is easily read by thermistors; however, the phase change cannot be read directly from the interferometric fringes detected by photodetectors. There are two main methods used to extract the accumulated phase change of interferometer under the temperature perturbation.

i) Phase extracted by counting peaks

The interferometric fringes detected as voltage signals are sinusoidal, and the change of the phase difference between two branches can be calculated by counting the peaks of the fringes, every two peaks equal 2π phase change. It is easy and fast when the phase change is full period and changes in one direction.

$$\mathrm{S} = \frac{1}{L}\frac{d\varphi}{dT} = \frac{Nuber\ of\ Fringes \times 2\pi}{L\Delta T} \tag{1}$$

Counting peaks is an effective method to extract the phase change especially when there are huge amounts of fringes, however, it can have problem with some situations. One is when the phase change is very small even not a full period, which can happen in the compensated fibre interferometer with ultra-small thermal sensitivity, the method cannot work at all, another one is when the sign of phase change reverse, the reversion cannot be found based on this method.

ii) Phase demodulation method based on 3×3 coupler

Due to the shortages of the counting peaks method, the demodulation method based on 3×3 coupler is built to gain higher precision demodulated phase. The main idea of this method is to construct orthogonal variables and demodulate the phase. The optical path scheme and signal process of this method is showed Fig. 1 and Fig.2.

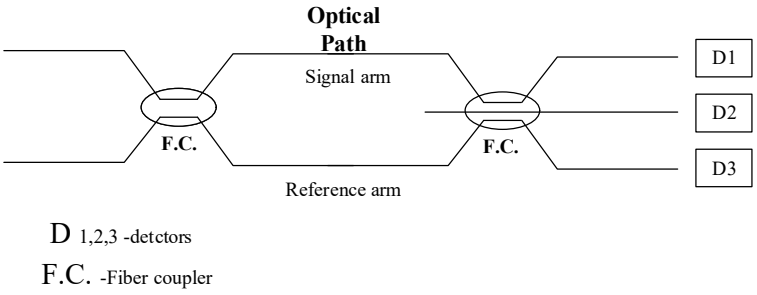

Figure 1. Schematic of the optic circuitry for the (3×3) passive homodyne detection.

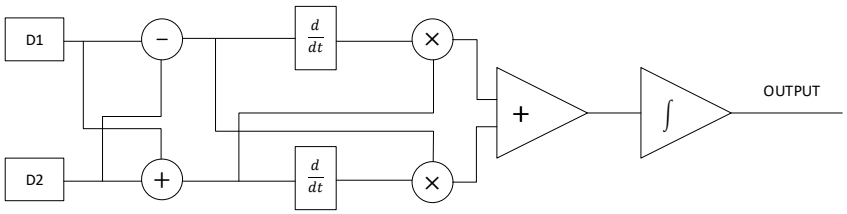

Figure 2. Schematic of the optic and electronic circuitry for the (3×3) passive homodyne detection

3 outputs of 3 photodetectors are:

$$I_1 = A_1 \cos(\theta + \varphi_1) + B_1 \tag{2}$$

$$I_2 = A_2 \cos(\theta + \varphi_2) + B_2 \tag{3}$$

$$I_3 = A_3 \cos(\theta + \varphi_3) + B_3 \tag{4}$$

After normalization, the signals become:

$$I_1 = \cos(\theta + \varphi_1) \tag{5}$$

$$I_2 = \cos(\theta + \varphi_2) \tag{6}$$

$$I_3 = \cos(\theta + \varphi_3) \tag{7}$$

Constructing orthogonal variables by following ways:

$$S_1 = I_1 + I_2 = 2\cos(\theta + (\varphi_1 + \varphi_2)/2)\cos\left(\frac{\Delta\varphi}{2}\right) \tag{8}$$

$$S_2 = I_1 - I_2 = -2\sin(\theta + (\varphi_1 + \varphi_2)/2)\sin\left(\frac{\Delta\varphi}{2}\right) \tag{9}$$

$$\Delta\varphi = \varphi_1 - \varphi_2 \tag{10}$$

$$S_1 \times \dot{S_2} - \dot{S_1} \times S_2 = 4\sin\left(\frac{\Delta\varphi}{2}\right)\cos\left(\frac{\Delta\varphi}{2}\right)\dot{\theta} \ = 2\sin(\Delta\varphi)\,\dot{\theta} \tag{11}$$

The phase is demodulated by integration.

$$\int 2\sin(\Delta\varphi)\,\dot{\theta}\,dt = 2\sin(\Delta\varphi)\,\theta \tag{12}$$

iii) correction of phase difference error of 3×3 coupler

In the phase demodulation method based on 3×3 coupler mentioned above, the $\Delta\varphi$ between the outputs is supposed to be $\frac{2}{3}\pi$(for ideal 3×3 coupler), while it cannot be in fact. To get more precise demodulated phase, correcting this error can be very essential.

After the normalization, the two outputs should be:

$$I_1 = \cos(\theta + \varphi_1) \tag{13}$$

$$\mathrm{I}_2 = \cos(\theta + \varphi_2) \tag{14}$$

The relationship between two outputs can be written as an ellipse equation:

$$x^2 - 2xy\,cos(\Delta\varphi) + y^2 = sin(\Delta\varphi)^2 \tag{15}$$

By fitting the ellipse's equation, get the modulus, so as $\Delta\varphi$.

iv)Polarization error correction

After normalizing the signal, the polarization error can still exist. To get more precise results, it should be eliminated. The normalized outputs should be:

$$I_1 = \mathrm{A(t)}\cos(\theta + \varphi_1) \tag{16}$$

$$I_2 = A(t)\cos(\theta + \varphi_2) \tag{17}$$

Assume $A(t)$ is a slowly change variable (it is a reasonable assumption, for the polarization changes very slowly), get the $\Delta\varphi$ by the method above in a short time period. Then $A(t)$ can be derived:

$$\mathrm{A(t)} = \sqrt{\left(\frac{I_1 + I_2}{2\cos\left(\frac{\Delta\varphi}{2}\right)}\right)^2 + \left(\frac{I_1 - I_2}{2\sin\left(\frac{\Delta\varphi}{2}\right)}\right)^2} \tag{18}$$

Once the $A(t)$ is calculated, it can be eliminated by the division.

2. Length of branch difference

The length difference of two branches of MZI can be measured by coupling the broadband light into the interferometer and recording the interferometric signals, here the function of the interferogram is:

$$f(\lambda) = \cos\left(\frac{2\pi}{\lambda} n\Delta l\right) \tag{19}$$

where λ is the wavelength, n is the index of fibre, Δl is the unbalance of two branches (residual fibre). By calculating the periods of the interferogram, the Δl can be obtained.